Doctoral theses at NTNU, 2013:369

Hanne Kauko

Quantitative scanning transmission electron microscopy studies on heterostructured GaAs nanowires

Doctoral Thesis

Hanne Kauko

ISBN 978-82-471-4890-7 (printed version)
ISBN 978-82-471-4891-4 (electronic version)
ISSN 1503-8181

NTNU – Trondheim
Norwegian University of
Science and Technology

NTNU
Norwegian University of Science and Technology
Thesis for the degree of Philosophiae Doctor
Faculty of Natural Sciences and Technology
Department of Physics

Doctoral theses at NTNU, 2013:369

NTNU

NTNU – Trondheim
Norwegian University of
Science and Technology

Hanne Kauko

Quantitative scanning transmission electron microscopy studies on heterostructured GaAs nanowires

Thesis for the degree of Philosophiae Doctor

Trondheim, December 2013

Norwegian University of Science and Technology
Faculty of Natural Sciences and Technology
Department of Physics

NTNU – Trondheim
Norwegian University of
Science and Technology

NTNU
Norwegian University of Science and Technology

Thesis for the degree of Philosophiae Doctor

Faculty of Natural Sciences and Technology
Department of Physics

ISBN 978-82-471-4890-7 (printed version)
ISBN 978-82-471-4891-4 (electronic version)
ISSN 1503-8181

Doctoral theses at NTNU, 2013:369

Printed by Skipnes Kommunikasjon as

To my mother.

Abstract

This thesis presents a quantitative high-angle annular dark field scanning transmission electron microscopy (HAADF STEM) study on heterostructured GaAs-based nanowires (NWs). Quantitative HAADF STEM was employed to investigate Sb concentration variations in axial GaAsSb inserts within GaAs NWs and in GaAsSb NWs, as well as Al concentration variations in the AlGaAs shell in GaAs/AlGaAs core-shell NWs. The NWs were grown with the vapor-liquid-solid (VLS) growth mechanism using Ga- and Au-assisted molecular beam epitaxy (MBE).

Compositional characterisation by quantitative HAADF STEM was realized by comparing experimental image intensities normalized to the incident beam intensity with simulated intensities. The HAADF STEM image simulations were performed using the frozen-phonon multislice approach. For correct compositional analysis of $GaAs_{1-y}Sb_y$, static atomic displacements (SAD) had to be included in the simulations, however this was not the case with $Al_xGa_{1-x}As$.

GaAsSb inserts within GaAs NWs and GaAsSb NWs were studied with non-corrected STEM at a relatively low magnification using NWs in plane. In this case the known thickness profile of the hexagonal NWs could be exploited in the quantitative HAADF STEM analysis. In the GaAsSb inserts, concentration gradients axially along as well as radially across the insert were identified. The Sb concentration in the insert decreased axially towards the upper and lower interfaces with GaAs, and radially towards the outer surfaces. The axial concentration gradients were attributed to the reservoir effect related to the VLS growth process. The effects of the axial concentration gradients on the NWs optical properties were investigated.

The radial concentration gradients in the GaAsSb inserts result from a combined effect of radial GaAs overgrowth and out-diffusion of Sb during the post-insert axial GaAs growth, causing an increased surface depletion of Sb with increasing post-insert GaAs growth time. In GaAsSb NWs, increased surface depletion of Sb towards the bottom of the NW was observed, and this was attributed to out-diffusion of Sb during the NW growth.

GaAs/AlGaAs core-shell NWs were studied with aberration corrected STEM, using cross-sectional specimens prepared with ultramicrotomy. A method for mapping Al concentration in $Al_xGa_{1-x}As$ at unit cell spatial resolution using the atomic resolution HAADF STEM images was developed. The method is independent of the effective source size and higher order lens aberrations. With the method, Al concentration variations in the AlGaAs shell could be quantified at unit cell spatial resolution.

Acknowledgements

My greatest acknowledgements go to my supervisor Ton van Helvoort. While many PhD students struggle with getting feedback from their supervisors, for me each draft, abstract and application I wrote was met with an abundance of comments. There were certainly times when I found this frustrating, however there was usually a point to each one of the comments, and I highly appreciate your efforts. Moreover, the support I received from you, Ton, during the last months of my PhD, in even all the smallest issues, was invaluable.

A crucial point during my PhD was a three-day visit to the University of Bremen, to learn about quantitative HAADF STEM from the group of Professor Andreas Rosenauer. Had there not been this visit, and the numerous emails sent with Knut Müller and Tim Grieb afterwards, I had not succeeded in this work. I am particularly indebted to Tim, for being my personal online help in HAADF STEM image simulations and quantification.

Moreover, I was privileged to have the opportunity to spend two months at the Monash Centre of Electron Microscopy (MCEM) in Melbourne, Australia, for which I am most grateful to Professor Joanne Etheridge. The level of skill and enthusiasm at MCEM was both impressive and inspiring. I want to thank especially Changlin Zheng, for the late night sessions at the microscope, and Selwyn Glanvill, for making microtomy an enjoyable activity.

This study would not have been possible without the nanowire material to investigate. I must thank the growers, Abdul Mazid Munshi and Dheeraj Dasa Lakshmi Narayana at the Department of Electronics and Telecommunications (IET), NTNU; and particularly Professor Bjørn-Ove Fimland, for sharing his expertise on these nanowires. Further, I want to thank Lyubomir Ahtapadov, for the optical characterisation of the nanowires, and for the help in searching for the truth about the Sb concentration in the nanowire inserts.

Special acknowledgements go to my co-supervisor, Professor Randi Holmestad, for being ever present an eager to help, as well as for creating the special atmosphere we have in the TEM group. I would also like to acknowledge my colleagues in the group: Ruben Bjørge, for all the help and support, especially during the first steps towards quantitative HAADF STEM at NTNU; Jelena Todorovic, for sharing the same room, supervisor, and often also similar worries over three years; Flemming Ehlers, for your kindness and the never-ending conversations; and the rest of the group, for making the working atmosphere pleasant. I am also very grateful to Bjørn Gunnar Soleim, for all the practical help at the microscope.

I must also thank all my good friends here in Trondheim, in Finland and around the world, in the dance cyphers and at the slopes, for making me laugh when I started taking things too seriously. Thank you, William, for the linguistic support, and for being there to calm me down on the days when my head was in a complete chaos.

Dad, Jessi and Ville – thank you for being always there, a phone call away. My home is still there where you are, dad; thank you for that. Lastly, I wish I could thank my mother. If there is any persistence in me that took me here, it is all because of her.

Preface

This thesis is submitted as a partial fulfilment of the requirements for the degree of philosophiae doctor (PhD) at the Norwegian University of Science and Technology (NTNU). The doctoral work was carried out at the Department of Physics (IFY), NTNU, where also majority of the experimental results were obtained, from September 2009 to October 2013. This period included a year of teaching duties. Three research visits abroad were conducted: a short visit to the University of Bremen, Germany, in learning purposes; a short visit to the Aalto University, Finland, for experiments; and a two-month visit to the Monash Centre of Electron Microscopy (MCEM), Australia, where both experimental work and simulations were carried out.

The thesis is divided into three parts. Part I is a general introduction to the methods applied as well as the material investigated. The main scientific results are given in Part II, comprised of the scientific papers as listed below. The work is concluded in Part III, where the main findings from both method and materials perspective are summarized, and suggestions for future work are given.

Publications included in this thesis

- **Paper I**
  "Compositional characterization of GaAs/GaAsSb nanowires by quantitative HAADF-STEM." H. Kauko, T. Grieb, R. Bjørge, M. Schowalter, A. M. Munshi, H. Weman, A. Rosenauer and A. T. J. van Helvoort. *Micron* **44**, 254–260 (2013).

- **Paper II**
  "The effects of Sb concentration variation on the optical properties of GaAsSb/GaAs heterostructured nanowires." J. Todorovic, H. Kauko, L. Ahtapodov, A. F. Moses, P. Olk, D. L. Dheeraj, B. O. Fimland, H. Weman and A. T. J. van Helvoort. *Semiconductor Science and Technology* **28**, 115004 (2013).

- **Paper III**
  "Antimony surface depletion during the growth of GaAsSb and GaAs/GaAsSb nanowires." H. Kauko, B. O. Fimland, T. Grieb, A. M. Munshi, A. Rosenauer and A. T. J. van Helvoort. In preparation.

- **Paper IV**
  "Compositional analysis of GaAs/AlGaAs heterostructures using quantitative scanning transmission electron microscopy." H. Kauko, C. L. Zheng, Y. Zhu, S. Glanvill, C. Dwyer, A. M. Munshi, B. O. Fimland, A. T. J. van Helvoort and J. Etheridge. Accepted for publication in *Applied Physics Letters*.

Author's contribution Scientific research is a team effort, and all the listed co-authors have contributed either experimentally or in interpreting the results and writing the manuscript. I have had the responsibility for the HAADF STEM experiments, and the related conventional TEM (CTEM) and energy dispersive X-ray spectroscopy (EDX) characterisation at NTNU. I have further had the responsibility for the quantitative interpretation of the HAADF STEM image intensities in all the four papers. In Paper II, J. Todorovic performed most of the CTEM and EDX experiments as well as the correlated photoluminescence (PL)-TEM characterisation, and wrote the manuscript. In Paper IV, the high-resolution HAADF STEM images were acquired by C. L. Zheng at MCEM. The HAADF STEM image simulations for GaAsSb for Papers I-III were performed by T. Grieb (University of Bremen, Germany), and for AlGaAs for Paper IV by the author. The NW material investigated was grown by A. M. Munshi (Papers I, III and IV) and D. L. Dheeraj (Paper II) at the Department of Electronics and Telecommunications (IET) at NTNU.

Publications not included in this thesis

- "Quantitative HAADF-STEM on heterostructured GaAs nanowires." H. Kauko, R. Bjørge, R. Holmestad and A. T. J. van Helvoort. *Journal of Physics: Conference Series* **371**, 012056 (2012).

Conference contributions (Presenter underlined)

- "Quantitative HAADF-STEM on heterostructured GaAs nanowires." H. Kauko, R. Bjørge, R. Holmestad and A.T.J. van Helvoort. Scandem 2011, Oulu, Finland, 8-10 June 2011. [Poster and oral presentation]
- "Quantitative HAADF-STEM on heterostructured GaAs nanowires." H. Kauko, R. Bjørge, R. Holmestad and A.T.J. van Helvoort. EMAG 2011, Birmingham, UK, 6-9 September 2011. [Oral presentation]
- "Composition analysis of heterostructured GaAs nanowires with quantitative HAADF-STEM." H. Kauko, T. Grieb, A. Rosenauer, R. Bjørge, M. Munshi, H. Weman and A. T. J. van Helvoort. Nanolab user meeting, Trondheim, 16 November 2011. [Oral presentation]
- "Studying Sb distribution in heterostructured GaAs/GaAsSb nanowires with quantitative HAADF-STEM." H. Kauko, T. Grieb, A. Rosenauer and A. T. J. van Helvoort. European Microscopy Congress (EMC 2012), Manchester, UK, 16-21 September 2012. [Poster]
- "GaAs/AlGaAs core-shell nanowires for novel solar cell applications." H. Kauko, A. M. Munshi, C. G. Lim, D. C. Kim, D. L. Dheeraj, B. O. Fimland, A. T. J. van Helvoort and H. Weman. Norwegian Solar Cell Conference 2013, Oppdal, Norway, 13-15 March 2013. [Poster]
- "GaAs/AlGaAs core-shell nanowires for novel solar cell applications." H. Kauko, A. M. Munshi, C. G. Lim, D. C. Kim, D. L. Dheeraj, B. O. Fimland, A. T. J. van Helvoort and H. Weman. Nanokonferansen 2013, Oslo, Norway, 18 March 2013. [Poster and oral presentation]
- "Novel solar cells based on GaAs/AlGaAs core-shell nanowires." H. Kauko, A. M. Munshi, C. G. Lim, D. C. Kim, D. L. Dheeraj, B. O. Fimland, A. T. J. van Helvoort and H. Weman. Annual Nano Network Workshop 2013, Bergen, Norway 17-19 June 2013. [Poster]

Trondheim, December 2013

Hanne Kauko

Acronyms

ADF	annular dark field
BF	bright field
BFP	back focal plane
CBED	convergent beam electron diffraction
CCD	charge-coupled device
CT	concentration-thickness
CTEM	conventional transmission electron microscopy
CTF	contrast transfer function
DF	dark field
DV	differential voltage
EDX	energy dispersive X-ray spectroscopy
EELS	electron energy loss spectroscopy
FEG	field emission gun
FFP	front focal plane
FFT	fast Fourier transform
GPU	graphical processing unit
HAADF	high-angle annular dark field
HR	high-resolution
IFT	inverse Fourier transform

LED	light-emitting diode
MBE	molecular beam epitaxy
MTF	microscopy transfer function
NW	nanowire
OTF	optical transfer function
PL	photoluminescence
PSF	point spread function
SAD	static atomic displacements
SAED	selected area electron diffraction
SEM	scanning electron microscopy
STEM	scanning transmission electron microscopy
TDS	thermal diffuse scattering
TEM	transmission electron microscopy
VLS	vapor-liquid-solid
VS	vapor-solid
WZ	wurtzite
Z	atomic number
ZB	zinc blende

Contents

Part I

Introduction

Chapter 1

Motivation

Semiconductor materials are the foundation for most modern day electronics, such as transistors, lasers, light-emitting diodes (LED), charge-coupled devices (CCD), and solar cells. What is particular about semiconductors is that their electrical and optical properties are strongly dependent on the material composition. This implies that these properties can be tailored for specific applications by adjusting the composition. The conductivity of a semiconductor is dependent on small amounts of specific impurities, dopants, in the material. In the case of III-V semiconductors such as GaAs, the band gap energy can be tuned by alloying. For instance for solar cells this means that the material's response to the solar spectrum can be optimized, and for other optoelectronic applications, such as LEDs and lasers, this means that their emission spectrum can be adjusted by changing the material composition. To be able to produce the desired semiconductor devices, it is crucial to be able to characterise the material composition at a high spatial resolution. This is particularly important for nanostructured semiconductor devices.

High-angle annular dark field scanning transmission electron microscopy (HAADF STEM) is a method for imaging materials at a high spatial resolution, with the image intensity sensitive to the atomic number, Z, and specimen thickness [1, 2]. With an appropriate characterisation of the incident electron beam and the detector, the experimental image intensities can be compared, at an absolute scale, with simulated intensities [3, 4]. Consequently, the chemical composition [5, 6, 7] and thickness [8, 9] of the specimen can be mapped at a high spatial resolution on the basis of the image intensities. The method where specimen composition or thickness is determined by comparing simulated and experimental HAADF STEM image intensities is referred to as quantitative HAADF STEM. In the present

work, this method has been applied for characterising the composition in heterostructured GaAs-based nanowires.

Nanowires (NWs) are thin (in the order of $10-100$ nm), usually $3-5$ μm long wires that can be grown epitaxially from a substrate in controlled chemical processes. The special geometry provides many unique properties. Firstly, strain-free growth of lattice-mismatched heterostructures into the NWs, and on lattice-mismatched substrates is enabled due to strain-relaxation at the free surface [10]. This has been a long-term problem for conventional, planar semiconductor heterostructures. It gives the possibility to fine-tune the NWs optoelectronic properties and enables the integration of high-performance III-V semiconductors with for instance silicon [11]. The geometry provides also design freedom: in addition to axial heterostructures along the NW [12, 13], radial heterostructures can be grown [14, 15]. Growth of radial heterostructures allows the formation of a radial p-n junction, which could be a particularly advantageous design for instance for solar cells [16, 17, 18], transistors [19, 20] and LEDs [21, 22]. Furthermore, a two-dimensional NW array with optimal density provides light trapping; yet another benefit for NW-based solar cells [23, 24]. Finally, owing to the high surface-to-volume ratio, the demand for active material is greatly reduced when NWs are used instead of planar structures.

To be able to grow heterostructured NWs with the desired properties, it is important to be able to characterise the composition at a high spatial resolution. Here, quantitative HAADF STEM has been applied for studying two types of heterostructured GaAs-based NWs: GaAs NWs with axial GaAsSb inserts, and GaAs/AlGaAs core-shell NWs. In addition, GaAsSb NWs were studied. The GaAs NWs with GaAsSb inserts and GaAsSb NWs were studied in plane, i.e., as lying on a facet, and the GaAs/AlGaAs core-shell NWs were studied in cross-section. From quantitative HAADF STEM perspective this means that two very different GaAs alloys, as well as two different zone axes and specimen geometries were studied. Moreover, the quantitative studies were carried out on two different microscopes and resolution ranges: at a relatively low resolution on a JEOL 2010F at NTNU, and at a high resolution on an aberration corrected FEI Titan^3 80-300 at MCEM. In this introduction part the aim is to introduce the reader the basics of the quantitative HAADF STEM method applied and the NW material investigated, as well as to pass on the knowledge that was acquired from studying two such different systems by quantitative HAADF STEM.

Chapter 2

Scanning Transmission Electron Microscopy

The resolving power, i.e., the smallest distinguishable distance, of a type of radiation is determined by its wavelength. The wavelength of visible light is on average 550 nm, and the resolution of an optical microscope is hence limited to that scale. The idea of a transmission electron microscope (TEM) was first suggested by Knoll and Ruska in 1932 [25] – with the modest goal to exceed the resolution of an optical microscope [26]. Earlier, in 1925 de Broglie had formulated the theory for the wave nature of particles, relating the momentum of a particle to its wavelength according to $\lambda = h/p$ [27]. According to this formula, an electron accelerated with 200 kV, corresponding to a typical acceleration voltage in a modern TEM, has a wavelength of 0.025 Å. Due to lens aberrations the practical resolution of a common TEM is however limited to "only" $1 - 2$ Å, which is in the order of the spacing between atoms in a crystal. With modern, aberration corrected instruments, sub-ångstrom resolution is obtained.

Not surprisingly, visualizing single atoms has been one of the central goals in the development of TEM. The first successful attempts were realized by Crewe and his collaborators in 1970 – with a scanning TEM (STEM) [28]. In their famous experiment they used a STEM instrument specifically developed in their laboratory, equipped with a field emission gun (FEG), and collecting the transmitted electrons with an annular detector [29]. The specimen had uranium atoms deposited on a carbon film. An essential improvement in the instrumentation was the use of a FEG instead of a thermionic electron source, providing sufficient signal strength and coherency to enable the atomic resolution STEM.

Since the first goal was reached, the aim has been to obtain quantita-

tive images of atomic lattices with higher and higher resolution. So far the method best suited for this task has proven to be high-angle annular dark field (HAADF) STEM. What makes HAADF STEM so attractive is that the produced images are incoherent, with intensity localized on atomic column positions and dependent on the atomic number (Z) and thickness [30]. This allows the intensity at a certain point in the image to be directly related to the average Z and thickness of the atomic column in the corresponding point in the lattice.

This chapter starts with a brief introduction to the basic operating principles of a TEM and a STEM, followed by a section discussing the limits of the STEM resolution, and how these limits can be overcome by aberration correction. The majority of the chapter is devoted to HAADF STEM, which was the main method used in the present work. In section 2.3 the factors that render HAADF STEM images incoherent, and give the intensity the dependency on Z, are addressed. HAADF STEM image simulations are introduced in section 2.4. The further steps that need to be taken for compositional analysis by quantitative HAADF STEM – that is, to be able to compare experimental and simulated intensities – are covered in section 2.5. The chapter concludes with a discussion on the status of quantitative HAADF STEM as a tool for high-resolution compositional analysis.

2.1 Basic operating principles

2.1.1 Transmission Electron Microscopy

The basic set-up of a TEM is illustrated in figure 2.1(a). Electrons originating from either a thermionic or a field-emission source are accelerated by the electron gun, and the electron beam is controlled by electromagnetic lenses and deflector coils [31]. Starting from the top of the microscope, the function of the condenser lenses is, as the name indicates, to condense and spread the beam to control the illumination on the specimen. The condenser lens aperture limits the angular range of the electrons that are allowed to proceed to the specimen, hence making the beam more parallel and removing the high-angle electrons that suffer most from the lens aberrations (see section 2.2).

In most TEMs, the specimen sits in between the upper and lower polepiece of the objective lens. The upper polepiece is exploited in forming the highly focused electron probe required in the STEM mode. The lower polepiece is responsible for image formation in conventional TEM (CTEM). It is hence primarily the aberrations of this lens that determine the image quality

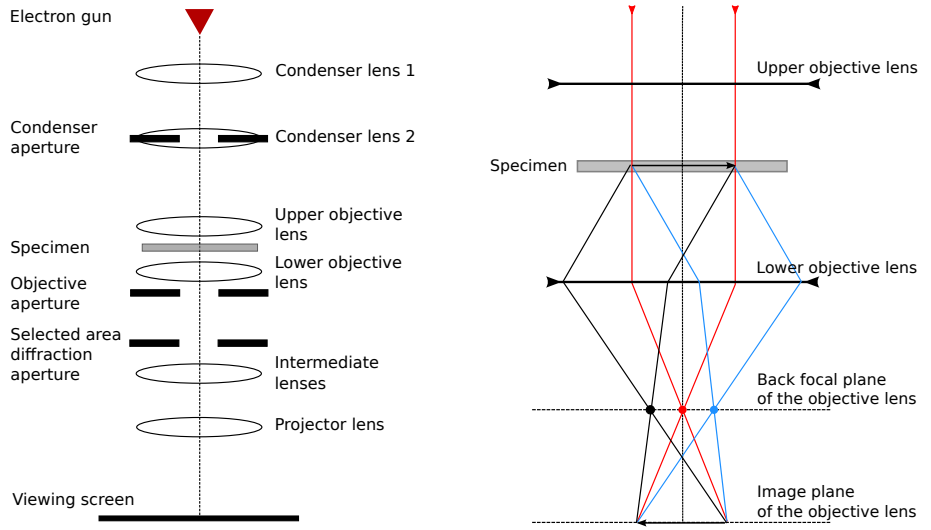

(a) (b)

Figure 2.1: (a) A schematic of the TEM set-up and (b) the electron ray paths after the specimen.

in TEM. In TEM mode, the image is further magnified by the intermediate and projector lenses, before it is finally projected on to the screen or the CCD camera. The intermediate and projector lenses are also employed in switching between imaging and diffraction mode in TEM – that is, projecting either the back focal plane (BFP) or the image plane of the objective lens on to the screen, which is explained in more detail below.

Figure 2.1(b) shows a more detailed view of the electron trajectories through the specimen and the lower objective lens. When crystalline specimens are studied in highly symmetric zone axis orientations, the electrons will scatter from parallel crystal planes to certain distinct angles. Electrons diffracting from a certain set of planes will scatter to a certain angle, and these electrons are brought to the same point in the BFP of the objective lens, as is illustrated with the black, red and blue ray paths in figure 2.1(b). This is the plane that is projected on to the screen when operating the microscope in diffraction mode. On the other hand, the electrons originating from a certain point in the sample are brought to the same point in the image plane of the objective lens. This is the plane that is projected on to the screen in imaging mode.

In the imaging mode, different imaging techniques can be performed by inserting an objective aperture in the BFP (see figure 2.1(a)). In bright field (BF) imaging, the aperture is centered around the central, non-diffracted beam. In this case, areas in the specimen diffracting strongly will appear dark – this is called diffraction contrast. Alternatively, the objective aperture can be centered around one or some of the diffracted beams to perform dark field (DF) imaging. In this technique regions of the specimen diffracting in that particular direction will appear bright. In high-resolution (HR) TEM imaging a large aperture or no aperture at all is inserted, allowing the diffracted and non-diffracted beams to interfere, and the image is highly magnified with the intermediate and projector lenses to obtain lattice resolution.

In diffraction mode, an aperture is inserted in the image plane to restrict the area of the specimen contributing to the diffraction pattern. This is called selected area electron diffraction (SAED). If a parallel beam is used, sharp diffraction spots are formed. If a convergent beam is used instead, in a method called convergent beam electron diffraction (CBED), diffraction disks with a size dependent on the convergence angle are formed. The intensity variations in these disks tell a detailed story about the electron scattering within the specimen, and quantitative CBED can be used for determining for instance the specimen thickness [32] and structure factors of the material [33].

2.1.2 Scanning Transmission Electron Microscopy

In STEM the image is formed by scanning a probe (convergent beam) in a raster over the specimen and collecting the transmitted electrons at each probe position (figure 2.2). The image magnification is determined by the size of the scanned area rather than magnification by lenses. The intensity of a certain pixel in the image is the total signal collected with a certain detector during the dwell time, i.e., the duration the probe was placed on a given position. This kind of serial imaging allows site-specific collection of different types of signals simultaneously, however the process becomes very sensitive to mechanical and electrical disturbances due to the long scanning times required (typically 10-40 s). On the contrary in CTEM the whole image is generated in one go (usually in less than a second) by direct illumination of the specimen with a fixed parallel beam.

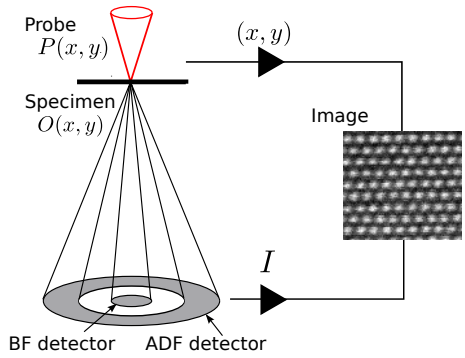

Figure 2.2: Operating principle of the STEM imaging system.

Instrument design

The focused probe is formed by the condenser lenses together with the upper pole piece of the objective lens [31]. When scanning the probe over the specimen, it is essential that at each point the probe is parallel to the optical axis. This is obtained with double deflection coils residing above the upper pole piece of the objective lens that pivot the beam about the front focal plane (FFP) of the objective lens (see figure 2.3(a)). With this kind of system, assuming a single-crystalline specimen, a stationary CBED pattern is created in the BFP of the lower objective lens as is illustrated in figure 2.3(b). The STEM detectors sit in the diffraction plane, and to form a real-space image, a certain part of the CBED pattern is collected by a certain detector, as will be explained in the following section. The STEM detector is either a semiconductor device or a scintillator-photomultiplier, both very sensitive to the number of electrons falling on the detector.

In a TEM/STEM, which is the most common instrument design, the STEM detectors cannot obviously be placed in the BFP of the objective lens because this space is filled by the objective aperture. The STEM detectors are then inserted in the viewing chamber (or below it), and the TEM is operated in diffraction mode when doing STEM.

Detector geometries and imaging modes in STEM

BF imaging in STEM is performed by using a circular detector centered on the optical axis. The size of the BF detector is such that it picks the central disk of the CBED pattern [31]. If the size of the probe-forming (condenser) aperture is big enough to allow the disks to overlap (see section 2.3.1),

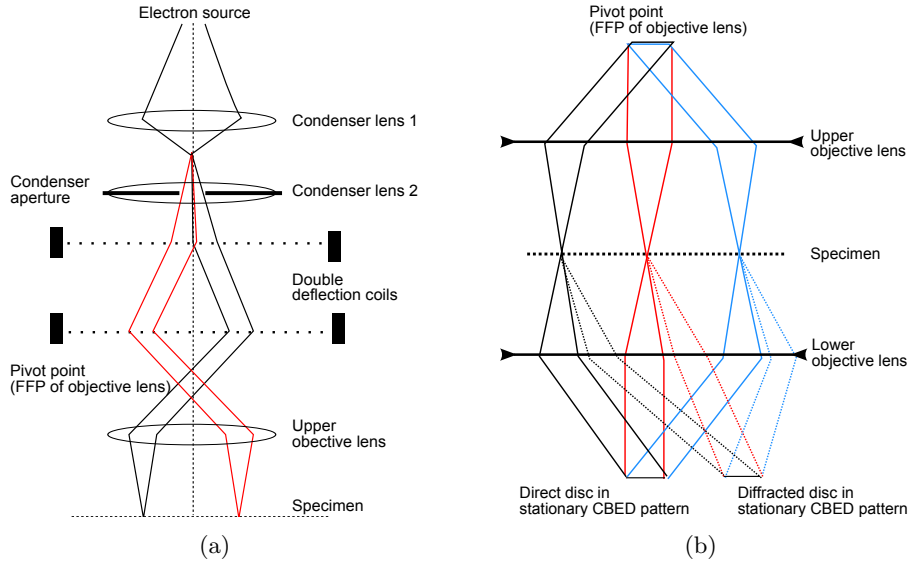

Figure 2.3: (a) Schematic of the STEM lens system and the scanning of a convergent probe and (b) a more detailed ray diagram for the specimen stage. (Redrawn after [31].)

the BF STEM detector will pick scattering from both the direct and the overlapping first-order diffracting disks, allowing lattice imaging [34]. Under these conditions BF STEM contrast is equivalent to HRTEM image contrast according to the principle of reciprocity [35]. BF STEM images are hence coherent phase-contrast images. Recently a BF imaging technique with a small annular detector placed within the bright field cone, called annular BF (ABF) imaging, has received interest as a means of visualizing light elements [36].

Annular dark field (ADF) images are formed by inserting an annular detector, centered around the optical axis. In this way all the beams scattered to a certain angular range are collected. The BF detector sits in the centre of the annular detector; thus BF and ADF images can be recorded simultaneously. High-angle ADF (HAADF) imaging means selecting an annular detector with a large inner and outer radius (typically from $\sim 30-50$ mrad to $\gtrsim 150$ mrad, depending on the acceleration voltage) in order to detect electrons scattered to high angles. In HAADF imaging, diffraction-contrast effects are minimized through the averaging over the large detector area, and incoherent images with intensity dependent on Z are obtained, as will be shown in section 2.3.

2.2 Breaking the limits to resolution

The resolution of STEM is defined by the size of the probe, which is primarily limited by the diffraction limit and spherical aberration [37]. Diffraction limit arises from the probe-forming aperture. If a circular aperture is illuminated with an approximately parallel beam, an Airy pattern – a central maximum with concentric side lobes – is formed in the object plane [37]. The size of the probe can be defined as the diameter of the first minimum, δ_D, in the Airy pattern

$$\delta_D = 0.61\frac{\lambda}{\alpha}, \tag{2.2.1}$$

where α is the convergence semi-angle. Hence, the larger the convergence angle (i.e., the larger the probe-forming aperture), the smaller the probe and hence the better the resolution. This is illustrated in figure 2.4, where two probes with different convergence angles are plotted.

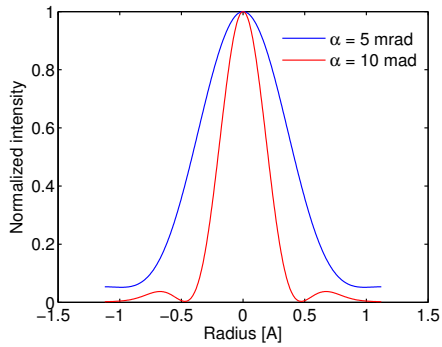

Figure 2.4: Intensity line profile for a STEM probe for 200 keV electrons, with a defocus of 50 nm and a spherical aberration constant C_3 of 1 mm, for two different convergence semi-angles α: 5 mrad and 10 mrad. The probe intensity profiles were calculated using a MATLAB code from Kirkland [38].

Nevertheless, an aperture has to be inserted – with the cost of loss in resolution and intensity – in order to remove the high-angle electrons that suffer most from aberrations. Very soon after the construction of the first electron microscope in 1932, it was proved by Scherzer in 1936 that the electron lenses would always suffer from chromatic and spherical aberrations [39]. Chromatic aberration results in electrons with a wide range of energies being focused in different planes by the lens, however this is not a limiting factor for the resolution in STEM [40]. Spherical aberration in turn is a defect occurring because the magnetic field of the lens behaves

differently for off-axis electrons: electrons travelling further away from the optical axis are brought to focus earlier than electrons travelling closer to the optical axis, as is illustrated in figure 2.5. As a result, the point where the envelope of all the rays is smallest is not a point but a disk, referred to as the disk of least confusion, with the radius δ_S given by [37]

$$\delta_S = \frac{1}{4} C_3 \alpha^3, \tag{2.2.2}$$

where C_3 is the spherical aberration coefficient. This expresses how the probe size is limited by the spherical aberration. It is however obvious that δ_S is smallest with vanishing α – opposite to the diffraction limit. Hence to be able to use a large convergence angle to obtain the smallest possible probe, correcting for spherical aberration is crucial.

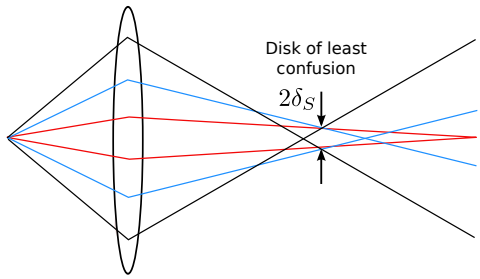

Figure 2.5: The paths of different rays through a lens with spherical aberration. Rays travelling far from optical axis come to cross-over earlier than those travelling close to optical axis.

Spherical aberration correctors are complex devices that compensate for the spherical aberration in the magnetic lenses with additional magnetic lenses [39]. After the discovery of spherical aberration, it took 60 years of struggling before the first aberration corrected commercial STEM was eventually put into practice in 1997 by Krivanek and co-workers [41]. The first aberration corrected TEM was established a year later [42], with a slightly different technology. The first sub-ångstrom resolution STEM images became finally published in 2002 [43]. Since then aberration corrected electron microscopy has been a success story, allowing routine acquisition of atomic resolution STEM images, even at lower voltages [44].

Despite the success several challenges remain. Aberration correction allows the use of a larger probe-forming aperture, thus electrons from a wider range of angles are incident on an atomic column. With higher transverse kinetic energy, the probe can more easily spread to adjacent atomic columns,

making images less easily interpretable [45, 46]. Furthermore, a larger convergence angle implies also a higher probe intensity, leading to an increased probability for beam damage. Finally, the aberration corrected instruments are very expensive to purchase and to maintain, and extensive training programmes are required to meet the required level of skill for operating the microscopes [47].

2.3 HAADF STEM image formation

The strengths of HAADF STEM imaging lie in the incoherency and the Z-sensitivity of the image intensity, as was mentioned at the start of this chapter. All our common light sources are incoherent – hence our eyes are used to interpreting incoherent images rather than interference fringes. The Z-sensitivity allows compositional analysis at a high resolution from the basis of the image intensities. This section addresses the obvious questions arising now: what are actually the conditions for incoherent imaging, what is it that renders HAADF STEM signal incoherent, and where does the compositional sensitivity arise from?

The concept of incoherent imaging applies strictly only for self-luminous objects [48]. However, Lord Rayleigh suggested already in 1896 that illuminating a specimen over a wide range of angles would render the specimen effectively self-luminous, and thus no interference between radiation emitted from spatially separated parts in the specimen could occur [30]. The imaging process can then be described as incoherent, and the image intensity becomes a convolution in intensity [30]:

$$I_{incoh} = |P(\boldsymbol{R})|^2 \otimes |\psi(\boldsymbol{R})|^2, \tag{2.3.1}$$

where $P(\boldsymbol{R})$ is now the function of the illuminating probe and $\psi(\boldsymbol{R})$ is the object wave-function. This is the mathematical definition for incoherent imaging.

On the contrary, in HRTEM imaging the specimen is illuminated with a coherent plane wave. The image is formed from the exit-surface wavefunction $\psi(\boldsymbol{R})$ by the objective lens, which suffers from aberrations. The blurring effect of the lens aberrations can be described as a convolution of the exit-surface wavefunction with a point spread function (PSF) $P(\boldsymbol{R})$, so that the resulting image intensity becomes [30]

$$I_{coh} = |P(\boldsymbol{R}) \otimes \psi(\boldsymbol{R})|^2, \tag{2.3.2}$$

which is the mathematical definition for coherent imaging. Writing out the

square gives

$$I_{coh} = [P(\boldsymbol{R}) \otimes \psi(\boldsymbol{R})] \cdot [P^*(\boldsymbol{R}) \otimes \psi^*(\boldsymbol{R})], \tag{2.3.3}$$

which shows explicitly that the convolution of $\psi(\boldsymbol{R})$ with the PSF is in complex amplitude and phase information is lost in the imaging process. The phase of the PSF can change rapidly when changing e.g. defocus, and the phase of $\psi(\boldsymbol{R})$ is sensitive to thickness. Thereby the resulting coherent image intensity is sensitive to these parameters, and contrast reversals are observed with changing defocus and specimen thickness. This does not occur with incoherent imaging, as will be shown in section 2.3.1.

In this section first the components of STEM image formation are introduced, following the approach by Nellist and Pennycook [30]. At this stage scattering from the specimen is treated with a kinematic scattering approximation, i.e., assuming that the specimen is very thin and the electrons are scattered only once. A mathematical proof for the incoherency of HAADF STEM imaging is already obtained with this approach. For a more physical picture, and to understand why HAADF STEM intensity is sensitive to Z and localized to atomic column positions, dynamical scattering – i.e., multiple scattering events in the specimen – has to be considered. This will be done in section 2.3.2, using a Bloch-wave approach. Now, these two approaches still consider only the portion of coherent scattering falling on the ADF detector. In fact, most of the scattering upon the ADF detector is incoherent thermal diffuse scattering (TDS) – this will be shown in section 2.3.3.

2.3.1 Components of STEM image formation

The probe function

The STEM image is formed by scanning the specimen with a focused probe and collecting a certain portion of the transmitted electrons for each probe position, as was explained in section 2.1.2. The focused probe can be described as a coherent superposition of partial plane waves, each labelled by its transverse component $\boldsymbol{K_i}$ (see figure 2.6). The probe is focused by the probe-forming lens, and due to lens aberrations each partial plane wave experiences a phase shift $\chi(\boldsymbol{K_i})$ relative to the $\boldsymbol{K_i} = 0$ -wave [30]:

$$\chi(\boldsymbol{K_i}) = \pi\lambda C_1 |\boldsymbol{K_i}|^2 + \frac{1}{2}\pi\lambda^3 C_3 |\boldsymbol{K_i}|^4, \tag{2.3.4}$$

where λ is the electron wavelength and C_1 is the defocus. For aberration corrected instruments, the resolution is not limited by C_3, and higher-order aberration terms have to be included in $\chi(\boldsymbol{K_i})$ [49].

To limit the influence of aberrations, only a certain portion of the initial electron beam is selected with the probe-forming aperture, described by a circular top-hat function $H(\boldsymbol{K_i})$ in reciprocal space, which is equal to unity within the aperture and zero outside. $H(\boldsymbol{K_i})$ and $\chi(\boldsymbol{K_i})$ can be combined as magnitude and phase, respectively, to form the complex aperture function $A(\boldsymbol{K_i})$:

$$A(\boldsymbol{K_i}) = H(\boldsymbol{K_i})e^{i\chi(\boldsymbol{K_i})}, \tag{2.3.5}$$

which describes the overall wave at the FFP. The illuminating probe function is obtained from this expression with inverse Fourier transform, which acts as a summation over all the incident partial plane waves [30]:

$$P(\boldsymbol{R}) = \int A(\boldsymbol{K_i})e^{i2\pi \boldsymbol{K_i}\cdot\boldsymbol{R}}d\boldsymbol{K_i}, \tag{2.3.6}$$

The effect of the scanning, i.e., varying the point on the specimen, $\boldsymbol{R_0}$, can be incorporated by multiplying $A(\boldsymbol{K_i})$ with a phase factor $e^{-i2\pi(\boldsymbol{K_i}\cdot\boldsymbol{R_0})}$. This yields

$$P(\boldsymbol{R}-\boldsymbol{R_0}) = \int A(\boldsymbol{K_i})e^{i2\pi \boldsymbol{K_i}\cdot(\boldsymbol{R}-\boldsymbol{R_0})}d\boldsymbol{K_i}. \tag{2.3.7}$$

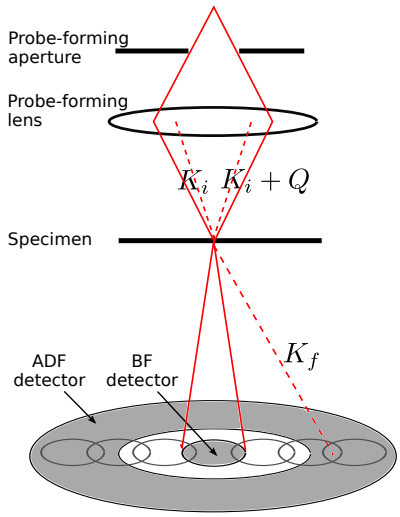

Figure 2.6: A schematic of the scattering of the STEM probe, focused by the probe-forming lens on to the specimen. Different parts of the resulting CBED pattern are detected by the BF and ADF detectors. The dashed lines describe the two incident partial plane waves ($\boldsymbol{K_i}$ and $\boldsymbol{K_i + Q}$) that are scattered into the same final wave vector $\boldsymbol{K_f}$. (Redrawn after [2].)

Scattering from the sample

In the kinematic approximation, scattering from the sample can be described as a single scattering event that scatters the initial wave vector, $\boldsymbol{K_i}$, into a final wave vector $\boldsymbol{K_f}$. The scattering event changes the magnitude and the phase of the incident wave by a complex multiplier $\Psi(\boldsymbol{K_f}, \boldsymbol{K_i})$. The intensity in far-field then becomes (setting $\boldsymbol{R}$ to origin) [30]

$$\begin{aligned} I(\boldsymbol{K_f}, \boldsymbol{R_0}) &= \left| \int A(\boldsymbol{K_i}) e^{-i2\pi \boldsymbol{K_i} \cdot \boldsymbol{R_0}} \Psi(\boldsymbol{K_f}, \boldsymbol{K_i}) d\boldsymbol{K_i} \right|^2 \\ &= \int \int A(\boldsymbol{K_i}) A^*(\boldsymbol{K_i'}) e^{-i2\pi(\boldsymbol{K_i} - \boldsymbol{K_i'}) \cdot \boldsymbol{R_0}} \\ &\cdot \Psi(\boldsymbol{K_f}, \boldsymbol{K_i}) \Psi^*(\boldsymbol{K_f}, \boldsymbol{K_i'}) d\boldsymbol{K_i} d\boldsymbol{K_i'}. \end{aligned} \tag{2.3.8}$$

Writing $\boldsymbol{K_i'} = \boldsymbol{K_i} + \boldsymbol{Q}$ and taking the Fourier transform of the intensity, the exponential terms are cancelled out and the expression is reduced into a single integral:

$$\begin{aligned} \widetilde{I}(\boldsymbol{K_f}, \boldsymbol{Q}) &= \int I(\boldsymbol{K_f}, \boldsymbol{R_0}) e^{-i2\pi \boldsymbol{Q} \cdot \boldsymbol{R_0}} d\boldsymbol{R_0} \\ &= \int A(\boldsymbol{K_i}) A^*(\boldsymbol{K_i} + \boldsymbol{Q}) \Psi(\boldsymbol{K_f}, \boldsymbol{K_i}) \Psi^*(\boldsymbol{K_f}, \boldsymbol{K_i} + \boldsymbol{Q}) d\boldsymbol{K_i} \end{aligned} \tag{2.3.9}$$

where $\widetilde{I}$ denotes the Fourier transformation of the intensity, recorded by a point detector at $\boldsymbol{K_f}$ in far field.

Expression (2.3.9) now describes the scattering event illustrated in figure 2.6: two initial partial plane waves, separated by $\boldsymbol{Q}$, are scattered by the specimen into the same final wave vector $\boldsymbol{K_f}$, where they interfere [30]. If the scattering is coherent Bragg diffraction, a CBED pattern will be formed in the detector plane. The initial partial plane wave pairs are scattered into a single wave vector in the disk overlap regions, where interference can occur. It can be read from equation (2.3.9) that when varying the probe position R_0, the intensity in the overlap regions varies sinusoidally with a spatial frequency of $\boldsymbol{K_i} - \boldsymbol{K_i'} = \boldsymbol{Q}$ – this is STEM lattice imaging [34]. The intensity in the CBED disks does however not vary when varying the probe position. If the disks do not overlap, there is no image contrast, and hence no lattice in the image.

The degree of overlap is determined by the size of the CBED disks, which is determined by the convergence angle of the probe. Hence the convergence angle needs to be large enough to allow overlap in order to obtain lattice resolution. Large overlapping disks in reciprocal space means a small

probe in real space – hence the larger the convergence angle, the better the resolution, as was already concluded in section 2.2.

Image intensity falling on a detector

According to Lord Rayleigh, illuminating an object with a large source over a wide range of angles in TEM would destroy interference between radiation emitted from spatially separate parts in the object and thus render the image incoherent, as was mentioned at the start of this section. The principle of reciprocity states that a large source in TEM corresponds to a large detector in STEM [35]. For the image intensity to be incoherent, the expression for intensity should be of the form of equation (2.3.1): a convolution in intensity between a probe-function and an object-function in real space (a multiplication in reciprocal space). This condition can actually be fulfilled by the detector geometry alone.

The image intensity on an ADF detector is obtained by integrating over expression (2.3.9) with a detector function $D(\boldsymbol{K_f})$ [30]:

$$\begin{aligned}\widetilde{I}(\boldsymbol{Q}) = \int D(\boldsymbol{K_f}) \int A(\boldsymbol{K_i} - \boldsymbol{Q/2})A^*(\boldsymbol{K_i} + \boldsymbol{Q/2}) \\ \cdot \Psi(\boldsymbol{K_f} - \boldsymbol{K_i} + \boldsymbol{Q/2})\Psi^*(\boldsymbol{K_f} - \boldsymbol{K_i} - \boldsymbol{Q/2})d\boldsymbol{K_i}d\boldsymbol{K_f},\end{aligned} \tag{2.3.10}$$

where $\boldsymbol{K_i}$ has been shifted to $\boldsymbol{K_i} - \boldsymbol{Q/2}$. Now, the domain of integral for $\boldsymbol{K_i}$ is limited by $A(\boldsymbol{K_i} - \boldsymbol{Q/2})A^*(\boldsymbol{K_i} + \boldsymbol{Q/2})$, i.e., it is the region of overlap between the two aperture functions separated by $\boldsymbol{Q}$. If $D(\boldsymbol{K_f})$ has a geometry much larger than the probe-forming aperture, the dependence of the $\boldsymbol{K_f}$ integral on $\boldsymbol{K_i}$ becomes very small, allowing the integrals to be separated. The ADF image intensity in reciprocal space then becomes:

$$\begin{aligned}\widetilde{I}_{ADF}(\boldsymbol{Q}) =& \int A(\boldsymbol{K_i} - \boldsymbol{Q/2})A^*(\boldsymbol{K_i} + \boldsymbol{Q/2})d\boldsymbol{K_i} \\ & \cdot \int D(\boldsymbol{K_f})\Psi(\boldsymbol{K_f} - \boldsymbol{K_i} + \boldsymbol{Q/2})\Psi^*(\boldsymbol{K_f} - \boldsymbol{K_i} - \boldsymbol{Q/2})d\boldsymbol{K_f} \\ =& T(\boldsymbol{Q})\widetilde{O}(\boldsymbol{Q}).\end{aligned} \tag{2.3.11}$$

Here, $\widetilde{O}(\boldsymbol{Q})$ is the Fourier transform of the object function, containing the information about the scattering from the specimen to the detector, and $T(\boldsymbol{Q})$ is the optical transfer function (OTF) for incoherent imaging. From the form of $T(\boldsymbol{Q})$ (the first integral in (2.3.11)) one can see that it is the autocorrelation of $A(\boldsymbol{K_i})$ (equation (2.3.5)). The inverse Fourier transform

(IFT) of an autocorrelation function is equal to the square of the modulus of the IFT of the original function. Now, the IFT of $A(\boldsymbol{K_i})$ is the probe function $P(\boldsymbol{R_0})$; thus

$$T(\boldsymbol{Q}) = FT\left\{|P(\boldsymbol{R_0})|^2\right\}. \tag{2.3.12}$$

Hence the ADF image intensity in real space becomes

$$I_{ADF}(\boldsymbol{R_0}) = |P(\boldsymbol{R_0})|^2 \otimes O(\boldsymbol{R_0}), \tag{2.3.13}$$

where $O(\boldsymbol{R_0})$ is the object function in real space. This expression is equivalent to expression (2.3.1), intensity for incoherent imaging; thus it has now been shown that the detector geometry alone gives the desired form for the HAADF STEM image intensity.

The OTF is an important funtion: it is the Fourier transform of the PSF for STEM, and contains information about the effect of aberrations of the probe-forming lens (equation (2.3.4)). According to equation (2.3.13), the image can be thought to be formed as a convolution between the PSF and the object function – hence the resolution of the microscope can be determined from the form of the OTF. In figure 2.7, the OTF is plotted together with the contrast transfer function (CTF) for coherent imaging in CTEM. From the plot it can be seen that the CTF oscillates as a function of spatial frequency $\boldsymbol{Q}$, resulting in contrast reversals with varying thickness and defocus. This is not observed for the OTF, which remains positive.

2.3.2 Contents of HAADF STEM image intensity

While the last section introduced the components of STEM image formation, the current section goes deeper into the contents of the HAADF STEM image intensity using a Bloch-wave approach, which allows the inclusion of dynamical scattering. This approach will eventually give an explanation to why HAADF STEM images of zone-axis lattices have intensities peaked on atomic column sites, and what is the origin of the Z-dependency of the intensity – still considering only coherent Bragg scattering. As it will be seen, the detector geometry plays a significant role in this part as well.

To understand what Bloch waves actually are, we start with the Schrödinger equation for the electron wavefunction $\psi(\boldsymbol{R}, z)$ within the crystal [2]:

$$\left[-\frac{\hbar^2\nabla^2}{2m} - eV(\boldsymbol{R}, z)\right]\psi(\boldsymbol{R}, z) = \frac{4\pi^2 k_0^2\hbar^2}{2m}\psi(\boldsymbol{R}, z) = E\psi(\boldsymbol{R}, z), \tag{2.3.14}$$

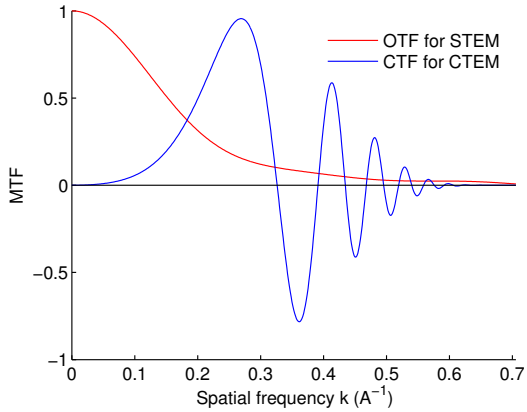

Figure 2.7: The two microscope transfer functions (MTF): CTF for CTEM (blue) and OTF for STEM (red). The parameters used were acceleration voltage $E = 200$ keV, $C_3 = 1.0$ mm, defocus $C_1 = -40$ Å, defocus spread $\Delta = 10$ Å (used only for CTF), illumination semiangle for CTF 0.5 mrad, and aperture semiangle for OTF $\alpha = 8.4$ mrad. The functions were plotted using a MATLAB code from Kirkland [38].

where V is the crystal potential, m is the relativistic electron mass, k_0 is the magnitude of the electron wave vector outside the crystal and E is the kinetic energy of the electron outside the crystal. Here $\boldsymbol{r}$ has been divided into components perpendicular and parallel to the optical axis, $\boldsymbol{R}$ and z, respectively. For the Schrödinger equation we seek a solution in the form of a Bloch wave

$$\phi(\boldsymbol{r}) = \sum_g \Phi_g \exp[-i2\pi((\boldsymbol{k}+\boldsymbol{g})\cdot\boldsymbol{r})]. \tag{2.3.15}$$

A Bloch wave has thus the form of a plane wave exhibiting the periodicity of the lattice; Φ_g are the Fourier components of the wave, determined by the crystal structure.

The electron wave function within the crystal is a linear combination of all the Bloch states $\phi^{(j)}(\boldsymbol{r})$, each weighted with its excitation coefficient $\Phi_0^{(j)*}$, the complex conjugate of the zeroth order Fourier component of the Bloch state in question [2]:

$$\begin{aligned}\psi(\boldsymbol{R}, z, \boldsymbol{K_i}) = &\sum_j \Phi_0^{(j)*}(\boldsymbol{K_i}) \sum_g \Phi_g^{(j)}(\boldsymbol{K_i}) \\ &\cdot \exp\{-i2\pi[(\boldsymbol{K_i}+\boldsymbol{g})\cdot\boldsymbol{R} + k_z^{(j)}(\boldsymbol{K_i})z]\},\end{aligned} \tag{2.3.16}$$

Here also the wave vector has been divided into components perpendicular and parallel to the optical axis, so that $\boldsymbol{k} = \boldsymbol{K} + k_z$. The depth dependency of the wave now lies in the last term in the exponential, where $k_z^{(j)}(\boldsymbol{K_i})$ is the longitudinal component of the wave vector, corresponding to jth Bloch state.

A probe focused on the crystal will excite different Bloch states in it, with probabilities given by the excitation coefficients. Equation (2.3.16) combined with the probe function (2.3.7) will then describe the scattering from the sample, which was earlier in equation (2.3.8) covered with a simple complex multiplier. To derive the form of HAADF STEM intensity, the resulting expression is further integrated over the ADF detector in Fourier space, similarly to the previous section. An expression equivalent to equation (2.3.10) is obtained [2]:

$$\begin{aligned}\widetilde{I}(\boldsymbol{Q}, z) = &\sum_g D_g \int A(\boldsymbol{K_i}) A(\boldsymbol{K_i} + \boldsymbol{Q}) \\ &\cdot \sum_{j,k} \Phi_0^{(j)*}(\boldsymbol{K_i}) \Phi_Q^{(k)}(\boldsymbol{K_i}) \Phi_g^{(j)}(\boldsymbol{K_i}) \Phi_g^{(k)*}(\boldsymbol{K_i}) \\ &\cdot \exp\{-i2\pi z[k_z^{(j)}(\boldsymbol{K_i}) - k_z^{(k)}(\boldsymbol{K_i})]\} d\boldsymbol{K_i}.\end{aligned} \tag{2.3.17}$$

Here the first summation is over all the Bragg beams g incident on the detector. This summation acts only on a product pair of Bloch wave Fourier coefficients [2]:

$$C_{jk}(\boldsymbol{K_i}) = \sum_g D_g \Phi_g^{(j)}(\boldsymbol{K_i}) \Phi_g^{(k)*}(\boldsymbol{K_i}). \tag{2.3.18}$$

Hence strong contributions to the intensity can only come from Bloch states that have frequency components that extend to the detector [50]. This implies states that are broad in reciprocal space, therefore narrow in real space – that is, the 1s states. How electrons in different Bloch states are distributed around atoms in a lattice is illustrated in figure 2.8.

With the notation of (2.3.18), the intensity becomes

$$\begin{aligned}\widetilde{I}(\boldsymbol{Q}, z) = &\int A(\boldsymbol{K_i}) A(\boldsymbol{K_i} + \boldsymbol{Q}) \sum_{j,k} C_{jk}(\boldsymbol{K_i}) \Phi_0^{(j)*}(\boldsymbol{K_i}) \Phi_Q^{(k)}(\boldsymbol{K_i}) \\ &\cdot \exp\{-i2\pi z[k_z^{(j)}(\boldsymbol{K_i}) - k_z^{(k)}(\boldsymbol{K_i})]\} d\boldsymbol{K_i}.\end{aligned} \tag{2.3.19}$$

An essential bit here lies in the difference between the diagonal terms, C_{jj}, and the cross terms, C_{jk}. The diagonal terms involve only one Bloch-state, whereas the cross-terms involve multiple Bloch states, as can be read from

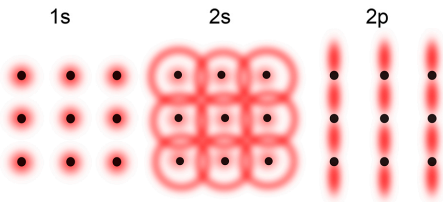

Figure 2.8: A schematic illustration of how electrons in the first three Bloch states are distributed around atoms in a lattice. (Redrawn after [48].)

equation (2.3.18). For the diagonal terms, the exponential term holding the thickness dependency in equation (2.3.19) is unity. Thus the diagonal terms are thickness-independent, while the contribution of cross-terms decreases exponentially with increasing thickness. Hence, with increasing thickness, contribution from only single Bloch states becomes significant.

Now, what we want to see is intensity maxima localized on the atomic sites – thus we want scattering from localized Bloch states, that is the 1s states. Fortunately, it is the 1s states that the HAADF detector will allow us to see. Evaluating (2.3.18) using a real space representation of the Bloch states and assuming an infinite detector except for a circular hole yields [30]

$$C_{jk}(\boldsymbol{K_i}) = \delta_{jk} - \int \frac{J_1(2\pi u_{in}|\boldsymbol{B}|)}{2\pi|\boldsymbol{B}|} \int \phi^{(j)}(\boldsymbol{K_i}, \boldsymbol{C})\phi^{(k)*}(\boldsymbol{K_i}, \boldsymbol{B}+\boldsymbol{C})d\boldsymbol{C}d\boldsymbol{B}. \tag{2.3.20}$$

This integral looks absolutely terrible, but let's still try to understand the physics in it. Firstly, the variables: J_1 is the first order Bessel function of the first kind, u_{in} is the inner radius of the detector in reciprocal space, and $\boldsymbol{B}$ and $\boldsymbol{C}$ are dummy real-space integration variables. The meaning of the Bessel function part, which is the Fourier transformation of the hole in the detector, is that it acts as a coherence envelope, controlling to which degree different Bloch waves can interfere. A detector that spans over a wide angular range produces a small coherence envelope in real space, allowing only states that are sharply peaked on atomic column positions to contribute to the image [30, 48]. With for instance $u_{in} = 30$ mrad and $\lambda = 1.9$ pm, the Bessel term has its first zero at $|\boldsymbol{B}| = 0.04$ nm, so the domain of the integral in (2.3.20) is extremely limited [2].

We have now shown that HAADF imaging of zone-axis lattice images actually yields intensities peaked on the atomic column sites – but we still need to explain the Z-dependency. Luckily this step is not too far away. For $j = k$, also for the diagonal states, the integral (2.3.20) can be written as

[30]

$$C_{jj} \propto \langle \phi^{(j)}(\boldsymbol{K_i})|T|\phi^{(j)}(\boldsymbol{K_i})\rangle, \tag{2.3.21}$$

that is, C_{jj} is proportional the the expectation value for the transverse kinetic energy T for the jth Bloch state. Thus states with high transverse kinetic energy will scatter more strongly on the detector. Atomic columns with higher Z will have 1s states with higher transverse kinetic energy, and this is the origin of the Z-dependency of the image intensity [2, 30].

2.3.3 The contribution of thermal diffuse scattering

So far we have only considered the contribution of coherent Bragg scattering on the ADF detector. At high scattering angles, the scattered intensity is however dominated by electrons scattered by phonons, i.e., crystal vibrations, which in the case of a specimen in a TEM arise from thermal vibrations of the atoms. Scattering of electrons by phonons lead to a diffuse background intensity in the diffraction pattern, and is thereby generally referred to as thermal diffuse scattering (TDS). Furthermore, electrons scattered by phonons have random phases – i.e., they are incoherent. It is hence understandable that the early derivations for HAADF STEM intensity formation took as a starting point electrons scattered by phonons [1], rather than coherently scattered electrons as in the derivation above. Strangely – or conveniently – enough, both approaches yield intensity peaked on atomic sites, and dependent on the atomic number Z.

The scattering by phonons can be described as absorption: the electrons are absorbed, i.e., scattered to high angles, by phonons as they penetrate through the lattice. Mathematically, absorption is taken into account by adding an imaginary component into the projected lattice potential $V(\boldsymbol{R})$. The total projected potential then becomes [1]

$$V_{tot}(\boldsymbol{R}) = V(\boldsymbol{R}) + iV'(\boldsymbol{R}), \tag{2.3.22}$$

where $V'(\boldsymbol{R}) = V'(x, y)$ is the (projected) absorptive potential, leading to loss of electrons by absorption. The intensity for TDS scattering, i.e., loss of electrons by absorption, is given by [1]

$$I^{TDS} = \frac{2}{\hbar v} \int |\psi(\boldsymbol{r})|^2 V'(\boldsymbol{R}) d\boldsymbol{r}, \tag{2.3.23}$$

where $\psi(\boldsymbol{r}) = \psi(x, y, z)$ is the total electron wave function and v is the electron velocity. It can further be shown that the electrons scattered into high angles by phonons are scattered from states strongly localized to atomic

positions – the 1s Bloch states – and that the scattered intensity is higher for atoms with high Z [1].

Now, what we are really interested in is finding out what is the portion of TDS with respect to the coherent scattering incident on the ADF detector. According to the previous section (2.3.2), the coherent signal falling on the ADF detector is primarily scattering from the 1s states, which can be simplified into [30]

$$I_{coh}(t) \propto e^{-\sigma t}[1 - \cos(\zeta t)], \tag{2.3.24}$$

where t is the specimen thickness, σ is the absorption coefficient and ζ is the thickness frequency for the 1s states. The absorption coefficient determines the absorption of the wave function by phonons, and the thickness frequency is the rate of change of the phase of the wave function along the depth of crystal. To evaluate the effect of TDS, this expression is integrated over thickness, giving [30]

$$I_{TDS}(t) \propto (1-e^{-\sigma t}) - \left(1 + \frac{\sigma^2}{\zeta^2}\right)^{-1} \left[\frac{\sigma}{\zeta} e^{-\sigma t} \sin(\zeta t) + \frac{\sigma^2}{\zeta^2}(1 - e^{-\sigma t} \cos(\zeta t))\right]. \tag{2.3.25}$$

From this expression it can be read that with increasing thickness the sinusoidal terms will be suppressed and the intensity approaches unity, which is verified in the plot in figure 2.9. The total intensity can be calculated by defining the fraction of coherent to incoherent scattering as α so that [30]

$$I_{ADF}(t) = I_{TDS}(t) + \alpha I_{coh}(t), \tag{2.3.26}$$

which is also plotted in figure 2.9. From the plot it is evident that with $\alpha = 0.17$ (chosen after [30]), TDS dominates the intensity at thicknesses above ~ 20 nm.

In the previous section it was shown how the detector geometry only allows scattering from single electronic states localized around atomic positions to contribute to the HAADF intensity. Hence the detector geometry destroys transverse coherence, i.e., coherence of the electron wave functions between adjacent columns. Phonon scattering on the other hand plays an important role in destroying longitudinal coherence. Electrons scattered by phonons have random phases, and are no longer in phase with the propagating electron wave field [48]. The destruction of longitudinal coherence, i.e., intracolumn interference, is important for determination of elemental composition of the specimen along the depth of the specimen, such as locating substitutional atoms in the columns. However, destruction of coherence is much less complete in longitudinal than in transverse direction [30].

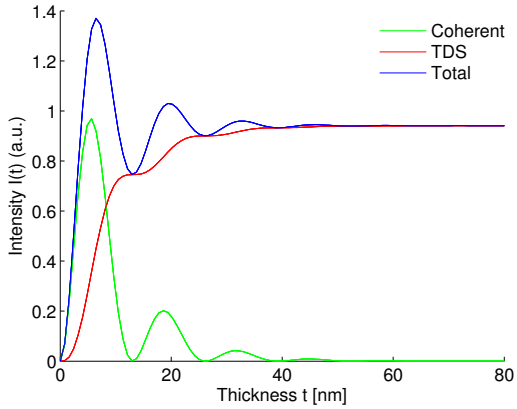

Figure 2.9: The contributions of coherent and thermal diffuse scattering falling on the ADF detector, as well as the total intensity, according to equations (2.3.24), (2.3.25) and (2.3.26). (Replotted after [30].)

In this section we have shown that at normal specimen thicknesses, TDS dominates the scattering on the ADF detector, and that the phonons conveniently pick the wave functions scattered from the 1s states, freeing them from the wave field propagating through the lattice and thus breaking the coherence in longitudinal direction. One could then say that "the 1s state puts the electron wave function onto the detector, but it is phonon scattering that keeps it there" [48].

2.4 Image simulations with multislice approach

Image simulation means numerically calculating the microscope images from a detailed description of the specimen and the instrument [38]. Simulations are required for quantitative interpretation of the image intensity: for mapping the specimen thickness [8, 9] and composition [7, 6], and for understanding the effects of probe characteristics and microscope aberrations on the image [46, 51]. For STEM image simulations, two main approaches exist: multislice and Bloch-wave approach. The principles of the Bloch-wave approach were essentially given in section 2.3.2. This approach treats the scattering process more physically, and it has been widely used for understanding the STEM image formation using simple model structures [2, 52, 53, 54]. In the Bloch wave approach however the HAADF intensity might be underestimated at higher specimen thickness as will be discussed in section 2.4.2, and it is difficult to apply to non-perfect crystals [54]. Multislice approach is

better suited for simulating STEM image intensities for real specimens and is therefore more widely applied for solving materials problems by quantitative STEM [4, 9, 32, 55]. The image simulations for the present work were all performed with programs based on the multislice approach, and hence it is this approach that will be focused on here.

2.4.1 Principles of the multislice approach

To simulate HAADF STEM image intensities for a certain crystal, first a supercell modelling the crystal has to be constructed. A supercell is an extended crystal unit cell in the orientation of concern. In practice a text file containing a list of the atomic positions, as well as the atomic numbers, Debye-Waller factors and occupancies for each atomic position has to be generated. In the multislice approach, the supercell is divided into thin (ideally one atomic layer, $1 - 2$ Å) slices in the direction of the electron beam, and for each slice a projected potential is calculated – the scattering properties of a slice are thus "pressed" into a plane. The incident electron wave function is then alternately transmitted through the slices and propagated through the gaps (vacuum) between the slices, as is illustrated in figure 2.10. Mathematically this can be expressed as [38]

$$\psi_{n+1}(x,y) = p_n(x,y,\Delta z_n) \otimes [t_n(x,y)\psi_n(x,y)], \tag{2.4.1}$$

where $\psi_n(x,y)$ is the wave function at the top of slice n and $t_n(x,y)$ and $p_n(x,y,\Delta z)$ are the transmission and propagator functions, respectively, for the slice. The initial wave function $\psi_0(x,y)$ is the STEM probe wave function, which was introduced in section 2.3.1. The transmission function for the specimen portion between z and $z + \Delta z$ is:

$$t(x,y,z) = \exp\left[i\sigma v_{\Delta z}(x,y,z)\right] = \exp\left[i\sigma \int_z^{z+\Delta z} V(x,y,z')dz'\right], \tag{2.4.2}$$

where $v_{\Delta z}(x,y,z) = \int_z^{z+\Delta z} V(x,y,z')dz'$ is the projected potential for a slice with thickness Δz and σ is the interaction parameter, dependent on the energy of the incident electrons. The propagator function is best expressed in reciprocal space:

$$P(k,\Delta z) = \exp(-i\pi\lambda k^2 \Delta z). \tag{2.4.3}$$

Physically, the propagator function can be associated with the Fresnel (near-field) diffraction over a distance Δz. To minimize computing time, the Fourier transformed form of equation (2.4.1) is generally applied so that

the fast Fourier transform (FFT) algorithm can be exploited. Using the convolution theorem, (2.4.1) becomes

$$\psi_{n+1}(x,y) = FT^{-1}\{P_n(k_x,k_y,\Delta z_n)FT[t_n(x,y)\psi_n(x,y)]\}. \qquad (2.4.4)$$

At the end, when the wave function has propagated through the specimen, the final wave function is integrated over the ADF detector in reciprocal space to calculate the intensity for the point on the supercell in question.

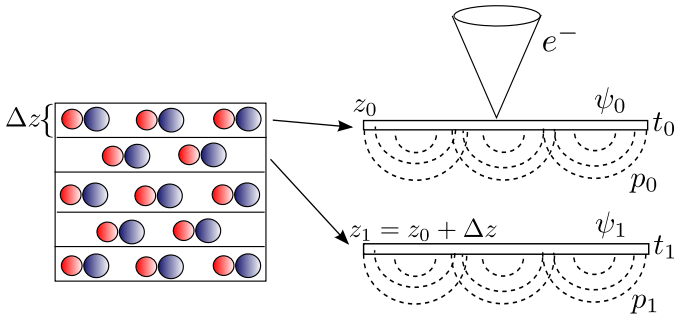

Figure 2.10: The principles of the multislice approach. The supercell, describing the specimen in the orientation in concern, is divided into thin (Δz) slices (left). For each of the slices, a projected potential is formed, and the electron wave function ψ is alternately transmitted (t) through the slices and propagated (p) through the vacuum between the slices (right).

For accurate image simulations, correct sampling of the input functions – i.e., the incident wave function, and the transmission and propagator functions – is crucial. A large enough supercell has to be created, and the supercell has to be sampled with a sufficient number of pixels to avoid artefacts. Moreover, the sampling density determines the smallest spatial frequency and thereby the largest scattering angle included in the calculations, and it is important that high enough sampling is employed such that the largest scattering angle exceeds the outer angle of the ADF detector in question. A thorough description about the required sampling conditions is given by Kirkland in [38].

Several different multislice simulation programs were applied for the HAADF STEM image simulations in the course of this PhD. For the simulations for Paper IV, a program by C. Dwyer called STEMimg [56] was used. As most multislice programs available, STEMimg is based on the code by Kirkland [38], but it has been made very efficient by exploiting parallel computing possible on a graphical processing unit (GPU). For simulations for Papers I-III, a multislice program by A. Rosenauer, STEMsim [57], was applied. STEMsim cannot compete with STEMimg in speed, however it allows

inclusion of static atomic displacements (SAD) that can affect the HAADF STEM image intensity for certain materials (see section 2.4.3). Perhaps the most user-friendly multislice simulation program currently available for HAADF STEM image simulations is qSTEM by C. Koch [58], which was used at the start of this PhD. While STEMimg requires a computer with a GPU and STEMsim requires a Linux cluster, qSTEM can be run on a normal desktop computer, and it has an intuitive graphical user interface. qSTEM additionally permits relatively easy simulation of interfaces and complex super structures, however it is not as efficient as STEMimg and does not allow inclusion of SAD as STEMsim does.

2.4.2 Simulating thermal diffuse scattering

The most common way to include TDS in multislice simulations is the frozen phonon approach [59]. Phonons vibrate relatively slowly: the duration of one vibration period for an optical (transverse) phonon is in the order of 10^{-13} s, and acoustic (longitudinal) phonons, which produce most of the atomic displacement, vibrate even more slowly. An electron with kinetic energy of 100 keV travels with a speed of $1.5 \cdot 10^{18}$ Å/s, and the electron/atom interaction time can be estimated to be $\sim 2 \cdot 10^{-2}$ vibration periods [59]. Hence one electron sees a somewhat frozen view of the lattice; however for the next electron, the picture has changed a little due to the lattice vibrations. In the frozen phonon approach, the multislice calculation is performed several times and for each run the position of each atom in the specimen is shifted slightly. The final image is taken as an average over the different calculations.

In practice, the correlations between the atomic vibrations are generally not considered but each atom is assumed to vibrate independently with an amplitude related to its Debye-Waller factor – this is known as the Einstein model for TDS [1]. It has been shown that this is a good approximation for STEM image calculations [60], and the Einstein model is therefore applied for simulating TDS in most multislice programs. The approach would hence be more correctly referred to as the frozen lattice rather than the frozen phonon approach [4], however the generally the latter term is used even if Einstein model is applied. As is conventional, I will henceforth use the term frozen phonon approach.

To realistically include the effect of TDS with the frozen phonon approach, several runs with different atomic configurations are required (20 has been suggested [54]), resulting in long computation times. An alternative, analytic approach, is based on the absorptive potentials discussed in section 2.3.3 [61, 62]. With this approach, the required times for simula-

tions are dramatically shorter (even 1/60 of the times required for frozen phonon multislice simulations [54]). The analytic approach is taken when including TDS in Bloch wave simulations, and it is used in some multislice programs as well [61, 63]. In STEMsim both approaches are implemented, but the simulations performed for the present work (using STEMsim and STEMimg) were all done using the frozen phonon approach. The analytic approach excludes multiple scattering events after a single phonon scattering event (absorption by a phonon), and hence the HAADF intensity might be underestimated at higher specimen thicknesses ($\gtrsim$ 50 nm) [64]. On the other hand the frozen phonon model naturally includes multiple sequential scattering events.

2.4.3 Static atomic displacements

When atoms having different covalent or ionic radii are present in a crystalline alloy, a type of static disorder called static atomic displacements (SAD) will be present in the lattice [65]. For instance replacing an As atom in GaAs by Sb causes displacements in the neighboring atoms due to the larger covalent radius of Sb. As TDS, caused by temporally varying shifts in atomic positions, this kind of static disorder can also result in increased diffuse scattering to high angles [66, 67, 68].

The effect of SAD in the simulated HAADF STEM image intensities was first studied by Grillo et. al. [67], for the case of $In_xGa_{1-x}As$, and subsequently by Rosenauer et. al. [7], for $In_xGa_{1-x}N$. In Paper I in this thesis, the effect of SAD on the HAADF intensity in the case of $GaAs_{1-y}Sb_y$ is demonstrated. All of these studies concluded that SAD have to be included in the image simulations for accurate quantification of the experimental intensities. One of the few III-V alloys virtually free of SAD is $Al_xGa_{1-x}As$ [69], which was studied in Paper IV. This difference between the different alloys in terms of SAD can be understood from the differences in covalent radii for atoms sharing the same sublattice. For $Al_xGa_{1-x}As$, the covalent radii of Al and Ga is very similar (1.21 and 1.22 Å, respectively [70]), while this is not the case for As and Sb in $GaAs_{1-y}Sb_y$, (1.19 and 1.39 Å for As and Sb, respectively [70]).

To compute the SAD, the elastic constants of the atoms in the studied crystal structure have to be known. For simulating $GaAs_{1-y}Sb_y$ in Papers I-III, the SAD were implemented by relaxation using the valence force field method, and the relaxations were done using Keating potentials [71]. Primarily due to the complexity related to implementing the SAD, the simulations for $GaAs_{1-y}Sb_y$ with the STEMsim program were mostly performed by T. Grieb at the University of Bremen, Germany.

2.4.4 Simulations for compositional analysis: the CT-matrix

For compositional analysis of a ternary alloy, HAADF STEM images are simulated for different concentrations x of the alloying element, with a certain thickness step up to the desired thickness. In the present work, experimental image intensities averaged over a unit cell (Paper IV) or a larger area (Papers I-III) were employed in the compositional analysis (see section 2.5.3). Using simulated intensities averaged over a unit cell (or supercell) for different thicknesses and concentrations, a matrix for the simulated intensity as a function of thickness and concentration – concentration-thickness (CT) -matrix – was constructed by cubic interpolation. This matrix was used as a database when quantifying the experimental image intensities. The CT-matrix for the two material systems studied in the present work, $GaAs_{1-y}Sb_y$ and $Al_xGa_{1-x}As$, is presented in figures 2.11(a) and 2.11(b), respectively. The simulations for [110] $GaAs_{1-y}Sb_y$ were performed for an acceleration voltage of 200 kV and an ADF detector spanning an angular range of 29-114 mrad (parameters for JEOL 2010F). For [111] $Al_xGa_{1-x}As$, an acceleration voltage of 300 kV, and an angular range of 46-200 mrad for the ADF detector (parameters used at FEI Titan^3 80-300) were employed.

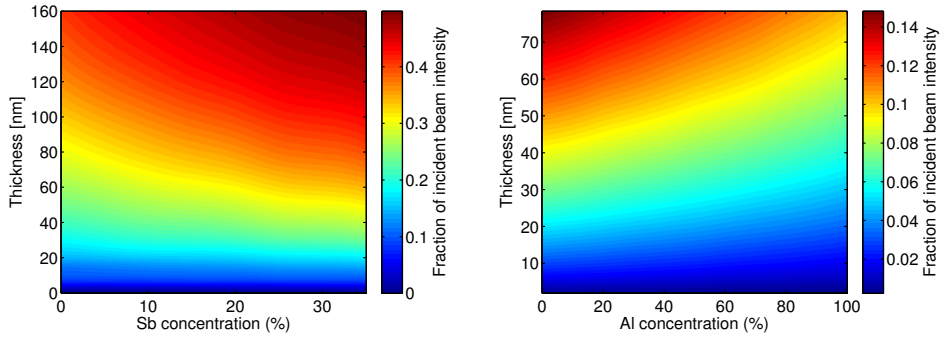

(a) (b)

Figure 2.11: Simulated HAADF STEM intensity as a function of thickness and alloy concentration, i.e., the CT-matrix, for (a) [110] $GaAs_{1-y}Sb_y$ and (b) [111] $Al_xGa_{1-x}As$. Note the different range for concentrations and thicknesses in (a) and (b), chosen after the studied material problem: the Sb concentration was studied in $GaAs_{1-y}Sb_y$ inserts and NWs in plane, with thickness ranging from 50 to 160 nm and Sb concentration being generally below 30%; the Al concentration was studied in cross-sectioned NWs, with thickness ranging from 20 to 80 nm and Al concentration from 0 to 100%.

2.5 Quantitative HAADF STEM

2.5.1 Normalization to the incident beam intensity

The goal in quantitative HAADF STEM imaging is mapping either the specimen composition [6, 7, 55] or thickness [8, 9]. To do this, the experimental image intensities are compared with simulated intensities in order to verify, which intensity level in the image corresponds to a certain thickness and composition in the real specimen. In the image simulations, the incident beam intensity is normalized to one, and the resulting intensities are given as a fraction of the incident intensity. Consequently, the experimental images need to be normalized to the incident beam intensity prior to the comparison. This can be accomplished by scanning the detector directly with the incident beam, which was first demonstrated by LeBeau and Stemmer [3], using an external amplifier to obtain a larger dynamical range. Shortly after that, Rosenauer et. al. [4] did the same without an external amplifier, and introduced a useful expression for normalizing the images:

$$I_{norm} = \frac{I_{raw} - I_{vac}}{I_{det} - I_{vac}}, \tag{2.5.1}$$

where I_{raw} is the raw image intensity, I_{vac} is the vacuum (dark) intensity of the detector and I_{det} is the average intensity over the ADF detector in the absence of a specimen. I_{vac} and I_{det} depend on the offset and gain (brightness and contrast) settings of the detector, respectively, which are usually varied between and during imaging sessions. Hence a detector scan image has to be acquired at each HAADF STEM imaging session aiming for quantitative intensity analysis, with the same offset and gain settings as used for imaging. Example detector scan images from JEOL 2010F and FEI Titan^3 80-300 are shown in figures 2.12(a) and (b), respectively.

Performing the detector scan

When doing STEM in a TEM/STEM instrument, the microscope is operated in diffraction mode, as was explained in section 2.1.2. To obtain a detector scan image, the microscope has to be operated in imaging mode. At the FEI Titan^3 80-300, which was used for the quantitative HAADF STEM study in Paper IV, this is done simply by switching off diffraction by pressing a button. At the JEOL 2010F, which was used for the quantitative HAADF STEM work in Papers I-III, this is done by manually changing the settings of the intermediate and projector lenses to values corresponding to the TEM mode. The optimal values for producing a good detector image

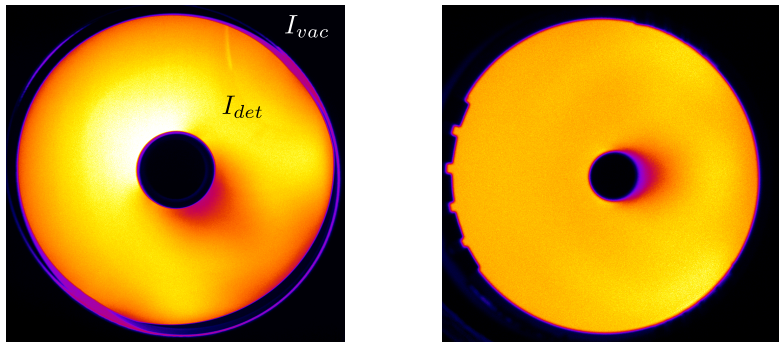

(a) (b)

Figure 2.12: A detector scan image from (a) JEOL 2010F at NTNU, acquired by the author and (b) FEI Titan^3 80-300 at MCEM, Australia, acquired by Changlin Zheng.

were found by trial and error, and are given in table 2.1 together with the respective values for STEM and TEM modes. Additionally, the detector image had to be shifted to the centre using projector shifts and the value for differential voltage (DV) had to be adjusted from the optimum for HR STEM of -22 down to approximately -9 in order to get a focused image.

Table 2.1: The intermediate and projector lens settings in hexadecimals at the JEOL 2010F for TEM mode at 30k magnification, for doing the detector scan and for STEM mode.

Lens	TEM 30k	STEM detector scan	STEM mode
Intermediate lens 1	8520	8520	5223
Intermediate lens 2	4CF0	4CF0	AE00
Intermediate lens 3	BD90	8700	8700
Projector lens	FF00	FF00	FA00

At the JEOL 2010F, the detector scan was always performed prior to the imaging, in order to ensure that the gain and offset were at an optimal range. The offset was set to yield a vacuum intensity of approximately $1 \cdot 10^4$, and the gain was set to give an average detector intensity of $4 \cdot 10^4$, ensuring that the maximum intensity on the detector did not exceed $5 \cdot 10^4$ [4]. On a probe-corrected instrument, the incident beam is much stronger than the high angle signal on the detector, and the detector might be saturated if the same incident beam as used for imaging directly scans the detector. In

order to avoid saturating and damaging the detector, in Paper IV a smaller condenser lens aperture was used to form a relatively low intensity beam to scan the detector, however keeping the gain and offset settings the same. The intensity difference between the two probes applied for imaging and detector scan, formed with different condenser lens aperture sizes, was calibrated with a CCD camera and taken into account in the image normalization.

Detector non-uniformity

As can be seen from figure 2.12, the detector response is not uniform. Rosenauer et.al. [4] have suggested taking this into account in the image simulations by applying a radially averaged detector sensitivity profile, shown in figure 2.13(a) for the ADF detector at JEOL 2010F, when calculating the signal falling on the detector. This option is included in STEMsim. Findlay and LeBeau [72] have studied the effect of detector non-uniformity in the intensity quantification, concluding that in the high angle DF region, assumption of a uniform detector is valid, whereas in the low angle DF region and in the case of ABF STEM, the detector non-uniformity should be taken into account in the simulations. In the present work, for quantitative HAADF STEM work at JEOL 2010F (Papers I-III), image simulations both with and without considering the detector non-uniformity were conducted with STEMsim. Best fit with pure GaAs intensities at a known thickness was generally obtained with simulations assuming a uniform detector response, despite the relatively low angles employed at the JEOL 2010F (see the discussion below). Hence the detector non-uniformity was not considered in the simulations for Papers I-III. Whether the detector non-uniformity was included in the simulations or not had however a negligible effect on the final concentration determination, when analysis based on the intensity ratio was employed (see section 2.5.2). Detector non-uniformity was not included in the STEM image simulations for Paper IV either.

A word on the detection angles

The quantitative HAADF STEM work at the JEOL 2010F was performed employing detector inner and outer angles of 29 and 114 mrad (corresponding to a camera length of 25 cm). When increasing the detection angles, i.e., lowering the camera length, a systematic mismatch between simulated and normalized experimental image intensities was observed (figure 2.13(b)). We attribute this to an internal limiting aperture. Nevertheless, the images acquired with these settings are incoherent: no contrast reversals are observed with change in defocus or thickness. From figure 2.11(a) it can be seen that

the intensity increases monotonically as a function of thickness. According to Hartel [73], for incoherent imaging a detector inner angle at least three times the probe convergence angle should be employed, and this condition is fulfilled: the probe convergence angle employed was 8.4 mrad.

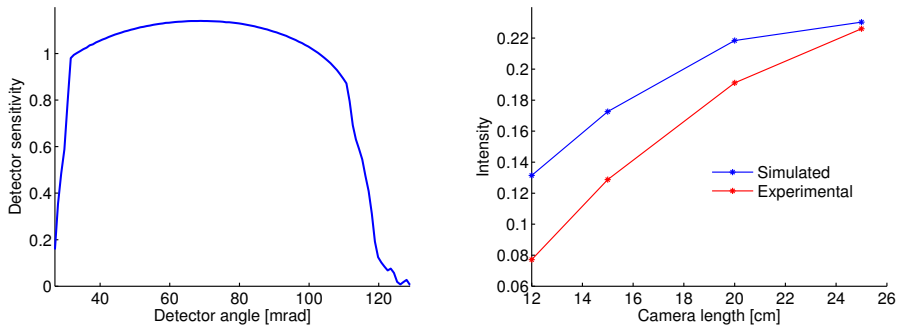

(a) (b)

Figure 2.13: (a) Radially averaged detector sensitivity profile of the ADF detector at JEOL 2010F, generated by T. Grieb. (b) Average simulated and normalized experimental intensities as a function of camera length on JEOL 2010F for WZ GaAs at a thickness of 47 nm. The experimental intensities were obtained from a WZ GaAs segment in a GaAs/GaAsSb NW, and the simulations were performed with the STEMimg software.

2.5.2 Analysis based on the intensity ratio

With quantitative HAADF STEM, often a system with an alloy of unknown composition embedded in a known matrix is studied [4, 55, 67, 74]. In such cases it is common to do the compositional analysis using an intensity ratio I_x/I, where I_x and I are intensities for the regions with unknown and known composition in the HAADF STEM image, respectively. The experimental intensity ratio is then compared with a simulated intensity ratio for different concentrations x, at the specific thickness. This mitigates errors associated with for instance the measurement of thickness, as will be demonstrated below. Furthermore, the intensity ratio is independent of the incident beam intensity: the dependency on I_{det} in equation (2.5.1) vanishes when the ratio is used. This implies that the detector scan is not necessarily needed, as I_{vac} can be determined simply by scanning vacuum. Using the intensity ratio might further reduce errors associated with the non-uniform detector response.

Consequently, in some quantitative HAADF STEM approaches the normalization of experimental images to the incident beam intensity is omitted and the analysis is performed from the basis of the intensity ratio alone [75, 76, 77, 78]. However, if the specimen thickness is not known from other methods, it can be determined from the normalized experimental image intensity at an area of known composition by comparison with simulated intensities. In the present work, in Papers I-III the thickness of the specimen (NW) could be determined with high precision from the NW width in the TEM images, assuming a hexagonal shape. Comparison of simulated and normalized experimental intensities at the pure GaAs region however served as a valuable verification for the quantification approach. In Paper IV, the specimen thickness (NW cross-section) was determined from the basis of normalized experimental intensities at the pure GaAs region.

In figures 2.14(a) and 2.14(b), the CT-matrices for [110] $GaAs_{1-y}Sb_y$ and [111] $Al_xGa_{1-x}As$ (see figure 2.11), respectively, are plotted relative to the GaAs signal (I_{GaAs}). These two systems are clearly very different. In the case of $Al_xGa_{1-x}As$, I/I_{GaAs} is nearly constant as a function of thickness for thicknesses above ~ 30 nm for the entire concentration range (figure 2.14(d)), and has an almost perfectly linear dependency on concentration for the thicknesses concerned (figure 2.14(f)). For $GaAs_{1-y}Sb_y$ on the other hand, I/I_{GaAs} is no longer flat as a function of thickness for Sb concentrations above 20% (figure 2.14(c)), and the dependency on concentration is more complex than in the case of $Al_xGa_{1-x}As$ (figure 2.14(e)). An obvious reason for these differences is the absence of strain and SAD in $Al_xGa_{1-x}As$: the difference in lattice parameter between AlAs and GaAs is 0.0078 Å (0.14%) [79], and the effect of SAD is negligible due to the similar covalent radii of Al and Ga, as was explained in section 2.4.3. For $GaAs_{1-y}Sb_y$, the difference in lattice parameter between GaSb and GaAs is is 0.443 Å (7.8%) [80], and the effect of SAD on the HAADF STEM intensity is significant. The crystal orientation might also have an effect since the channelling conditions are different [46], and the angular extent of low-order Bragg reflections is different for different orientations as well. The CT-matrix for $GaAs_{1-y}Sb_y$ in figure 2.14(a) is qualitatively similar with an equivalent matrix for $In_xGa_{1-x}As$ (also affected by SAD) at the same orientation presented in [81], simulated with different instrument parameters. Finally, the lower detection angles employed at the JEOL 2010F when studying $GaAs_{1-y}Sb_y$, discussed in the previous section, might have had an effect, allowing more contribution from coherent scattering on to the detector and hence yielding a more complex behaviour for the HAADF intensity as a function of thickness and composition.

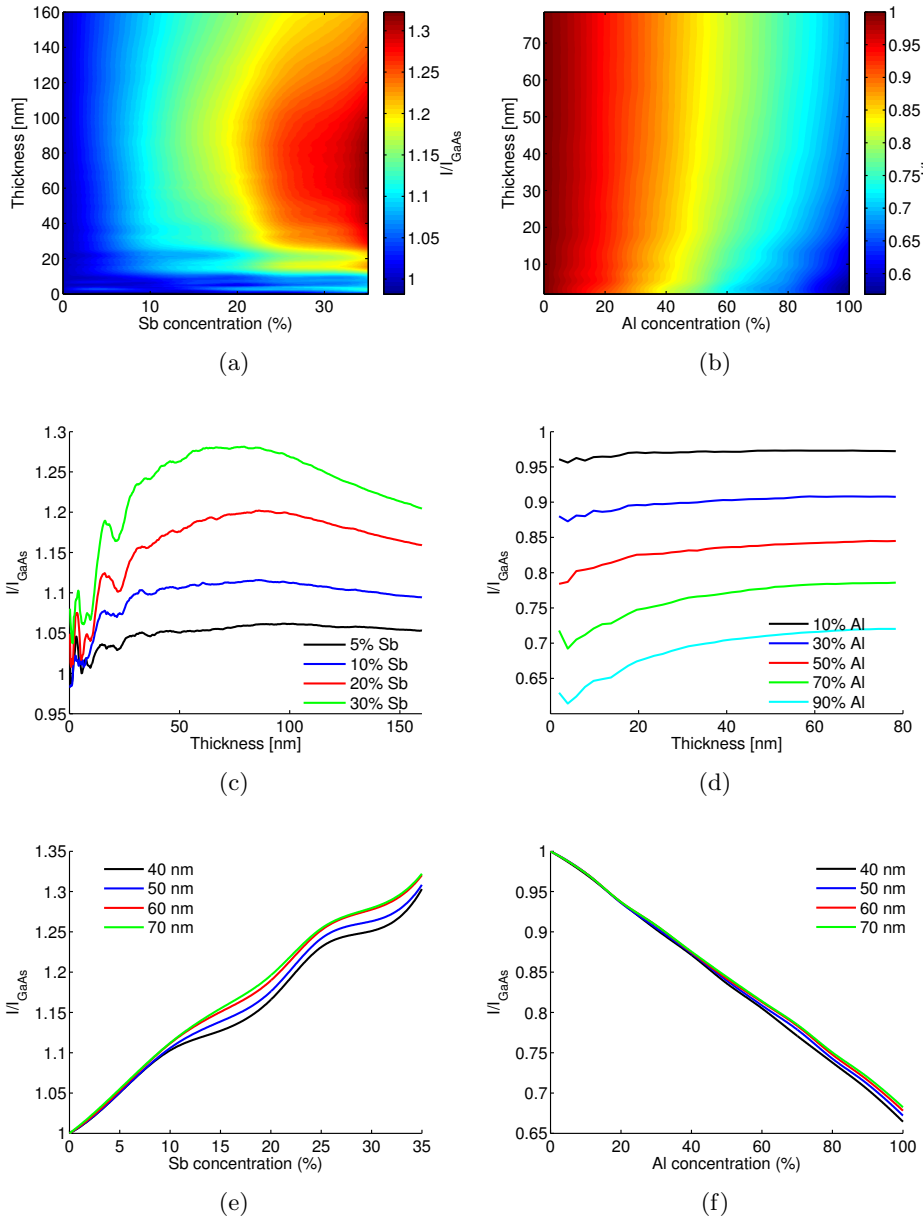

Figure 2.14: Simulated intensity relative to the GaAs signal (I/I_{GaAs}) for [110] $GaAs_{1-y}Sb_y$ (left) and [111] $Al_xGa_{1-x}As$ (right). (a), (b) The CT-matrix (see figure 2.11) normalized to I_{GaAs}; and I/I_{GaAs} as a function of (c), (d) thickness for certain concentrations and (e), (f) concentration for certain thicknesses. Note the different range for concentrations and thicknesses for $GaAs_{1-y}Sb_y$ and $Al_xGa_{1-x}As$.

2.5.3 Averaged intensities vs. column-by-column analysis

In Papers I-III, the experimental images were acquired at a relatively low magnification, and intensities averaged over a larger region across a NW were employed in the quantitative analysis. In Paper IV, experimental intensities averaged over a unit cell region were employed. The average experimental intensities were quantified by comparison with average simulated intensities in a CT-matrix, as was explained in section 2.4.4. In principle, the availability of aberration correction allows column-by-column compositional mapping from the atomic resolution images. The analysis based on averaged intensities has however certain advantages.

Firstly, despite the apparent atomic resolution in HAADF STEM images acquired with aberration corrected instruments, at thicknesses above $\sim$ 30 nm the signal at an atomic column position will have contributions from neighboring columns as well due to dynamical scattering of the electron probe [46, 82, 83]. This effect is strongly enhanced with higher probe convergence angles employed in aberration corrected instruments [46]. Hence, if atomic column resolution compositional analysis is desired, the specimen should be very thin.

Secondly, in experimental atomic resolution HAADF STEM images, the contrast is always lower than in the simulated images, and a diffuse background signal is present. This is due to probe spreading and spatial incoherence, which can be defined as the combined effect of the finite source size, mechanical and electrical instabilities, sample drift etc. [64]. Earlier it was suggested that in order to perform quantitative comparisons between simulated and experimental images at an atomic column resolution, the background signal should be subtracted from the experimental image intensity [84, 85]. In the pioneering work by LeBeau et. al. [64], quantitative agreement between simulated and normalized experimental images at atomic resolution was finally obtained – after the effect of spatial incoherence had been included in the simulated images by convolving the images with a Gaussian envelope function. The standard deviation of the Gaussian depends on the instrument parameters; for aberration corrected instruments primarily on the effective source size [51]. To determine these parameters and to find the correct standard deviation is not an easy task [56, 86, 87]. If the intensity analysis is done from the basis of averaged intensities instead, these parameters do not need to be considered [88]. This decreases the number of parameters to be determined and incorporated in the image quantification significantly, and the errors associated with the measurement of these parameters are avoided.

2.6 Conclusions and outlook: Quantitative HAADF STEM

Quantitative HAADF STEM is not a straightforward tool for compositional analysis. It requires rigorous image simulations, and to perform the simulations, a number of specimen and instrument parameters needs to be known accurately. Image normalization is not necessarily an easy task either, as became clear from section 2.5.1; although once the procedure has been established, it can be applied repeatedly. On the other hand in energy dispersive X-ray spectroscopy (EDX), which is undoubtedly the most applied method for compositional analysis in TEM, the software spits out a composition with a push of a button. So why bother to do the efforts required by quantitative HAADF STEM, when such an easy method is available?

Firstly, the spatial resolution of compositional analysis by quantitative HAADF STEM is high: with an aberration corrected instrument atomic or unit cell resolution can be obtained, depending on the specimen thickness as was discussed in section 2.5.3. The resolution of EDX is limited to a few nanometers due to the large sampled volume (see section 3.3.3). Secondly, HAADF STEM intensity is sensitive for very small changes in composition: in the case of heavy elements in a light matrix, single atom sensitivity has been obtained [89, 90]. Thirdly, as opposed to EDX, the signal acquisition time is very short, minimizing the effects of specimen drift and mechanical instabilities, as well as the electron dose and damage to the specimen. Another widely applied method for high-resolution compositional analysis in STEM is electron energy loss spectroscopy (EELS), and this method has certain benefits. It however requires significantly more complex instrumentation than what is required in HAADF STEM, and compositional analysis of certain materials is hindered by peak overlap (see section 3.3.3). Finally, through the simulations and the quantification process, a lot of understanding about the material and the instrument is gained. In the long term, this understanding is needed.

Despite the advantages, the number of groups routinely using quantitative HAADF STEM as an analytical tool is currently rather small owing to the complexity of the method. Here some prominent groups and their approaches are given. The group of A. Rosenauer at the University of Bremen has done groundbreaking work in the field, particularly regarding compositional analysis of planar III-V structures [7, 4, 91]. Rosenauer's group along with V. Grillo have introduced additional materials parameters that have to be taken into account in HAADF STEM intensity quantification of some material systems: SAD, which was discussed in section 2.4.3, and surface strain

relaxation, which might decrease the image intensity at interfaces [92, 93]. V. Grillo and co-workers at the University of Modena have also recently released their own software for advanced quantitative analysis of HRTEM and HAADF STEM images [78]. J. Etheridge's group at Monash University has conducted profound studies on the effect of certain microscope parameters, such as the probe convergence angle [46] and effective source size [51], on the image quantification on aberration corrected instruments. S. Van Aert and co-workers at the University of Antwerp have on the other hand proposed an approach, where advanced statistical methods together with rather simple simulations are applied for quantifying the experimental image intensities [6]. Another group worth mentioning is S. Molina's group in Cádiz who have developed a software for simulating HAADF STEM of nanostructures [63] as well as their own method for analysing atomic resolution images via ratios of integrated column intensities [75]. This method is available as a Digital Micrograph plug-in for quantifying the composition in atomic-resolution HAADF STEM images [94].

The questions are, what are the steps further and will quantitative HAADF STEM become an established analytical tool? With the ever increasing availability of aberration corrected instruments, enabling routine acquisition of atomic resolution HAADF STEM images, the interest towards the methods for quantitative analysis of these images is clearly increasing. This is reflected for instance in the increased number of software available for such analysis [78, 94], as mentioned above. Reliable quantitative HAADF STEM analysis of different material systems will however require extensive further research, on for instance the contribution of SAD on the HAADF intensity on different systems than studied thus far (see section 2.4.3). Furthermore, quantitative HAADF STEM analysis sets some restrictions to the specimen to be studied, regarding for instance the uniformity in thickness and composition. Usually a reference area with known composition is required as well (see section 2.5.2). Quantitative HAADF STEM will hence probably remain as a special tool for specific materials problems. Nevertheless, considering the high spatial resolution and the accuracy of the method, as well as the understanding gained on the material and the instrument through the quantification procedure, there certainly exists a demand for further development and application of quantitative HAADF STEM.

Chapter 3

Heterostructured GaAs-based nanowires

Semiconductor nanowires (NWs) are potential building blocks for a wide range of applications: solar cells [16, 17, 95], LEDs [21, 96] and specific applications in biotechnology [97, 98], to mention a few. The one-dimensionality of NWs offers a number of advantages as opposed to conventional, planar semiconductor devices. Firstly, NWs can overcome the challenges and limitations caused by lattice mismatch due to strain relaxation at the free surfaces [10]. This enables NW growth on lattice-mismatched substrates, for instance GaAs on silicon [11], which makes it possible to integrate optically active semiconductors with conventional Si-based electronics [99], as well as to employ cheaper substrate materials. Furthermore, lattice-mismatched heterostructures, such as axial inserts of another semiconductor material or alloy, can be grown into the NWs, without the problem with strain which often affects the functionality of planar semiconductor heterostructures. Secondly, with NWs, a much greater surface-to-volume ratio is obtained. If a 1 cm^2 wide and 5 μm thick layer is instead made of 20 nm thick NWs with 20 nm spacing in between, the surface area becomes three times the original area while using only one-fifth of the material [100]. Hence the demand for active material is greatly reduced.

For solar cells, NWs could be a particularly advantageous design. The vertical geometry enables light absorption superior to that of planar devices [18, 100]. With optimal density, the NW array creates a light trap, and NW structures can be further tailored for optimal light absorption [101]. Moreover, in NWs the p-n junction can be created radially [17, 102, 103, 104]. In this case charge carrier creation and separation take place perpendicularly to each other – light is absorbed and carriers

are created axially along the NW, while the carriers are separated radially across the NW diameter. This reduces the recombination of electrons and holes and hence enhances the overall efficiency [18]. The possibility for strain-free growth of axial heterostructures is in turn highly beneficial for manufacturing multi-junction solar cells [95, 105, 106].

GaAs-based NWs, which is the material investigated here, offer some superior properties as opposed to for instance Si NWs. The band gap energy of GaAs (1.4 eV at room temperature [107]) is more optimal than that of Si (1.1 eV [107]) with respect to the solar spectrum. GaAs has a direct band gap, thus enabling a more efficient photon absorption. Furthermore, the band gap of III-V NWs can be tuned by alloying [17]. This can be exploited for instance in creating multi-junction solar cells, as mentioned above, to harness a broader range of the solar spectrum. The possibility for band gap engineering is advantageous for other applications as well.

A major challenge in the fabrication of heterostructured III-V NW devices is optimizing the growth to obtain the desired crystal structure and composition, and hence the desired optoelectronic properties. The growth of GaAs NWs by molecular beam epitaxy (MBE), which is the method used by the NW group at IET, NTNU, is introduced in section 3.1. Another widely applied technique in the growth of heterostructured GaAs nanowires is Metal-Organic Vapor Phase Epitaxy (MOVPE), however with MBE a higher crystal purity is obtained [108]. The crystal structure of GaAs NWs is explained in section 3.2. In optimizing the growth, characterisation by TEM plays an important role; TEM characterisation techniques employed in the present work will be covered in section 3.3. In addition to TEM, other tools commonly applied to characterising semiconductor NWs are for instance scanning electron microscopy (SEM) (morphology), Raman spectroscopy (composition) [109], scanning tunneling microscopy (morphology and electronic structure) [110], X-ray diffraction (crystal structure) [111] and photoluminescence (PL) (optical properties) [112]. In the present work, individual NWs were additionally studied with correlated PL-(S)TEM in order to understand the effect of the structural and compositional variations in the NWs in their optical properties. This technique is briefly introduced in section 3.3.4.

3.1 Growth by MBE

The GaAs NWs studied here were grown by MBE exploiting the vapor-liquid-solid (VLS) growth mechanism, first demonstrated by Wagner and Ellis in 1964 with Si NWs using Au catalyst particles [113]. In the present

work, GaAs NWs grown by both Au- and Ga-assisted techniques were studied. The Au-assisted technique is the most applied technique, and it works for most standard semiconductor materials. Au impurities might however get incorporated to the NW body during the growth, which could be detrimental for the optoelectronic properties of the NWs [89]. Furthermore, NWs grown with the Au-assisted technique tend to have a high crystal phase diversity [12] as opposed to NWs grown with the Ga-assisted technique, as will be discussed in section 3.2.

In Au-assisted growth, GaAs(111)B (As-terminated) substrates are employed [12, 114]. A thin ($\sim$ 1 nm) Au layer is first deposited on the substrate, which is thereafter taken to the MBE growth chamber and heated up under an As flux to a temperature of 540°C suitable for GaAs NW growth [12, 114]. At this stage liquid Au nanoparticles alloyed with the substrate constituents are formed. Subsequently, the GaAs NW growth is initiated by opening the shutter of the Ga effusion cell, typically set to yield a nominal planar growth rate of 0.7 monolayers per second (MLs^{-1}). The elements then dissolve to the liquid nanoparticles, which eventually become supersaturated with the gas constituents. The NW grows by precipitation from the liquid Au droplet – hence the name for the growth mechanism (VLS).

Ga-assisted growth can be realized on different substrates to obtain lower costs and/or improved device functionality. Usually Si(111) substrates are employed [115], however growth on graphene [116] and glass [117] has also been demonstrated. In Ga-assisted growth, the seed particles for the NW growth are liquid Ga droplets, which form when Ga flux is introduced to the MBE growth chamber as is illustrated in figure 3.1(a). Typical temperatures for Ga-assisted growth are $620 - 640$°C [115]. In the present study, the Ga source was typically set to yield a growth rate of 0.7 MLs^{-1}, similarly to the Au-assisted NWs [115].

In Papers I-III, GaAs NWs with axial GaAsSb inserts (figure 3.1(b)) were studied. GaAsSb inserts can be grown with both Au- and Ga-assisted techniques by introducing an Sb flux to the MBE chamber after some time (typically 15-20 min) of axial GaAs growth. The GaAsSb insert growth time can be chosen according to the desired insert length; here inserts grown for 30 s (Paper II) and 60 s (Papers I and III) were studied. After the insert growth the Sb flux is switched off and axial GaAs growth is continued. This results in a 20 to 150 nm long insert, depending on the growth rate. In some cases a flux interruption is introduced after the growth of the insert in order to reduce the Sb content in the metal droplet, to reduce defect density in the GaAs segment after the insert as well as to change the droplet contact angle (the size of the metal droplet with respect to the NW body) [115].

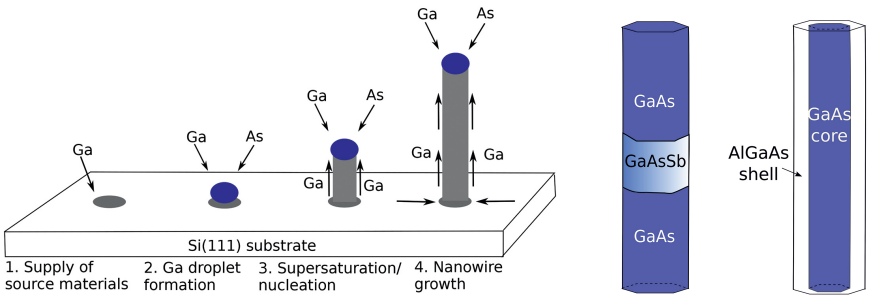

Figure 3.1: Schematic of (a) GaAs NW growth with the Ga-assisted technique, and NW heterostructures: (b) GaAs NW with an axial GaAsSb insert and (c) GaAs/AlGaAs core-shell structured NW.

Growth of full GaAsSb NWs by Au- [114] and Ga-assisted techniques [109] has also been demonstrated. Ga-assisted GaAsSb NWs were a part of the study in Paper III.

In Paper IV, GaAs/AlGaAs core-shell NWs (figure 3.1(c)) were investigated. The growth of an AlGaAs shell on the GaAs NWs is obtained differently in the two catalytic techniques. In the Au-assisted technique, an AlGaAs shell is grown by introducing an Al flux to the MBE chamber in addition to the Ga and As fluxes after the growth of a GaAs core [15]. This results in both unwanted axial VLS AlGaAs growth and radial vapor-solid (VS) growth of AlGaAs on the core facets [15]. In the Ga-assisted technique, the GaAs core growth is first terminated by stopping the Ga flux and consuming the Ga droplet by As flux. Subsequently, an AlGaAs shell is grown by VS mechanism on the core facets. In addition, a GaAs capping layer is in both Au- and Ga-assisted techniques grown on the shell facets in order to prevent oxidation of the AlGaAs shell.

3.2 Crystal structure of GaAs nanowires

In bulk, GaAs adopts the cubic zinc blende (ZB) crystal phase, however in NWs, GaAs and many other ZB III-V materials often adopt the hexagonal wurtzite (WZ) phase [118]. The two crystal phases are illustrated in figure 3.2. ZB GaAs has the space group $F\bar{4}3m$ and lattice parameter $a = 5.653$ Å [80], and WZ GaAs has the space group $P6_3mc$ and lattice parameters $a = 3.989$ Å and $c = 6.564$ Å [119]. The difference between the two phases can be understood by considering the stacking sequences

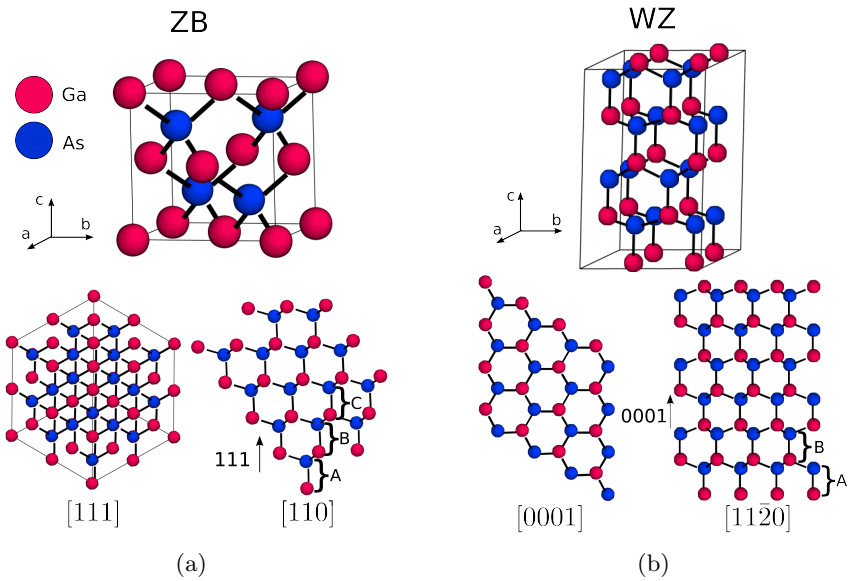

Figure 3.2: (a) The ZB GaAs unit cell, and the crystal structure viewed in [111] and [110] orientations, with the ABC stacking indicated in the latter. (b) The WZ GaAs unit cell, and the crystal structure in [0001] and [11$\bar{2}$0] orientations, with the AB stacking indicated in the latter.

in $[111]_{ZB}$ and $[0001]_{WZ}$ directions: the stacking sequence for $[111]_{ZB}$ is ABCABCABC, whereas for $[0001]_{WZ}$ it is ABABAB, as is illustrated in figure 3.2. Both ZB and WZ GaAs nanowires are hexagonal in cross-section, and the growth direction is [111] for ZB and [0001] for WZ. The NW faceting for both the phases is shown in figure 3.3(a).

In addition to the prevalence of two possible crystal phases, NWs often contain structural defects, such as stacking faults (interruption in the stacking sequence) and twins. In ZB NWs, a twin is a 60° rotation of two ZB segments about the [111] growth axis with respect to each other (shown in figure 3.5(d)), changing the stacking sequence from ABC to CBA [120]. Au-assisted GaAs NWs grown by MBE have predominantly the WZ phase, however they tend to have a high density of stacking faults, and often also the GaAs 4H polytype phase (shown in figure 3.5(d)) is observed in these NWs (see Paper II and [12]). Ga-assisted NWs adopt mostly the ZB phase, but the growth conditions can be tuned to obtain the WZ phase [115]. Ga-assisted NWs studied here usually contained few structural defects. Whether the NW adopts the WZ or the ZB phase is determined by the droplet con-

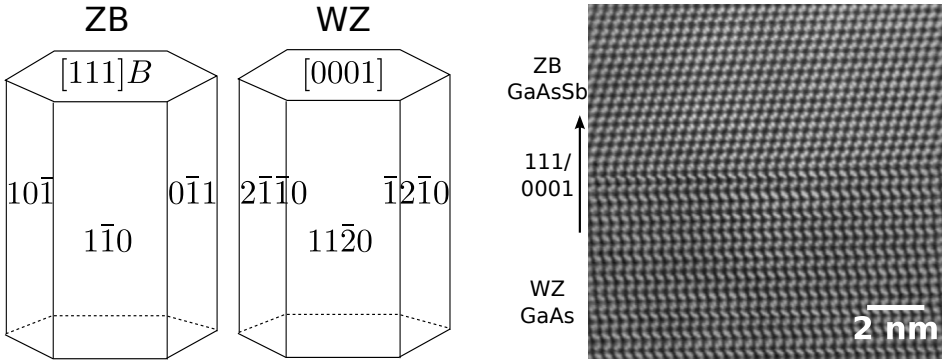

(a) (b)

Figure 3.3: (a) Schematics of the growth direction and faceting for the ZB and WZ NWs studied here and (b) a HAADF STEM image taken at the interface between the WZ GaAs part and the ZB GaAsSb insert in a Au-assisted NW. The zone axis is $\langle 11\bar{2}0 \rangle$ for WZ and $\langle 110 \rangle$ for ZB, and the growth direction for both the phases is indicated in the figure. The image was acquired with a JEOL 2200FS operated by Dr H. Jiang at the Aalto university, Finland. The image has been enhanced by Wiener filtering.

tact angle, which in turn depends in a complex manner on the growth conditions, such as the III/V flux ratio and the growth temperature [115, 118]. The crystal phase and structural defects affect the optoelectronic properties of the NWs [121], and controlling the crystal phase is hence a major focus in III-V NW growth optimization.

GaAsSb inserts within GaAs NWs, as well as GaAsSb NWs, adopt the ZB phase independent of the growth technique [12, 114, 115]. In Au-assisted NWs, The crystal phase of the pure GaAs segments above and below the GaAsSb insert is WZ [12]. A HAADF STEM image taken at the interface of the WZ GaAs segment and the ZB GaAsSb insert is shown in figure 3.3(b). In Ga-assisted NWs the pure GaAs segment below the insert has the ZB phase and above the insert usually the WZ phase [115]. In GaAs/AlGaAs core-shell structured NWs, the shell adopts the phase of the core [15]. Note that the lattice parameter of GaSb is significantly (7.8% [80]) larger than the that of GaAs, whereas the difference in lattice parameter between GaAs and AlAs is negligible (0.14% [79]).

3.3 Structural and compositional characterization by TEM

3.3.1 TEM specimen preparation

For in-plane characterisation of NWs, specimen preparation is relatively simple. The NWs are scraped off the substrate with a diamond scraper, dispersed in isopropanol and transferred to a TEM grid. In the present work graphene-coated Cu-grids (Graphene Laboratories Inc.) were used in order to minimize the effect of the support on the HAADF STEM intensity quantification. This specimen preparation technique was employed in the work for Papers I-III, where GaAs NWs with axial GaAsSb inserts, and GaAsSb NWs (Paper III) were studied. For STEM experiments, the specimens were always plasma-cleaned before loading into the TEM (twice 10 s in Fischione 2010 plasma cleaner with 20% O_2 using a shielding holder) in order to avoid build-up of carbon contamination during the STEM session.

For thorough characterisation of core-shell structured NWs, cross-sectional specimens are required. In the context of Paper IV, cross-sectioned NW specimens were prepared by ultramicrotomy. By ultramicrotomy, specimens with relatively even thickness are obtained, and problems with surface damage often present in ion milled specimens are avoided. A small piece of NWs on the substrate was embedded into epoxy resin using flat embedding moulds, and placed into a vacuum oven for hardening. The hardened samples were first abraded to obtain an approximately 500 μm wide block face, and subsequently placed in an ultramicrotome for dry trimming with a Diatome 45° diamond trimming knife. To avoid fracturing of the NW material, a small enough piece had to be employed so that there was still resin supporting the piece from several sides after the trimming. Once all the sides had been trimmed to mirror finish, the actual slices were cut with a Diatome Ultra 45° diamond knife. For a detailed description about microtomy on semiconducting materials, see [122].

In figure 3.4, HAADF STEM images of cross-sectioned Au-assisted (figures 3.4(a)-(c)) and Ga-assisted (figure 3.4(d)) GaAs/AlGaAs core-shell NWs are presented. The cross-section presented in figures 3.4(a) and 3.4(b) is presumably from the top part of a Au-assisted NW, where axial AlGaAs growth has taken place in addition to the radial shell growth (see section 3.1). The core-shell structure and the hexagonal shape are not as distinct as in the cross-section in figure 3.4(c), presumably taken from the lower part of a Au-assisted core-shell NW. In addition, in a cross-section like the one in figure 3.4(a) with a round core, by EDX similar, albeit low

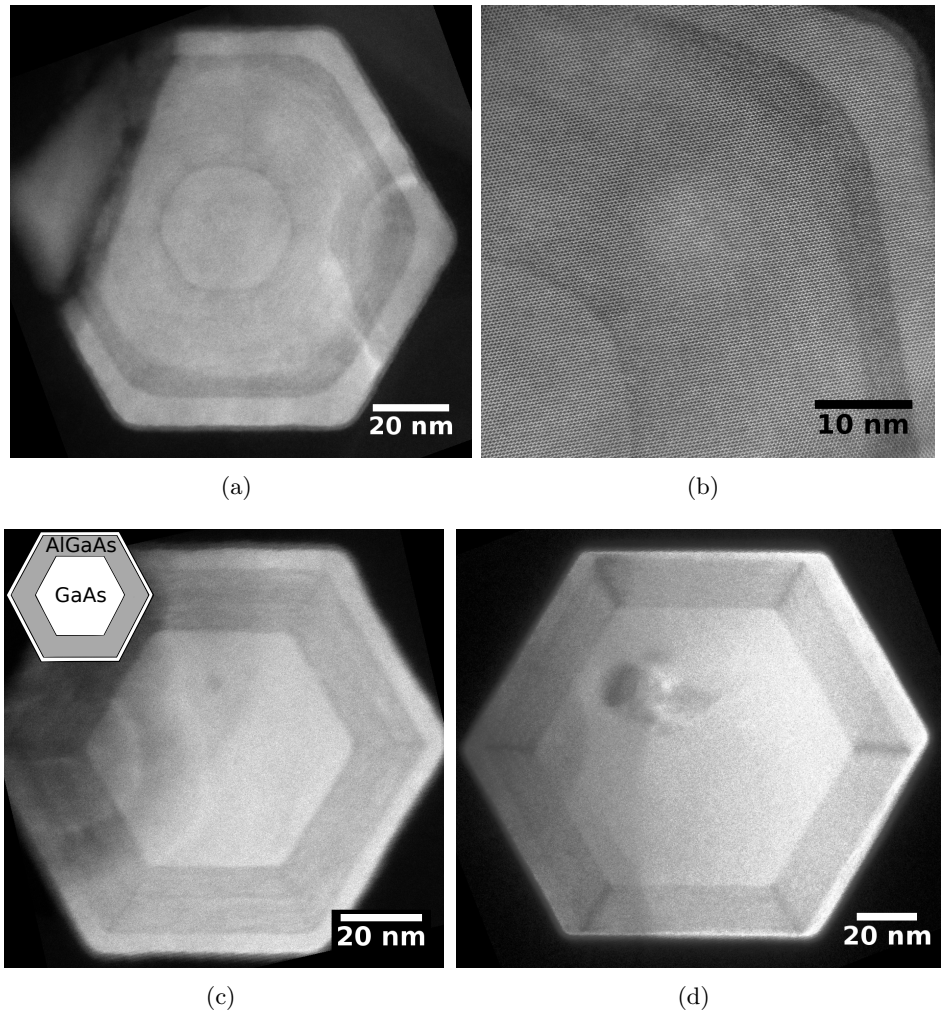

(a) (b)

(c) (d)

Figure 3.4: HAADF STEM images of cross-sectioned (a)-(c) Au- and (d) Ga-assisted GaAs/AlGaAs core-shell NWs. For Au-assisted NWs, the crystal phase is WZ and zone axis [0001]. For Ga-assisted NWs, the crystal phase is ZB and zone axis [111]. Images (a) and (b) (the same cross-section at a lower and higher magnification) were acquired with the FEI Titan^3 80-300 operated by Dr C. Zheng at MCEM, Australia. Images (c) and (d) were acquired with the JEOL 2010F at NTNU. The inset in (c) depicts the targeted cross-sectional structure, with a hexagonal GaAs core surrounded by an even and homogeneous AlGaAs shell, capped with a thin GaAs layer. The different contrast in (a) is due to this cross-section being from the axial AlGaAs part (see text), resulting in that the core is not pure GaAs but has an Al content similar to that of the shell.

(∼10%) Al concentrations were detected in both the core and the shell, which is a further proof for that these cross-sections are from the axial AlGaAs part. This further explains the similar HAADF STEM intensity in the core and the shell observed in these cross-sections (figure 3.4(a)).

In the Ga-assisted core-shell growth technique, no axial AlGaAs growth takes place (see section 3.1), and cross-sections from these NWs (figure 3.4(d)) were relatively similar, although slightly asymmetric. High-resolution HAADF STEM images of a cross-sectioned Ga-assisted GaAs/AlGaAs core-shell NW are presented in Paper IV.

3.3.2 Structural characterisation

The purpose of structural characterisation by TEM is to study the dimensions, crystal phases and structural defects in the NWs. Initial characterisation of as-grown NWs is performed with SEM (figure 3.5(a)). For characterising the crystal phase and defects, conventional TEM techniques such as BF (figure 3.5(b)) and DF TEM (see Paper II), SAED and HRTEM are used. Figure 3.5(d) shows a HRTEM image from the insert region of a Au-assisted GaAs NW with a GaAsSb insert. Above the insert (marked with black arrows), a twin as well as a short segment with 4H stacking order are present.

3.3.3 Compositional characterisation

Quantitative HAADF STEM

HAADF STEM imaging, often referred to as Z-contrast imaging, is mostly used in a qualitative manner to estimate specimen composition together with EDX [123, 124], which is described in detail below. For higher resolution and more accurate compositional characterisation, quantitative HAADF STEM is highly recommendable, as was concluded in Chapter 2.

In Papers I-III, quantitative HAADF STEM was applied to study Sb concentration and its variations in GaAsSb inserts within GaAs NWs and in GaAsSb NWs (Paper III) at a relatively low magnification. In these studies the NWs were studied in plane, in which case the thickness profile is known from the projected width assuming a hexagonal shape. This is highly beneficial for the HAADF STEM intensity quantification and enabled detailed analysis of the radial Sb distribution in GaAsSb inserts and GaAsSb NWs in Paper III. The procedure for quantitative HAADF STEM analysis of hexagonal NWs in plane is described in detail in Papers I (the basic approach) and III (quantification of the radial Sb distribution in GaAsSb

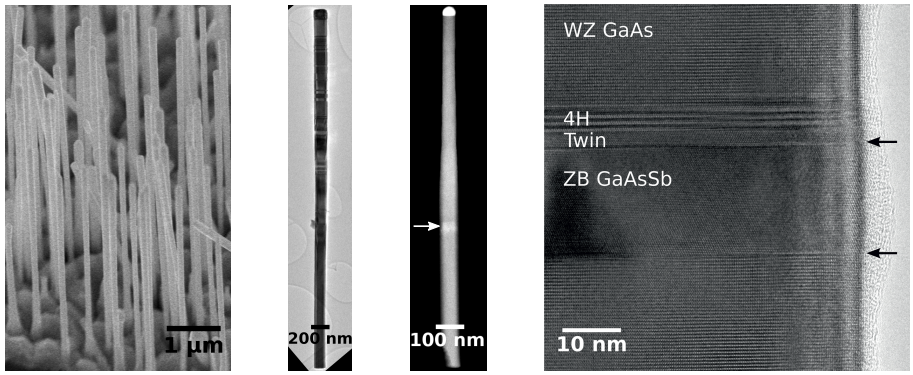

(a) (b) (c) (d)

Figure 3.5: (a) SEM image of Ga-assisted GaAs/AlGaAs core-shell NWs and (b) BF TEM image of an individual NW, with stacking faults visible in the upper part. (c) Low-magnification HAADF STEM image of a Au-assisted GaAs NW with a GaAsSb insert (indicated) and (d) HRTEM image of the insert region. The black arrows mark the insert interfaces. Image (a) was acquired with Hitachi S-5500 and images (b)-(d) were acquired with the JEOL 2010F at NTNU.

NWs and inserts).

In Paper IV, Al concentration variations in the AlGaAs shell in cross-sectioned Ga-assisted GaAs/AlGaAs core-shell NWs were studied at unit cell resolution using images taken with an aberration corrected STEM. Details for the developed method are given in the Paper IV.

Energy Dispersive X-ray Spectroscopy

One of the most common tools for compositional characterisation of heterostructured semiconductor NWs is EDX [13, 123, 124, 125]. The principle is straightforward: The high-energy electron beam excites an atom in the material, and when the atom de-excites, an X-ray with energy equal to the energy difference between the final and the excited state, characteristic to the material, is emitted. With an X-ray detector sitting above the specimen stage in TEM, the energy and number of these X-rays can be detected, and hence the elements present in the specimen can be identified and their concentrations estimated. The concentration values given by EDX however depend on a number of parameters, not just on the actual concentration [31, 126], and should hence be treated with caution as will be discussed later in this section.

The EDX software packages have automatic quantification routines and will always give a number for the concentration of an element, but the quantification can also be done manually. The most commonly applied, and the simplest quantification technique is the Cliff-Lorimer ratio technique, which applies for thin specimens, i.e., assuming no absorption or fluorescence. Assuming a material with two elements A and B and their respective concentrations C_A and C_B, the intensity of the characteristic X-ray peaks, I_A and I_B, respectively, is related to the concentrations according to [127]

$$\frac{C_A}{C_B} = k_{AB}\frac{I_A}{I_B}. \tag{3.3.1}$$

This equation is the Cliff-Lorimer equation, and k_{AB} is the Cliff-Lorimer factor, usually simply referred to as the k-factor. The k-factor is not a constant but a sensitivity factor, and will depend on a number of material and instrument parameters. In the present work usually a sample consisting of a binary material AB with known composition and a ternary material $AB_{1-y}C_y$ with unknown concentration of C, was studied. In this case k_{AB} can be determined from a spectrum at the AB segment, assuming that $C_A = C_B = 0.5$. The concentrations of B and C in the $AB_{1-y}C_y$ segment can then be determined using k_{AB} and assuming that $C_A = 0.5$. The concentration of C, C_C, is then

$$C_C = 0.5 - C_B = 0.5 - \frac{0.5}{k_{AB}}\frac{I_B}{I_A}, \tag{3.3.2}$$

where I_A and I_B are now the spectral intensities for A and B, respectively, in the $AB_{1-y}C_y$ segment. For this approach to be valid, the AB and $AB_{1-y}C_y$ segments should have the same thickness, the same crystal phase and orientation, and the illumination and detection conditions should be identical. For higher concentrations of C k_{AB} and hence equation (3.3.2) might no longer be valid. The values obtained with manual quantification were usually roughly (to within $\sim 5\%$) in agreement with the values from software quantification.

The effect of crystal orientation on the quantification is particularly problematic for GaAs alloys at or close to the $\langle 110 \rangle$ orientation. According to DeGraef [128], for (111)GaAs systematic row (i.e., strong scattering from 111 planes), which is always present at or close to the $\langle 110 \rangle$ orientation, the ratio of thickness integrated intensities of Ga and As will never be unity. Basically this means that at this orientation the X-ray emission from particular sites within a unit cell is strongly affected by electron channelling conditions. In practice it was observed that most often the column V elements dominated the signal: At GaAs regions, higher signal, and by the

software also higher concentration ($\sim 5-20\%$), was usually predicted for As than for Ga. At GaAsSb regions this might have lead to an overestimation of the Sb concentration (see the following section). Preferably an orientation where the (111) systematic row is not present should be employed; however for the NWs discussed here, this would mean looking along or close to the $\langle 111 \rangle$ growth direction. Furthermore, in the case of NWs, the hexagonal shape and the azimuthal orientation of the NW with respect to the EDX detector can also affect the concentration determination. Measuring the same GaAsSb insert of a NW from batch C in Paper III gave values for the Sb concentration varying from 13 up to 28% when orientation relative to the electron beam or to the EDX detector was altered.

In addition to the uncertainties related to the concentration determination, EDX has several other inherent drawbacks. Firstly, for the high number of counts required for a reliable quantification, a long acquisition time, or a high incident beam intensity, is needed. Consequently, the specimen might drift or get damaged, both of which can affect the quantification, and the electron dose to the specimen is high. Secondly, the spatial resolution is limited not only by the probe size, but also by beam broadening in the material: the detected X-rays do not originate only from the incident probe position, but from a cone-shaped region under this position [31]. The practical spatial resolution of the EDX on the FEG TEM used here was therefore limited to approximately 5 nm.

To summarize, EDX is an established and quick method for approximate compositional analysis, but if accuracy and high spatial resolution are needed, alternative methods such as quantitative HAADF STEM or EELS should be applied. In the present work EELS could not be applied for studying Sb concentration in $GaAs_{1-y}Sb_y$ due to the overlap between Sb $M_{4,5}$ and O K edges, however EELS quantification of this material system should be assessed in more detail.

Comparisons between quantitative HAADF STEM and EDX

In the present work, a method for studying Sb concentration in GaAsSb inserts within GaAs NWs by quantitative HAADF STEM was developed. The compositional results obtained with quantitative HAADF STEM were compared with results from EDX, which is not necessarily a reliable reference, as was discussed above. When studying Sb concentration in the $GaAs_{1-y}Sb_y$ inserts, a clear deviation was observed between the two methods such that in particular at higher Sb concentrations ($\gtrsim 16\%$), higher values were obtained with EDX. This deviation is discussed in Papers II and III. In Paper IV, where Al concentration in $Al_xGa_{1-x}As$ was studied using planar (cross-

sectioned) specimens at or close to [111] zone axis (the (111)GaAs systematic row is absent), quantitative HAADF STEM and EDX results were generally in agreement over the whole Al concentration range (see Paper IV).

An important thing to notice is that in EDX quantification, the resulting concentration values are in atomic percentages (at. %), that is, as a fraction of the total number of the constituting elements. In quantitative HAADF STEM, the Sb concentration is quantified as a fraction of group V elements. Unfortunately, this obvious yet easily forgotten fact was not realized during the writing of Paper I. Hence the EDX results in Paper I should be doubled, resulting in a disagreement with the results from quantitative HAADF STEM and in the conclusion that SAD should not be included in the STEM image simulations, which is physically unfounded (see section 2.4.3 and [69]). However, in Paper I, results from only two NWs from different batches were presented, which in retrospect is too few, considering the fluctuations in EDX quantification. In all the papers afterwards, several NWs from each studied batch were considered and the concentration results were discussed on a statistical basis, rather than relying on results from single NWs. In addition, renewed inspection of the raw EDX data from the batch 1 NW in Paper I showed that the recorded spectrum was abnormal. The Sb concentration based on the software was in this particular case significantly lower than the value based on manual quantification (22% as opposed to 34%), indicating that the data was not reliable. Moreover, it has to be pointed out that for the EDX measurements conducted for Paper I, a Si(Li) detector (Oxford Instruments, solid angle 0.1 srad) was employed. This detector was later exchanged with a Si drift detector (Oxford Instruments, solid angle 0.23 srad), which was used for all further reported EDX results.

To verify if the conclusions of Paper I are still valid, additional studies were done on the same batch 1 sample that was studied in the paper. Two of the studied NWs are presented in figure 3.6. For these NWs, maximum Sb concentrations of 17% and 9% in the insert were determined by quantitative HAADF STEM, including SAD. Excluding SAD resulted in doubling of the values. By EDX, Sb concentrations of and 13% and 11%, respectively, were obtained with manual quantification and 21% and 7% with software quantification. These values are relatively similar with the results from quantitative HAADF STEM. This supports the finding that in this Sb concentration range ($\sim 12 - 16\%$), EDX and quantitative HAADF STEM are roughly in agreement, as is discussed in Paper II for Au-assisted GaAs/GaAsSb nanowires. The conclusion made in Paper I – SAD have to be included in the compositional analysis of $GaAs_{1-y}Sb_y$ by quantitative HAADF STEM – remains the same. This is in line with data presented in

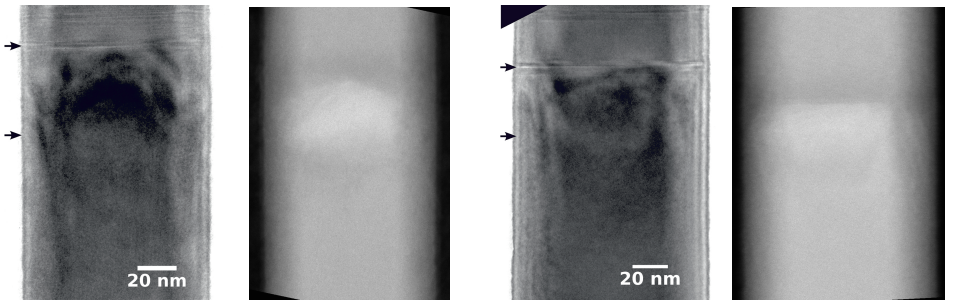

Figure 3.6: HRTEM and HAADF STEM images from the insert region for two NWs from the same batch 1 sample as studied in Paper I. The black arrows in the HRTEM images mark the insert interfaces to the GaAs segments. (a), (b) NW with a maximum Sb concentration of 17% in the insert as determined by quantitative HAADF STEM (EDX: 13%/21% by manual/software quantification). (c), (d) NW with a maximum Sb concentration of 9% in the insert (EDX: 11%/7% by manual/software quantification). The images were acquired with the JEOL 2010F at NTNU.

Papers II and III, and this is also a physically justified approach.

Later the same GaAs NWs with GaAsSb inserts as studied by TEM were additionally studied by PL [129]. This gave the possibility to determine the Sb concentration in the insert from the PL emission energy to verify the compositional analysis by quantitative HAADF STEM and EDX. Correlated PL-TEM was applied in Paper II, where Au-assisted GaAs/GaAsSb NWs were studied. An example of correlated PL-(S)TEM on a Ga-assisted GaAs/GaAsSb NW is given in the following section, together with a brief introduction to the method.

3.3.4 Correlated PL-(S)TEM

PL is applied to probe the electronic band structure and optical properties of semiconductors. The semiconductor material, in this case a NW, is illuminated with a laser beam, which results in creation of electron-hole pairs in the NW. If the electron-hole pairs recombine radiatively, that is, a photon is emitted in the process, these photons can be detected and the resulting spectrum will provide detailed information about the band structure of the specimen. Non-radiative recombination means that the electron-hole pair recombines without emitting a photon, which often occurs due to defects in the materials. In this case phonons are created instead. More details about

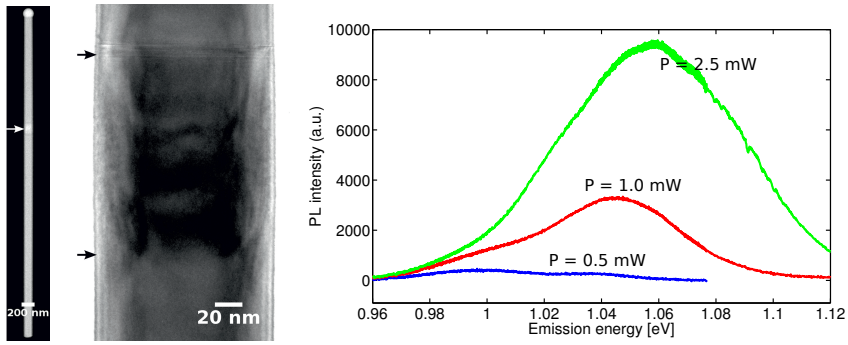

(a) (b) (c)

Figure 3.7: (a) Low-magnification HAADF STEM image of an entire GaAs NW with a GaAsSb insert (indicated with an arrow), (b) HRTEM image from the insert region (the black arrows mark the insert interfaces) and (c) the insert-related PL spectrum for different excitation powers P, acquired by L. Ahtapodov (unpublished data).

PL on semiconductors can be found elsewhere [130]. For NWs, the biggest defect is often the surface owing to the high surface-to-volume ratio, and the PL emission is greatly reduced by non-radiative recombination at the surface. This problem is particularly pronounced with GaAs NWs [131]. The main function of the AlGaAs shell is to passivate the GaAs surface states; indeed, significantly enhanced PL emission is observed from GaAs/AlGaAs core-shell NWs as opposed to bare core GaAs NWs [132, 133].

Correlated PL-(S)TEM refers to characterizing the same individual NWs by both PL and TEM. For this purpose, special TEM grids have to be employed to be able to map and identify the individual NWs in both PL and TEM. For correlated PL-TEM, SiN grids with nine windows were used [129]. These grids can however not be employed in quantitative HAADF STEM analysis as the thick SiN foil would affect the overall image intensity and thereby the quantification. To be able to characterise the NWs by quantitative HAADF STEM as well, graphene grids with a coordinate grid glued on top were later employed. Mapping was performed with SEM (usually at the 5-30 kV Hitachi S-5500 SEM/STEM) after which the chosen NWs were measured with PL. The PL measurements were carried out by L. Ahtapodov at IET, NTNU. Subsequently, the specimen was loaded into TEM for structural and compositional characterisation. After characterisation with the high-voltage TEM, the NWs do not emit any more, so the PL measurements have to be performed before the TEM characterisation [129].

Figure 3.7 presents a HAADF STEM image of an entire GaAs NW with a GaAsSb insert grown with the Ga-assisted technique (same sample as batch D in Paper III), a HRTEM image from the insert region and the insert-related PL spectrum for this particular NW. Based on the insert-related PL emission energy, using an empirical model for the low temperature band gap of unstrained bulk $GaAs_{1-y}Sb_y$ (equation (6) in [134]), an Sb concentration y of 28% was determined for the insert. With quantitative HAADF STEM, an Sb concentration of 20% was obtained, and with EDX 35%. With PL, similar spectra and accordingly similar Sb concentrations were measured for several NWs from this batch, and with quantitative HAADF STEM values around 20-22% were measured for four different NWs (only one characterised by correlated PL-(S)TEM). With EDX, values varying from 18% to 35% were determined for the same four NWs. The higher value obtained by PL as opposed to quantitative HAADF STEM is probably due to the radial Sb concentration gradients in the inserts, which was studied in detail in Paper III. Using a model that takes into account the radial concentration gradient, resulting from a combined effect of radial GaAs overgrowth and out-diffusion of Sb, a maximum Sb concentration of approximately 30% was estimated for the insert centre with quantitative HAADF STEM in Paper III. This value is roughly in agreement with the value obtained by PL.

3.4 Conclusions and outlook: semiconductor nanowires

Semiconductor NWs are undoubtedly very promising for many applications where today bulk and thin film semiconductors are used, however some technological challenges remain before large-scale integration of NWs can be realised. One major challenge already mentioned in section 3.2 is optimizing the growth to produce NWs with the desired composition and crystal phase, with high reproducibility and low defect density. Based on the present study, more uniform NWs with a lower defect density are obtained with the Ga-assisted growth technique as compared to the Au-assisted technique. Another, more fundamental limit is the high non-radiative recombination rate at the NW surface, which degrades the NW's optical performance as was explained in section 3.3.4. Furthermore, long-term stability could be a problem with NW-based semiconductor devices [99].

One of the most promising applications for semiconductor NWs is solar cells. In this field, a considerable effort has been made by a European collaboration project called AMON-RA. Under this project, an efficiency of 13.8% was recently reported with an InP NW array solar cell employing a

single axial p-i-n junction in the NWs [95]. This is comparable to the record efficiency of a planar InP solar cell. The NW group at Lund University, Sweden, which is a part of the AMON-RA project, has further developed an innovative method for cost-efficient large-scale production of NWs, termed aerotaxy, referring to synthesis of NWs in gas-phase [135]. A spin-off company Sol Voltaics produces GaAs NWs with aerotaxy to be used as a solar panel additive, promising to increase the efficiency of solar modules up to 25% [136].

With radial p-n junction core-shell structured GaAs NWs, significantly enhanced light absorption on a single standing nanowire has been reported, predicting an apparent efficiency of 40% for the single NW [102]. In this study a radial p-i-n junction NW, with a Be-doped p-type GaAs core, an intrinsic GaAs layer and a Si-doped n-type GaAs shell was employed. The NW group at NTNU is working on optimizing the design for radial p-n junction GaAs/AlGaAs solar cells with the help of simulations. The simulations predict that with optimal doping density, core and shell dimensions, NW length as well as the Al composition in the n-type $Al_xGa_{1-x}As$ shell, an efficiency of $\sim 30\%$ could be reached [137].

To conclude, the semiconductor NW technology is clearly still in its infancy, however considering the recent, fast developments, much can be expected from this field. To succeed in producing functioning NW devices, all the components – device modelling, NW growth and characterisation – will have to work together.

Part II

Papers

Paper I

Compositional characterization of GaAs/GaAsSb nanowires by quantitative HAADF-STEM

H. Kauko, T. Grieb, R. Bjørge, M. Schowalter, A. M. Munshi, H. Weman, A. Rosenauer and A. T. J. van Helvoort

Micron **44**, 254–260 (2013).

Micron 44 (2013) 254–260

Contents lists available at SciVerse ScienceDirect

Micron

journal homepage: www.elsevier.com/locate/micron

Compositional characterization of GaAs/GaAsSb nanowires by quantitative HAADF-STEM

H. Kauko[a], T. Grieb[b], R. Bjørge[a], M. Schowalter[b], A.M. Munshi[c], H. Weman[c], A. Rosenauer[b], A.T.J. van Helvoort[a,*]

[a] Department of Physics, Norwegian University of Science and Technology (NTNU), Trondheim, Norway
[b] Institut für Festkörperphysik, Universität Bremen, Bremen, Germany
[c] Department of Electronics and Telecommunications, Norwegian University of Science and Technology (NTNU), Trondheim, Norway

ARTICLE INFO

Article history:
Received 4 June 2012
Received in revised form 10 July 2012
Accepted 10 July 2012

Keywords:
HAADF-STEM
Quantitative microscopy
Nanowires
Heterostructures
GaAsSb

ABSTRACT

The Sb concentration in axial $GaAs_{1-x}Sb_x$ inserts of otherwise pure GaAs nanowires has been investigated with quantitative high-angle annular dark-field scanning transmission electron microscopy (HAADF-STEM). The Sb concentration was quantified by comparing the experimental image intensities normalized to the incident beam intensity with intensities simulated with a frozen lattice multislice approach. Including static atomic displacements in the simulations was found to be crucial for correct compositional analysis of $GaAs_{1-x}Sb_x$. HAADF intensities of individual nanowires were analysed both across the nanowires, exploiting their hexagonal cross-sectional shape, and along the evenly thick central part of the nanowires. From the cross-sectional intensity profiles, a decrease in the Sb concentration towards the nanowire outer surfaces was found. The longitudinal intensity profiles revealed a gradual build-up of Sb in the insert. The decrease of the Sb concentration towards the upper interface was either gradual or abrupt, depending on the growth routine chosen. The compositional analysis with quantitative HAADF-STEM was verified by energy dispersive X-ray spectroscopy.

1. Introduction

Semiconductor nanowires are a promising candidate for future optoelectronic applications, such as solar cells, light-emitting diodes and nanolasers (Yang et al., 2010). Nanowires enable dislocation-free growth on lattice-mismatched substrates due to strain relaxation on the free surface, and both radial and axial heterostructures can be grown into the wires. The functional properties of nanowire-based materials can be modified through size, density and composition variation of the nanostructures.

Depending on the growth conditions, pure GaAs nanowires adapt either to the wurtzite (WZ) or zinc blende (ZB) phase (Glas et al., 2007). Band gap engineering is achieved by alloying the nanowires with for instance Sb (Dheeraj et al., 2008); this might however introduce strain, defects and phase transformations, which all affect the electronic properties of the nanowires. To obtain nanowires with the desired properties, it is crucial determine the composition at a high spatial resolution and to relate the compositional variations to changes in the crystal phase. In this paper we address this task with quantitative high-angle annular dark field scanning transmission electron microscopy (HAADF-STEM).

In HAADF-STEM, most of the scattering incident on the ADF detector is thermal diffuse scattering (TDS), which is incoherent, localized at atomic columns and dependent on the atomic number, Z (Pennycook and Jesson, 1991). Quantitative HAADF-STEM refers to quantification of zone-axis image intensities by comparison with simulated intensities (LeBeau and Stemmer, 2008). This has become one of the most powerful methods for materials composition analysis with high spatial resolution. Often materials where two or more alloys are present are studied so that one of the alloys, with known composition, can be taken as a reference. Experimental intensity ratio or contrast is then compared with a simulated ratio instead of direct intensity comparison. The ratio has a low dependency on for instance thickness, which is otherwise a critical parameter in quantitative HAADF-STEM work (Grillo et al., 2008; Herrera et al., 2009; Rosenauer et al., 2009). The method has been successfully applied to composition analysis of various structures, quantum wells being the most typical object (Grillo et al., 2008; Herrera et al., 2009; Grillo, 2009; Rosenauer et al., 2011). To our knowledge the method has not been earlier applied to heterostructured nanowires.

The HAADF intensity is however sensitive to several non-compositional factors as well, especially strain. Distortions in the

* Corresponding author.
E-mail address: a.helvoort@ntnu.no (A.T.J. van Helvoort).

0968-4328/$ – see front matter © 2012 Elsevier Ltd. All rights reserved.
http://dx.doi.org/10.1016/j.micron.2012.07.002

atomic column symmetry may cause de-channelling and reduction in HAADF intensity (Perovic et al., 1993; Grillo, 2009), whereas static disorder can result in increased diffuse scattering to high angles (Perovic et al., 1993; Grillo et al., 2008; Wu and Baribeau, 2009). The scattering angle dependence of strain-related scattering is also not well understood (Yu et al., 2004; Wu and Baribeau, 2009). A prominent example of static disorder is the static atomic displacements (SAD) from the sites of the average lattice, which exist when atoms having different covalent or ionic radii are present in a crystalline alloy (Glas, 1995). This can affect the HAADF intensity, and lately the SAD have been included in simulation of atomic resolution HAADF images of III–V semiconductors (Grillo et al., 2008; Rosenauer et al., 2011). The effect of the SAD on the HAADF intensity has been studied in the case of In in GaAs by Grillo et al. (2008) and in GaN by Rosenauer et al. (2011), but not yet for the case of Sb in GaAs.

The purpose of this paper is to investigate the Sb content and distribution in ZB GaAsSb axial inserts of otherwise pure WZ/ZB GaAs nanowires, as well as to demonstrate the application of quantitative HAADF-STEM on heterostructured nanowires. As opposed to quantum wells, which can be grown with high precision and characterised with other methods due to the large surface area, nanowires are too small to be characterised with for instance standard X-ray based techniques, and often suffer from growth defects. The well-defined shape and easy TEM specimen preparation however render them an interesting material for quantitative STEM analysis. Nanowires from two different growth batches are studied. The significance of SAD in STEM simulations and intensity quantification when studying Sb concentration in $GaAs_{1-x}Sb_x$ will also be discussed. The work was performed on a non-corrected TEM/STEM at a relatively low magnification, and the results from quantitative HAADF-STEM were verified with energy dispersive X-ray spectroscopy (EDX).

2. Materials and methods

2.1. Nanowire growth

The nanowires were grown by Ga-assisted vapour–liquid–solid (VLS) growth technique on a Si(1 1 1) substrate in a Varial Gen II Modular molecular beam epitaxy (MBE) system. The growth temperature was 620 °C. Ga flux was equivalent to a nominal growth rate of 0.7 monolayers per second in thin film, As flux was 4.2×10^{-6} torr and Sb flux 1.1×10^{-6} torr. Nanowires from two different growth batches were studied, and from each batch a representative wire is presented. The growth process for batch 1 was as follows: first pure GaAs was grown for 20 min, then GaAsSb for 1 min followed by a 15 min growth interruption (all gases closed) and finally a GaAs growth for 15 min. For batch 2, four 1 min GaAsSb inserts were grown in between five 10 min GaAs segments, and no growth interruption was used. The growth direction for ZB was [1 1 1], and for WZ [0 0 0 1].

Schematic diagrams of the nanowires and the insert areas studied are shown in Fig. 1. For nanowires from batch 1, the phase before the insert is ZB, and after the insert it is either WZ or ZB GaAs. The resulting crystal phase depends on the local growth conditions, such as the wire thickness and the size of the catalyst particle, and these may vary among individual nanowires (Glas et al., 2007). For nanowires from batch 2, the pure GaAs segment before the first insert is ZB and the other pure segments between the inserts are WZ GaAs. As the pure ZB GaAs area is used as a reference in the present quantitative STEM work, only the first insert will be discussed. For nanowires from batch 1, the insert was typically followed by stacking faults, whereas nanowires from batch 2 had seldom any.

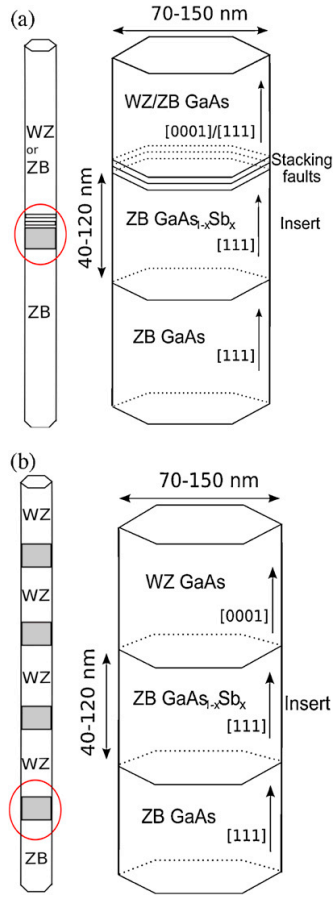

Fig. 1. Schematic diagrams of the nanowires (the gray segments are the inserts) and the studied insert areas enlarged for (a) nanowires from batch 1 (with growth interruption at the upper insert-nanowire interface) and (b) nanowires from batch 2 (four inserts).

2.2. Microscopy

2.2.1. Specimen preparation

For TEM work, the nanowires were scraped off the substrate with a diamond scraper, dispersed in isopropanol and transferred to a graphene-coated Cu-grid (Graphene Laboratories, Inc.). The samples were plasma-cleaned directly before loading into the TEM (twice 10 s in Fischione 2010 plasma cleaner with 20% O_2 using a shielding holder).

2.2.2. Imaging

The microscopy was performed on a JEOL 2010F operated at 200 kV (C_s = 1 mm). Images along the [1 1 0] axis for ZB GaAs ([1 1 $\bar{2}$ 0] for WZ) were recorded using a probe-forming aperture semi-angle of 8.4 mrad, probe size of approximately 0.2 nm and a dwell time of 38.8 μs. The ADF detector covered an angular range from 29 to 114 mrad (camera length 25 cm). The detector inner angle as well as the probe convergence angle was calibrated using Si [1 1 1] convergent beam electron diffraction patterns. The detector outer angle was determined from the detector image (see below). Reference HRTEM images were taken on a 2K Gatan UltraScan CCD camera.

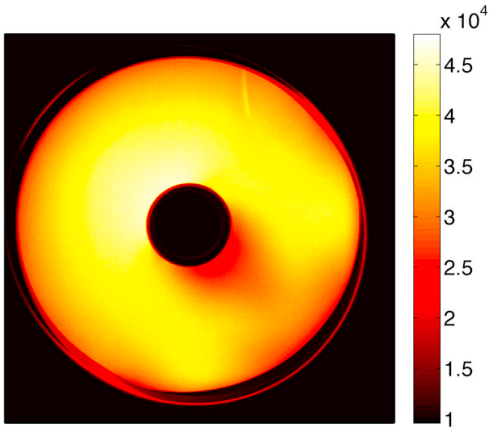

Fig. 2. Intensity map obtained by scanning the probe directly over the ADF detector.

In order to directly compare the experimental and simulated intensities, the experimental images have to be normalized relative to the incident probe intensity. This can be obtained by performing a detector scan (LeBeau and Stemmer, 2008; Rosenauer et al., 2009, 2011). At the JEOL 2010F this was accomplished by adjusting the intermediate and projector lenses in free-lens control to values corresponding to TEM-mode so that the probe was scanning directly over the detector. In addition, the objective lens defocus had to be adjusted in order to get a focused detector image. An example detector scan image is shown in Fig. 2. While scanning the detector, care was taken that the gain and offset (contrast and brightness) were such that the detector was not saturated: the intensity was set to approximately 1×10^4 in the vacuum region and 4×10^4 in the detector region (Rosenauer et al., 2009). The detector scan was always performed prior to the imaging, and the same gain and offset settings were used for image acquisition.

2.2.3. EDX

To verify the results from the quantitative STEM analysis, EDX point analyses and line scans were performed on the same nanowires directly after the HAADF-STEM work. A Si(Li) detector with INCA software (Oxford Instruments, Ltd.) was employed. Point scans were acquired both at the central area of the insert and at the pure ZB GaAs area well below the insert. The pure ZB/WZ GaAs area above the insert was also probed in order to verify that no detectable amounts of Sb was incorporated. Live time was 300 s, condenser aperture 70 μm and probe size 1 nm. The k-factor between Ga and As, k_{GA}, was determined from the K-peak intensities for Ga and As at the pure ZB GaAs region, I_{Ga} and I_{As}, as $k_{GA} = I_{As}/I_{Ga}$ (Williams and Carter, 2009). For the insert, the As and subsequently Sb concentration were determined using k_{GA} and assuming the Ga concentration to be 50 at.% (Sb takes the As sites in the lattice). To avoid the effects of channelling on the EDX signal, the nanowires were tilted slightly off the [1 1 0] zone axis before the acquisition.

EDX line scans were taken along the insert, from the pure ZB GaAs region before to the pure WZ/ZB GaAs region after the insert. Despite the long scan time (about 40 min with a total number of counts of $(1–2)\times10^6$), the counts per pixel were too low for quantitative analysis. The line scan profiles for Sb could however be compared qualitatively with the HAADF-STEM intensity profiles.

2.3. Thickness determination

Owing to the hexagonal shape of the nanowire (see Fig. 1), the cross-sectional thickness profile can be deduced from the projected width and no additional thickness determination is required. The width of each nanowire along the insert area was determined from several experimental HRTEM and HAADF lattice images, which were calibrated using the lattice spacing of ZB GaAs (5.653 Å (Vurgaftman et al., 2001)). An average width was then used when calculating the final nanowire thickness. The variation in the width of a nanowire as determined from the different images was typically less than 2 nm.

2.4. Simulations

Simulations were performed with the STEMsim software (Rosenauer and Schowalter, 2008), based on the frozen-lattice multislice method. For each Sb concentration $x \in \{0, 0.1, 0.2, 0.3\}$ in ZB $GaAs_{1-x}Sb_x$, 15 supercells with different statistical distributions of Sb and As atoms, different thermal displacements, as well as different SAD were generated. The SAD were implemented by relaxation using the valence force field method, and the relaxations were done using Keating potentials (Schowalter et al., 2012). The final simulated HAADF image was taken as an average over the individual images with different configurations. A supercell of 7×7 unit cells in [1 1 0] orientation was employed, with 80/108 pixels per unit cell in [0 0 1]/[1 $\bar{1}$ 0] direction. The total thickness of the simulated stack was 160 nm. The lattice constant a_{GaAsSb} for each simulated composition of the ternary semiconductor was calculated as a linear combination of the lattice constants of the pure structures, a_{GaAs} and a_{GaSb} (5.653 Å and 6.096 Å, respectively; Vurgaftman et al., 2001), according to Vegard's law:

$$a_{GaAsSb} = (1 - x)a_{GaAs} + xa_{GaSb}. \quad (1)$$

The Debye–Waller temperature factors for calculating the thermal displacements were based on DFT calculations (Schowalter et al., 2009). The respective values for the Debye–Waller factors, B, were $B_{As} = 0.600\ Å^2$ and $B_{Ga} = 0.697\ Å^2$ for GaAs, and $B_{Sb} = 0.819\ Å^2$ and $B_{Ga} = 0.953\ Å^2$ for GaSb. The Debye–Waller factor of Ga in the ternary semiconductor was calculated by linear interpolation similarly to Eq. (1).

Using the average intensities from images simulated for different thicknesses and concentrations, a matrix for the simulated $GaAs_{1-x}Sb_x$ intensity as a function of thickness and Sb concentration, x, was constructed by cubic interpolation. This so-called CT-matrix, shown in Fig. 3, was then used for analysing the normalized experimental images.

2.5. Intensity analysis

In order to compare experimental and simulated image intensities, the experimental images were normalized using the detector scan according to (Rosenauer et al., 2009):

$$I_{norm} = \frac{I_{raw} - I_{vac}}{I_{det} - I_{vac}} \quad (2)$$

where I_{raw} is the raw image intensity, I_{vac} is the mean vacuum intensity and I_{det} is the mean intensity on the detector. To determine I_{vac} and I_{det}, the detector image was segmented using two different threshold values: one to select the detector area only, and one to select the vacuum area. This was necessary due to the artefacts (outer rims) occurring in the detector image (see Fig. 2).

For the pure ZB GaAs parts, the normalized experimental intensities were compared directly with simulated intensities using intensity profiles taken across the nanowires. For the GaAsSb inserts, both cross-sectional intensity profiles as well as profiles

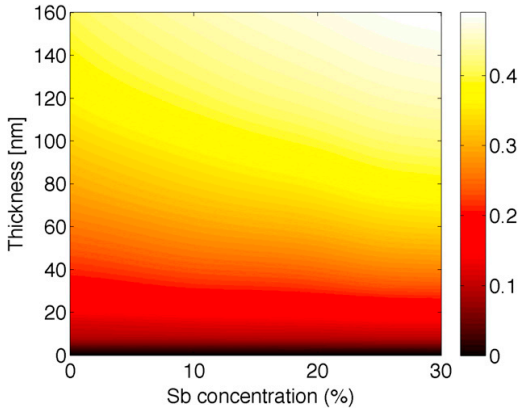

Fig. 3. Simulated average image intensity for $GaAs_{1-x}Sb_x$ as a function of thickness and Sb concentration.

taken along the evenly thick central part of the nanowires were studied. The analysis for the inserts were performed via the intensity ratio, I/I_{GaAs}, where I_{GaAs} is the pure ZB GaAs intensity at the maximum nanowire thickness. For calculating the experimental intensity ratio, image intensities normalized according to Eq. (2) were used.

3. Results

3.1. HRTEM and HAADF-STEM images

Fig. 4(a) depicts first a HRTEM image of the insert area of a nanowire from batch 1 ("nanowire 1"), and Fig. 4(b) depicts a HAADF-STEM image from the same region. Indicated in the HRTEM image are the pure ZB GaAs area, stacking faults below the insert and the insert. The thickness of the nanowire was 70 ± 2 nm. The insert length, determined from the HRTEM image as the length of the defect-free insert area, was 68 ± 3 nm.

Fig. 4(c) and (d) shows similarly HRTEM and HAADF images of the insert area of a nanowire from batch 2 ("nanowire 2"). The region below the insert is ZB GaAs and above the insert WZ GaAs, as indicated in the HRTEM image. As opposed to nanowire 1, this nanowire is completely defect-free in the pure GaAs regions below and above the insert. The thickness of this nanowire was 112 ± 2 nm, and the insert length was 121 ± 3 nm.

3.2. HAADF intensity quantification and composition analysis

3.2.1. Cross-sectional intensity profiles

Cross-sectional experimental HAADF intensity profiles are compared with simulated profiles in Fig. 5. The experimental profiles were obtained by averaging over narrow (ca. 5 nm wide) areas across the HAADF images of the nanowires, in a defect-free pure ZB GaAs region below the insert (Fig. 5(a) and (c)), and in the middle of the the $GaAs_{1-x}Sb_x$ insert (Fig. 5(b) and (d)). The simulated profiles were constructed using the CT-matrix (see Fig. 3) and a thickness profile calculated from the basis of the known geometry and thickness. To find the simulated intensity – and hence the Sb concentration – matching the experimental intensity at the insert, the average intensity for the central part of the experimental profile was used. The Sb concentrations obtained from this comparison were $17 \pm 3\%$ for nanowire 1 and $13 \pm 2\%$ for nanowire 2. The width of the averaging area for concentration determination was 70% of the width of the evenly thick central part, and the error estimates are based on the variation in intensity in this region. The Sb concentration results from EDX point analysis were 17% and 12% for nanowires 1 and 2, respectively.

3.2.2. Intensity profiles along the nanowires

The HAADF intensities were further analysed along the central parts of the nanowires, where the thickness is constant. Longitudinal intensity profiles were obtained by averaging over a rectangle covering 70% of the width of the evenly thick central part. The intensity profiles were then converted into Sb concentration profiles using the known thickness and the CT-matrix. Fig. 6(a) and (b) shows the resulting profiles for nanowires 1 and 2, respectively. The interfaces delimiting the insert are marked with vertical dashed lines. The maximum Sb concentrations obtained from these graphs lies at 17% for nanowire 1 and 13% for nanowire 2, in accordance with the results from the cross-sectional intensity analysis. Fig. 6(c) and (d) displays the EDX line profiles for Sb, also taken over the insert regions along the central parts of the nanowires.

4. Discussion

4.1. HAADF intensity quantification and composition analysis

4.1.1. Cross-sectional intensity profiles

The cross-sectional intensity profiles for pure ZB GaAs served as a good verification for the quantification approach. For nanowire 1 (Fig. 5(a)) the match between experimental and simulated profiles is almost perfect throughout the whole thickness profile. For nanowire 2 (Fig. 5(c)) the match is also good, apart from leaps in experimental intensity at the corners of the central part. The origin of these leaps is the longitudinal bright bands seen along the nanowire corners in the HAADF image (Fig. 4(d)). In the corresponding HRTEM image (Fig. 4(c)), dark bands are visible. This effect might be related to nanowire thickness as it is only observed with thicker nanowires. Similar longitudinal intensity variations have been observed earlier in core–shell nanowires, and these were ascribed to an increased curvature of atomic columns at the corners (Grillo and Rossi, 2011). Generally, the correspondence between experimental and simulated cross-sectional profiles for pure ZB GaAs was very good for nearly all the studied wires. Hence we conclude that for the part without Sb, the approach and the model work.

The cross-sectional profiles at the insert (Fig. 5(b) and (d)) do not display an equally good match for the whole thickness range. At the central parts of these profiles, the experimental intensity is varying, and appears to have a maximum in the middle. These variations cause the relatively high error values for the determined Sb concentration (see Section 3.2.1). Furthermore, at the nanowire wedges the experimental intensity is clearly lower than the simulated intensity for both the wires shown here. This effect was observed with all the studied wires, and it might indicate a decrease in Sb concentration towards the nanowire surfaces, or a deviation from the hexagonal shape at the insert region. For the latter no indications in these nanowires have been found.

To study further the possibility of a radially varying Sb concentration, another simulated profile was constructed using a simple model where the Sb concentration increases linearly from zero at the edge to a maximum value at the centre of the nanowire (red dashed line in Fig. 5(b) and (d)). These profiles display a significantly better match with the experimental profiles for both the wires. The maximum values for Sb concentration were $20 \pm 1\%$ for nanowire 1 and $15 \pm 1\%$ for nanowire 2, based on intensities from a narrow region at the centre (10% of the width of the evenly thick central part). The lower Sb content radially outwards might result from radial GaAs overgrowth during the axial nanowire growth after the insert. It could explain the relatively high photo-luminescence

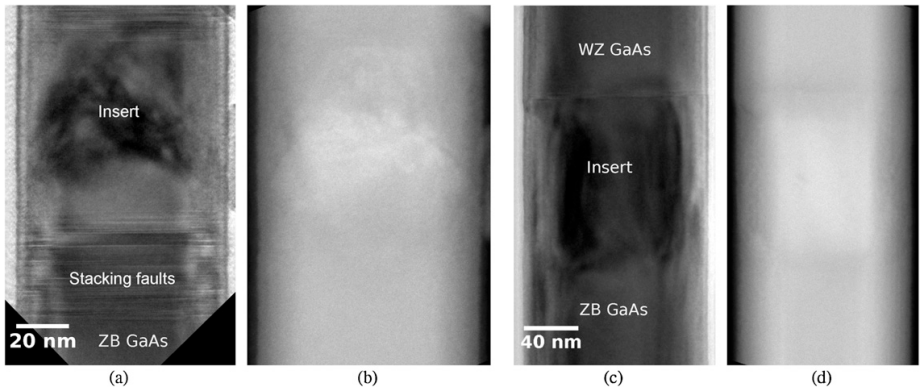

Fig. 4. HRTEM and HAADF-STEM images over the insert area for (a) and (b) nanowire 1 and (c) and (d) nanowire 2.

emission from $GaAs_{1-x}Sb_x$ inserts observed with similar nanowires despite the absence of a passivating shell (Dheeraj et al., 2008). We however expect the lateral overgrowth to be only a few nanometers.

4.1.2. Intensity profiles along the nanowires

The intensity profiles along the nanowires revealed how the Sb concentration varies along the insert. From MBE one would expect a Sb concentration profile close to rectangular, giving a well-defined sharp change in the band-gap structure. As seen from Fig. 6, this was not the case with the nanowires presented here, nor with other studied nanowires from these batches. This is probably due to the VLS growth mechanism. For growth with a stable Sb concentration an equilibrium between Sb dissolving into the catalytic Ga droplet and precipitating into the insert from the droplet has to be established first. With these wires, the Sb profile increases gradually over a distance of 20 nm (nanowire 1) to 30 nm (nanowire 2) before reaching a plateau. For nanowire 2, the increase/decrease in Sb concentration is equally gradual at the lower and the higher interface, resulting in a symmetric profile. For nanowire 1, the drop in Sb concentration is more abrupt due to the growth routine employed (growth interruption). Furthermore, in the case of nanowire 1 the

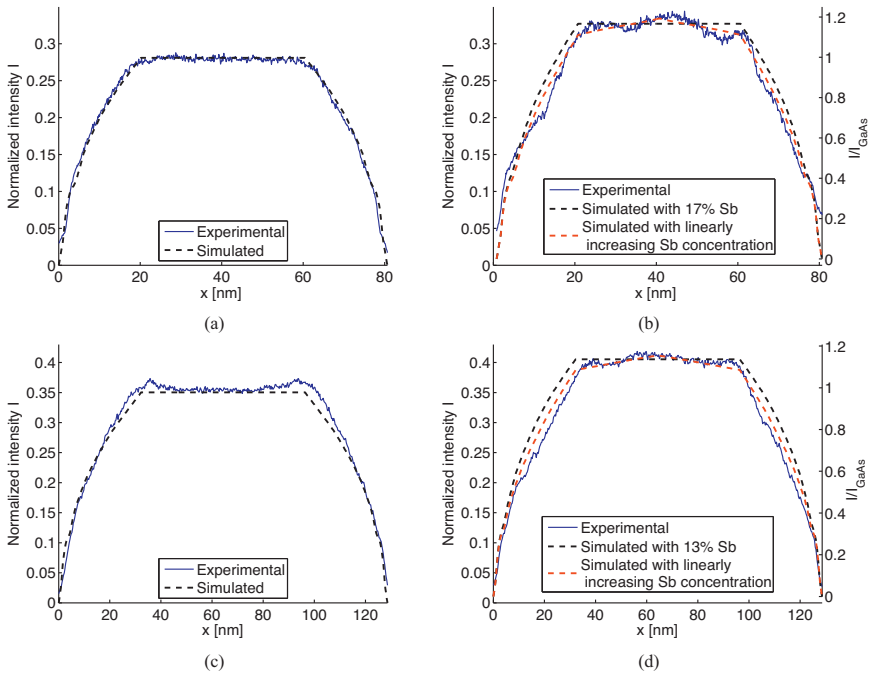

Fig. 5. Experimental intensity profiles across the HAADF images together with simulated profiles for the pure GaAs region below the insert (left) and for the central, highest intensity part of the insert (right): (a) and (b) nanowire 1; (c) and (d) nanowire 2. The simulated profiles plotted with black dashed line correspond to uniform Sb concentration across the nanowire. The profiles plotted with red dashed line were constructed with a model where Sb concentration increases linearly in the radial direction from zero at the edge to a maximum value at the centre of the nanowire.

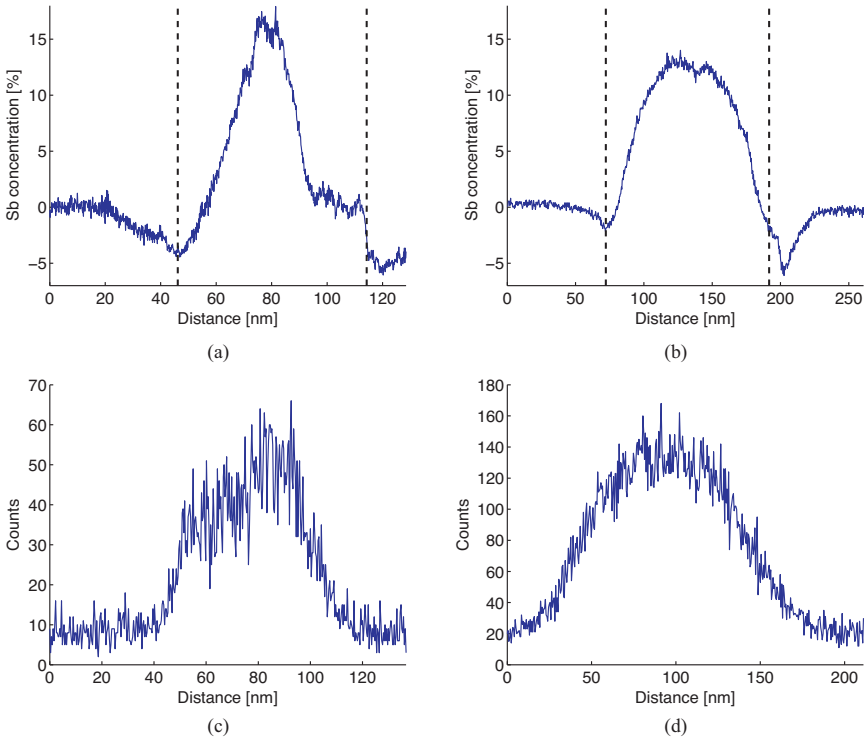

Fig. 6. The plots on the left are for nanowire 1, and on the right for nanowire 2. (a) and (b) Sb concentration profiles, obtained from HAADF intensity profiles taken along the central parts of the nanowires. The vertical lines denote the insert interfaces. The negative Sb concentration values at the interfaces are not real compositional effects but due to the intensity dips at the interfaces caused by surface strain relaxation and lattice defects. (c) and (d) EDX line scans for Sb taken overt the insert region along the central parts of the nanowires.

concentration drops to a stable, very low level before the structural interface, as judged from the HAADF-STEM intensity. This finding is relevant to possible electronic transitions within the insert (Hoang et al., 2010). We interpret this region with a very low Sb level as dissolving of the insert during the growth interruption.

At the interfaces, clear intensity dips are observed with both the nanowires. This is probably due to surface strain relaxation: bending of atomic columns near the surface at the interfaces causes de-channelling of the electron probe and thereby a drop in the HAADF intensity (Grillo, 2009). The effect was observed with all the studied nanowires, and has earlier been observed with quantum well and quantum dot structures (Grillo, 2009; Grillo and Rossi, 2011; Grieb et al., 2012). For nanowire 2 the dip is more pronounced at the upper interface, between the ZB insert and WZ GaAs, although a clear drop is observed at the lower interface as well, where there is no change in the phase. Note that after the dip the intensity at the pure WZ GaAs is even and nearly at the same level as the ZB GaAs intensity. Nanowire 1 has a longer low-intensity region before the insert, between the pure GaAs region and the insert, due to the presence of stacking faults. After the insert the intensity does not return to the pure ZB GaAs level, again because of an extended region with stacking faults.

Apart from the intensity dips at the interfaces and at the stacking faults, the HAADF-STEM intensity profiles are very similar with the EDX line scan profiles (Fig. 6(c) and (d)). Even the intensity variations at the peak plateau for the case of nanowire 1 are re-produced in the EDX profile, although with significantly lower spatial resolution and more noise.

4.2. Effect of strain on intensity quantification

In the HAADF images and in the intensity profiles extracted from them, prominent intensity variations were observed at the insert areas and at the interfaces. Intensity variations are present in the corresponding areas in the HRTEM images as well (Fig. 4(a) and (c)), and they appear to be strain related. This could have affected the concentration analysis. Strain-induced contrast in HAADF images can be related to two different mechanisms (Grillo, 2009): The first is often referred to as Huang scattering, which means diffuse scattering produced by lattice imperfections, such as the SAD (Wang, 1995). The second is related to de-channelling. De-channelling refers to reduction in the excitation of the 1s Bloch states, and thereby reduced scattering on to the HAADF detector due to distortions in atomic column symmetry (Perovic et al., 1993). An example of this are the intensity dips at the insert interfaces (see Section 4.1.2 and Fig. 6(a) and (b)). The decrease in intensity observed in connection with stacking faults with nanowire 1 might also be caused by de-channelling. These regions had to be ignored in the intensity quantification.

The intensity variations within the inserts can probably be ascribed to Huang-type scattering, resulting from lattice imperfections caused by Sb being introduced into the lattice. At the central part of the insert of nanowire 2 the intensity is rather uniform, indicating a homogeneous distribution of Sb atoms. The strong intensity variations observed at the insert of nanowire 1, also reflected in the higher error for the Sb concentration as determined in Section 3.2.1, might be a result of clustering of Sb. The good

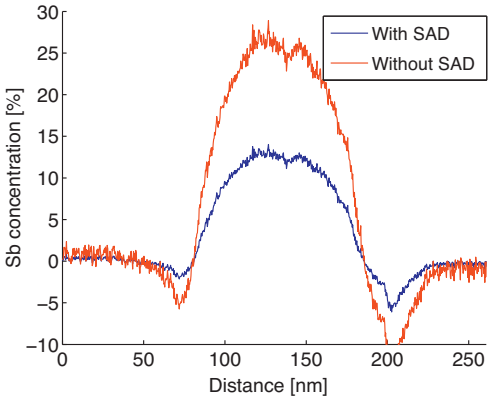

Fig. 7. The Sb concentration profile for nanowire 2 from Fig. 6(b) together with a profile constructed without taking the SAD into account.

correspondence between the results from quantitative HAADF and EDX point analyses however indicate that the applied method – with SAD included in the simulations – was sufficient and that this type of intensity variations have not remarkably affected the composition analysis within the insert.

To visualize the effect of SAD in the composition analysis, the Sb concentration profile for nanowire 2 from Fig. 6(b) is re-plotted in Fig. 7 together with a profile generated using simulations where the SAD was not taken into account. Only when SAD was taken into account, Sb concentrations similar to those determined by EDX point analysis were obtained. Hence it is evident that the simulations without SAD yield significantly lower HAADF intensities for the ternary semiconductor – and result in a clear overestimation of the Sb concentration.

5. Conclusions

In this study we have applied quantitative HAADF-STEM for studying the Sb concentration in GaAs nanowires with axial $GaAs_{1-x}Sb_x$ inserts, using nanowires from two different growth batches. The work involved comparison of simulated intensities with experimental intensities normalized with respect to the incident beam intensity. In the simulations, the SAD were included, and this was found to be crucial for compositional analysis of $GaAs_{1-x}Sb_x$. Simulated intensity profiles were in good agreement with normalized experimental intensity profiles taken across the nanowire HAADF images at the pure GaAs region. At the $GaAs_{1-x}Sb_x$ inserts, the experimental cross-sectional profiles deviated from simulated profiles with a radially uniform Sb concentration. A better agreement was obtained with a simulated profile with Sb concentration increasing linearly towards the nanowire centre, indicating a decrease in Sb the concentration towards the nanowire outer surfaces. Intensity profiles taken along the evenly thick central part of the nanowires revealed that the Sb concentration builds up gradually within the insert, and decreases after a plateau either gradually or more abruptly, depending on the growth conditions chosen. At the plateaus, Sb concentrations of 17% and 13% were obtained for the two nanowires, and these results were in good agreement with results from EDX point analysis (17% and 12%, respectively). Hence this study demonstrates that quantitative HAADF-STEM can be applied for compositional analysis of heterostructured GaAs/GaAsSb nanowires, providing relevant high-resolution insight into the radial and axial distribution of Sb within the nanowires.

Acknowledgments

This work was supported by the Faculty of Natural Sciences and Technology at NTNU and by the DFG (German research foundation) under contract no. RO2057/8-1-3008074.

References

Dheeraj, D.L., Patriarche, G., Zhou, H., Hoang, T.B., Moses, A.F., Grønsberg, S., van Helvoort, A.T.J., Fimland, B.-O., Weman, H., 2008. Growth and characterization of wurtzite GaAs nanowires with defect-free zinc blende GaAsSb inserts. Nano Letters 8 (12), 4459–4463.

Glas, F., 1995. Correlated static atomic displacements and transmission-electron-microscopy contrast in compositionally homogeneous disordered alloys. Physical Review B 51 (2), 825–839.

Glas, F., Harmand, J.-C., Patriarche, G., 2007. Why does wurtzite form in nanowires of III–V zinc blende semiconductors? Physical Review Letters 99 (14), 146101.

Grieb, T., Müller, K., Fritz, R., Schowalter, M., Neugebohrn, N., Knaub, N., Volz, K., Rosenauer, A., 2012. Determination of the chemical composition of GaNAs using STEM HAADF imaging and STEM strain state analysis. Ultramicroscopy 117 (6), 15–23.

Grillo, V., 2009. The effect of surface strain relaxation on HAADF imaging. Ultramicroscopy 109 (12), 1453–1464.

Grillo, V., Carlino, E., Glas, F., 2008. Influence of the static atomic displacement on atomic resolution *Z*-contrast imaging. Physical Review B 77 (5), 054103.

Grillo, V., Rossi, F., 2011. A new insight on crystalline strain and defect features by STEM-ADF imaging. Journal of Crystal Growth 318 (1), 1151–1156.

Herrera, M., Ramasse, Q.M., Morgan, D.G., Gonzalez, D., Pizarro, J., Yáñez, A., Galindo, P., Garcia, R., Du, M.-H., Zhang, S.B., Hopkinson, M., Browning, N.D., 2009. Atomic scale high-angle annular dark field STEM analysis of the N configuration in dilute nitrides of GaAs. Physical Review B 80 (12), 125211.

Hoang, T.B., Moses, A.F., Ahtapodov, L.Z.H., Dheeraj, D.L., van Helvoort, A.T.J., Fimland, B.-O., Weman, H., 2010. Engineering parallel and perpendicular polarized photoluminescence from a single semiconductor nanowire by crystal phase control. Nano Letters 10 (8), 2927–2933.

LeBeau, J.M., Stemmer, S., 2008. Experimental quantification of annular dark-field images in scanning transmission electron microscopy. Ultramicroscopy 108 (12), 1653–1658.

Pennycook, S.J., Jesson, D.E., 1991. High-resolution *Z*-contrast imaging of crystals. Ultramicroscopy 37 (1-4), 14–38.

Perovic, D.D., Rossouw, C., Howie, A., 1993. Imaging elastic strains in high-angle annular dark field scanning transmission electron microscopy. Ultramicroscopy 52 (3–4), 353–359.

Rosenauer, A., Gries, K., Müller, K., Pretorius, A., Schowalter, M., Avramescu, A., Engl, K., Lutgen, S., 2009. Measurement of specimen thickness and composition in $Al_xGa_{1-x}N$/GaN using high-angle annular dark field images. Ultramicroscopy 109 (9), 1171–1182.

Rosenauer, A., Mehrtens, T., Müller, K., Gries, K., Schowalter, M., Satyam, P.V., Bley, S., Tessarek, C., Hommel, D., Sebald, K., Seyfried, M., Gutowski, J., Avramescu, A., Engl, K., Lutgen, S., 2011. Composition mapping in InGaN by scanning transmission electron microscopy. Ultramicroscopy 111 (8), 1316–1327.

Rosenauer, A., Schowalter, M., 2008. STEMSIM - a new software tool for simulation of STEM HAADF *Z*-contrast imaging. In: Microscopy of Semiconducting Materials 2007. Vol. 120 of Springer Proceedings in Physics, pp. 170–172.

Schowalter, M., Müller, K., Rosenauer, A., 2012. Scattering amplitudes and static atomic correction factors for the composition-sensitive 002 reflection in sphalerite ternary III–V and II–VI semiconductors. Acta Crystallographica Section A: Foundations 68 (1), 68–76.

Schowalter, M., Rosenauer, A., Titantah, J.T., Lamoen, D., 2009. Jan. Temperature-dependent DebyeWaller factors for semiconductors with the wurtzite-type structure. Acta Crystallographica Section A: Foundations 65 (1), 5–17.

Vurgaftman, I., Meyer, J.R., Ram-Mohan, L.R., 2001. Band parameters for III–V compound semiconductors and their alloys. Journal of Applied Physics 89 (11), 5815–5875.

Wang, Z.L., 1995. Elastic and Inelastic Scattering in Electron Diffraction and Imaging. Plenum Press, New York.

Williams, D.B., Carter, C.B., 2009. Transmission Electron Microscopy: A Textbook for Materials Science. Part 4: Spectrometry, 2nd ed. Springer.

Wu, X., Baribeau, J.-M., 2009. Composition and strain contrast of $Si_{1-x}Ge_x$ ($x = 0.20$) and $Si_{1-y}C_y$ ($Y \leq 0.015$) epitaxial strained films on (1 0 0) Si in annular dark field images. Journal of Applied Physics 105 (4), 043517.

Yang, P., Yan, R., Fardy, M., 2010. Semiconductor nanowire: what's next? Nano Letters 10 (5), 1529–1536.

Yu, Z.H., Muller, D.A., Silcox, J., 2004. Study of strain fields at a-Si/c-Si interface. Journal of Applied Physics 95 (7), 3362–3371.

Paper II

The effects of Sb concentration variation on the optical properties of GaAsSb/GaAs heterostructured nanowires

J. Todorovic, H. Kauko, L. Ahtapodov, A. F. Moses, P. Olk,
D. L. Dheeraj, B. O. Fimland, H. Weman and A. T. J. van Helvoort

Semiconductor Science and Technology **28**, 115004 (2013).

Semicond. Sci. Technol. **28** (2013) 115004 (13pp) doi:10.1088/0268-1242/28/11/115004

The effects of Sb concentration variation on the optical properties of GaAsSb/GaAs heterostructured nanowires

J Todorovic[1], H Kauko[1], L Ahtapodov[2], A F Moses[2], P Olk[2], D L Dheeraj[2], B O Fimland[2], H Weman[2] and A T J van Helvoort[1,3]

[1] Department of Physics, Norwegian University of Science and Technology, NO-7491, Trondheim, Norway
[2] Department of Electronics and Telecommunications, Norwegian University of Science and Technology, NO-7491, Trondheim, Norway

E-mail: a.helvoort@ntnu.no

Received 3 June 2013, in final form 15 August 2013
Published 27 September 2013
Online at stacks.iop.org/SST/28/115004

Abstract

In this work we have investigated the variation of Sb concentration among and within zinc blende (ZB) GaAsSb inserts in wurtzite (WZ) GaAs bare-core and WZ GaAs/AlGaAs core–shell nanowires (NWs) grown by Au-assisted molecular beam epitaxy. The Sb concentration variation was related to the optical properties as determined by photoluminescence (PL). The NW structure and the Sb concentration were studied by transmission electron microscopy (TEM), energy dispersive x-ray spectroscopy (EDX) and quantitative high angle annular dark field scanning TEM (HAADF STEM). A clear trend relating the maximum Sb concentration with the insert length was observed: the longer the insert, the higher the Sb concentration. In addition, there are graded Sb concentration gradients both along and across the GaAsSb inserts. The influence of the Sb concentration variation on the PL emission from the GaAsSb inserts was investigated with correlated micro-PL and TEM-EDX on the same single NWs. Based on the PL results and the observed Sb concentration profiles, we propose a qualitative energy band diagram for a typical ZB GaAsSb insert in a WZ GaAs NW for the heterostructured NWs studied here. Type I transitions within the central region of the ZB GaAsSb inserts were found to dominate the insert-related PL emission. Weak type II transitions within the inserts due to the graded Sb concentration were observed as well. Using an existing empirical model, the Sb concentrations were additionally determined from the ground state PL energies (type I transition). For the average Sb concentration, the concentrations based on PL were in agreement with EDX and quantitative HAADF STEM results.

(Some figures may appear in colour only in the online journal)

1. Introduction

Axial inserts and quantum dots in heterostructured semiconductor nanowires (NWs) have become an attractive topic of research within the last decade and promise to be useful in a wide range of applications such as transistors [1], photodetectors [2] and single-photon sources [3]. Growth optimization of the axial inserts in terms of controlling their size, composition, crystal phase and structural defect density, is of utmost importance for realizing the application potential of such axially heterostructured NWs.

One of the interesting III–V ternary systems is $GaAs_{1-x}Sb_x$ due to the widely tunable bandgap and the possibility for both type I and II band alignment with GaAs [4–8]. The composition and the optical properties of strained GaAs/GaAsSb quantum wells [5, 9, 10] and

[3] Author to whom any correspondence should be addressed.

pseudomorphic GaAsSb thin films grown on GaAs [6, 8] have been a topic of study for some decades. In contrast to these two-dimensional heterostructures, the $GaAs_{1-x}Sb_x$ system in heterostructured semiconductor NWs is a relatively new field of technological interest. The growth of zinc blende (ZB) GaAsSb (axial) inserts in wurtzite (WZ) GaAs NWs by Au-assisted molecular beam epitaxy (MBE) was demonstrated in 2008 by Dheeraj *et al* [11]. Subsequently, there have been reports on ZB GaAsSb inserts in GaAs NWs, focusing on the growth optimization, optical characterization by micro-photoluminescence (μ-PL) and structural characterization by transmission electron microscopy (TEM) [11–17].

The composition in semiconductor NWs is most commonly studied by energy dispersive x-ray spectroscopy (EDX) in TEM [13, 15]. One of the few alternatives for high-resolution composition analysis is quantitative high angle annular dark field scanning TEM (HAADF STEM) [18]. This technique has been successfully applied to different planar semiconductor heterostructures, but hardly to heterostructured NWs [19]. Composition variation within the NW's axial inserts and the insert-core and core–shell interface sharpness will affect the optical properties of these inserts. While the effects of the structural defects on the NW optical properties have been reported in a number of studies [20–22], the effects of possible composition variation within a NW heterostructure on the optical properties has not been studied in detail yet. To achieve precise tailoring of the bandgap, it is crucial to correlate the exact Sb content in the GaAsSb insert with the insert PL emission energy and to determine whether the optical transitions related to the insert are of type I or type II.

In this work, we report on the Sb concentration variation among and within ZB GaAsSb inserts in WZ GaAs bare-core and WZ GaAs/AlGaAs core–shell NWs grown by Au-assisted MBE, and study how the compositional variations affect the optical properties of the insert. The Sb concentration and its variation within the inserts were studied with EDX and quantitative HAADF STEM. Independently, a large number of single bare-core and core–shell NWs were studied with correlated μ-PL-(S)TEM-EDX. For these NWs, the Sb concentrations were additionally determined from the ground state energies of the ZB GaAsSb PL emission using an existing empirical model. The Sb concentrations obtained with these three different analytical methods are compared. Furthermore, the effects of the Sb concentration variation within the insert on the GaAsSb-related PL emission are discussed. Based on the PL results and the Sb concentration analyses, we propose a qualitative energy band diagram for a typical ZB GaAsSb insert in a WZ GaAs NW for the heterostructured NWs studied here.

2. Methods

2.1. NW growth

The NWs were grown by Au-assisted MBE on GaAs(111)B substrates in a Varian Gen II Modular system. Two different batches with ZB GaAsSb inserts were studied in this work: WZ GaAs bare-core and WZ GaAs/AlGaAs core–shell NWs. For the bare-core batch, the Au layer was deposited by electron-beam evaporation, whereas for the core–shell batch, the Au was deposited on heated substrate *in situ* in an MBE growth chamber. The WZ GaAs core below the insert was grown for 17 min at a substrate temperature of ∼540 °C under an As_4 flux of 6×10^{-6} Torr and at a growth rate of ∼0.7 MLs^{-1}. The ZB GaAsSb insert was grown for 30 s under a Sb_2 flux of 6×10^{-7} Torr. For both batches, a flux interruption for 1 min, with all the MBE shutters and As and Sb valves closed, was introduced immediately after the growth of the GaAsSb insert. The growth of the WZ GaAs core was continued by opening the Ga shutter 2 s before the As valve and shutter. The WZ GaAs core above the insert was grown for 17 and 8 min for the bare-core and the core–shell NWs, respectively. The core–shell NWs had in addition a radial AlGaAs shell around the NW core in order to passivate the GaAs and GaAsSb core interface states. The AlGaAs shell, with nominal 30% Al as calibrated for two-dimensional growth on ZB GaAs(001), was grown for 15 min at ∼540 °C under an As_2 flux of 6×10^{-6} Torr. Above the core–shell NW segment, an axial AlGaAs segment forms as well during the radial shell growth [23]. The core–shell NWs were capped by a thin GaAs layer (grown for 5 min at ∼400 °C) to prevent oxidation of the AlGaAs shell. More details on the growth procedures can be found elsewhere [12, 13, 23].

2.2. Specimen preparation

The NWs were scratched off the substrate, dispersed in isopropanol and drop-cast onto TEM grids. In the initial TEM study and in the compositional studies (EDX, quantitative HAADF STEM), 2000 mesh Cu grids with graphene support (Graphene Supermarket Ltd) were used. For the correlated μ-PL and (S)TEM study, 200 μm thick Si TEM grids with nine windows of a 50 nm thick amorphous SiN film (Thinwindows Inc.) were used. NWs from the core–shell samples were initially selected by optical microscopy and the single NWs were subsequently identified by low voltage (S)TEM or TEM. In the bare-core samples, single NWs were initially selected by 30 kV STEM (Hitachi S5500). Further details on the μ-PL-TEM method have been reported elsewhere [24].

2.3 Micro-photoluminescence

μ-PL measurements were carried out using a low vibration optical cryostat (Janis ST-500) with a piezo-driven sample stage. The NWs were excited by a 532 nm laser line at a temperature of ∼20 K. The power density at the sample was varied from ∼30 to ∼8500 W cm^{-2}. The laser (spot size ∼1.5 μm) was focused onto a single NW using a long working distance microscope objective lens (50 ×, NA 0.65, M Plan Apo NIR HR, Mitutoyo). The PL from the NWs was collected by the same lens, dispersed by a spectrograph (Horiba iHR550) and detected by a thermoelectric cooled Andor Newton Si electron multiplying charge-coupled device (EMCCD). The spectral resolution of the system is about 200 μeV.

2.4 TEM, EDX and HAADF STEM

The structural characterization was performed on a Philips CM30 (LaB_6) TEM and a JEOL 2010F TEM/STEM (Schottky field emission gun, $C_s = 1$ mm), both operating at 200 kV. The NW crystal phase was analyzed by bright field (BF) and dark field (DF) TEM, selected area electron diffraction (SAED) and high-resolution TEM (HRTEM) lattice imaging. HRTEM, HAADF STEM and EDX analyses were performed on the JEOL 2010F. EDX analysis was performed in STEM mode (probe size 0.7 or 1 nm, condenser aperture 50 or 70 μm). The EDX system was equipped with a Si drift detector with a collection angle of 0.23 sr (INCA, Oxford Instruments Ltd). To avoid the effects of channeling on the EDX signal [25], the NWs were kept off a major zone axis, in most cases slightly off the [1 1 0] zone axis. The spatial resolution of the point analysis was estimated to be ∼5 nm for the bare-core NWs in the present analytical set-up.

To study the composition variation along the GaAsSb inserts, EDX line scans were performed for ∼45 min (total number of counts in the order of 1–4 $\times$ 10^6) along the inserts, starting from and ending in a WZ GaAs region below or above the insert. For quantitative EDX, point scans were performed at several different positions along the inserts for a live time of 200–300 s (total number of counts in the order of 1–9 $\times$ 10^5). The Ga, As and Sb concentrations within the GaAsSb inserts were determined by the INCA software quantification routine using the NW thicknesses and the k-factors calculated by the INCA software. For core–shell NWs, the Al in the shell was taken into account for the quantification of the Sb concentration.

For some representative ZB GaAsSb inserts in bare-core NWs, the Sb concentration was additionally determined by quantitative HAADF STEM analysis, i.e. by performing quantitative comparisons between simulated and experimental HAADF image intensities [18]. Images along the [1 1 0] axis for ZB GaAsSb were recorded using a probe-forming aperture semi-angle of 8.4 mrad, probe size of approximately 0.2 nm. The annular dark field (ADF) detector covered an angular range from 29 to 114 mrad. Simulations for ZB GaAsSb inserts for different Sb concentrations x, in $GaAs_{1-x}Sb_x$, and thicknesses were performed with the STEMsim software [26], based on the frozen-lattice multislice method. Static atomic displacements, caused by Sb being introduced into the GaAs lattice [27], as well as increase in the unit cell size with increasing Sb concentration, were taken into account in the simulations. In order to compare the experimental and simulated intensities, the experimental images were normalized relative to the incident probe intensity [18]. In addition, intensities relative to pure GaAs intensity (I/I_{GaAs}) were employed in the analysis in order to make it more robust for instance in terms of small errors in thickness determination. For more details on the simulations and the quantification approach, see Kauko *et al* [19].

3. Results and discussion

3.1. Structural characterization by conventional TEM techniques

The basic structural characterization of NWs from both batches was carried out using BF and DF TEM, SAED and HRTEM. The bare-core NWs had a diameter of ∼45–80 nm, whereas the diameter of the core–shell NWs was in the range of ∼70–140 nm. It was confirmed that the GaAs core below and above the GaAsSb insert has predominantly WZ crystal phase with a random density and distribution of stacking faults (SFs) for both batches. The WZ GaAs core directly below the insert has no other defects than SFs. The GaAsSb inserts have a ZB crystal phase (see figure 1), and for some NWs (∼25%) the insert consists of two or more twinned segments (figure 1(*a*)). In the WZ GaAs core directly above the insert, there is a random distribution of SFs as well, and some NWs (∼25%) have a 4H polytype segment at the upper insert interface (figure 1(*b*)). This is in agreement with the TEM characterization of similar NWs reported previously [12, 24]. Many NWs have an SF, twinned with respect to the insert, at the very interface (lower and/or upper) with the WZ GaAs core (figure 1(*c*)). A twinned SF can be single, i.e. a unit ZB layer ABC (0.98 nm), or a longer ZB layer, ABCA (1.30 nm) or ABCAB (1.63 nm), where A, B and C represent Ga-As bilayers. To summarize, roughly half of all studied NWs have a twinned insert, a twinned SF at the lower and/or upper insert interface or a 4H polytype segment above the insert, or a combination of these defects. Compared to a previous study without a flux interruption after the growth of the insert [12], the flux interruption introduced here is found to reduce but not to completely prevent the formation of the 4H polytype segment at the upper insert interface.

3.2 The Sb concentration analysis by EDX

Figure 2 shows the maximum Sb concentration within the ZB GaAsSb insert as a function of the insert length for 31 NWs from the two batches, out of which 17 NWs were part of the correlated μ-PL-(S)TEM study discussed in section 3.4. The Sb concentrations presented in figure 2 were determined by EDX point analysis. For the bare-core NWs, a clear trend can be observed in this plot: the longer the insert the higher the Sb concentration. For the core–shell NWs, the data is more scattered and no such trend can be observed. Furthermore, the plot shows that the core–shell NWs have in general lower Sb concentrations, shorter inserts (∼30–55 nm) and less variation in lengths as compared to the bare-core NWs (∼20–80 nm).

The GaAsSb insert length was determined from the crystal phase, i.e. as the length of a single or twinned ZB segment between the WZ GaAs segments (or between WZ and 4H GaAs). The EDX point analysis indicated that there was no Sb in the 4H segments. Longer twinned ZB segments (see figures 1(*a*) and 3) were included in the insert length since the EDX point analysis indicated presence of Sb in such segments. Twinned SFs, at the lower and/or upper insert interfaces, were not added to the insert length. Due to the limited spatial resolution of the EDX point analysis, it was not

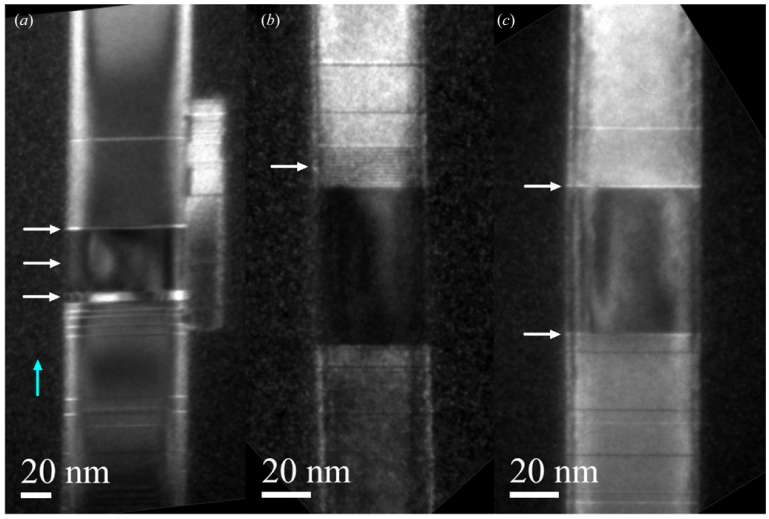

Figure 1. DF TEM images of bare-core NWs with a ZB GaAsSb insert: (*a*) 47 nm long with two twinned segments, 7 nm and 40 nm, and a 2 nm long twinned SF at the upper interface; (*b*) 64 nm long with a 4H polytype segment at the upper interface; (*c*) 59 nm long with twinned SFs at both insert interfaces. All three NWs have SFs both below and above the insert. The white arrows indicate special features such as: twinned segments in (*a*), 4H polytype in (*b*) and twinned SFs in (*c*). The blue (vertical) arrow in (*a*) indicates the $[0\ 0\ 0\ 1]_{WZ}$ ($[1\ 1\ 1]_{ZB}$) growth direction for the NWs.

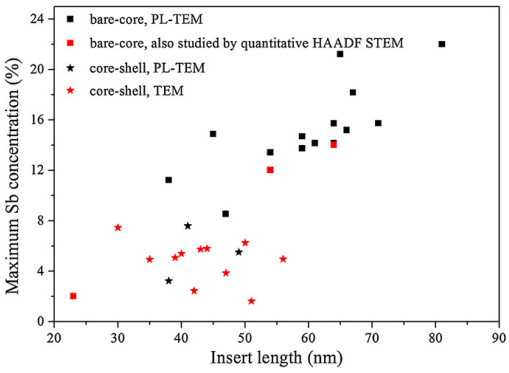

Figure 2. The maximum Sb concentration within the ZB GaAsSb insert, as determined by the EDX point analysis, as a function of the insert length, for bare-core NWs (squares) and core–shell NWs (stars). The three bare-core NWs marked by red squares were studied by quantitative HAADF STEM as well. The NWs marked by black squares/stars were part of the correlated μ-PL-(S)TEM study. The core–shell NWs marked by red stars were studied only by TEM and EDX.

possible to prove whether the short twinned segments (<5 nm) and twinned SFs at the insert interfaces contained Sb.

To determine where in the GaAsSb insert the maximum Sb concentration is reached, EDX point analyses were performed at several points along the insert at the uniformly thick central part of the NW. For all inserts, a clear variation of the Sb concentration values along the insert was observed. The maximum values were found approximately at the insert center for most of the bare-core NWs, or within the upper half of the insert for a few of the bare-core NWs. For most of the core–shell NWs, the maximum Sb concentration was found within the upper half of the insert. For both bare-core and core–shell batches, a much lower Sb concentration was measured in the vicinity (∼5–10 nm) of the insert interfaces than in the central region of the insert.

To study the observed Sb concentration variation within the inserts in more detail, EDX line scans were performed. Comparisons between Sb L_α EDX line scan profiles along the insert for two bare-core NWs with a short and a long insert, and two core–shell NWs with similar insert lengths, are shown in figures 3(*a*) and (*b*), respectively. The Sb concentrations indicated in figure 3 are the maximum values as determined by the EDX point analysis. The specific structural characteristics of the NWs shown in figure 3 are described in the following. The bare-core NW with 22% Sb has an 81 nm long defect-free insert and some SFs in the WZ GaAs core below and above the insert. The bare-core NW with 8.5% Sb, which is presented in figure 1(*a*), has a twinned insert (two twin planes), where the two twinned segments (7 nm and 40 nm long) contain Sb, and one 2 nm long twinned SF at the upper GaAsSb/GaAs interface, which may or may not contain Sb. The core–shell NW with 3.2% Sb has a 38 nm long defect-free ZB insert. The core–shell NW with 7.6% Sb also has a twinned insert (one twin plane): 35 nm and 6 nm long twinned segments. The insert was followed by a 35 nm long Sb-free 4H polytype GaAs.

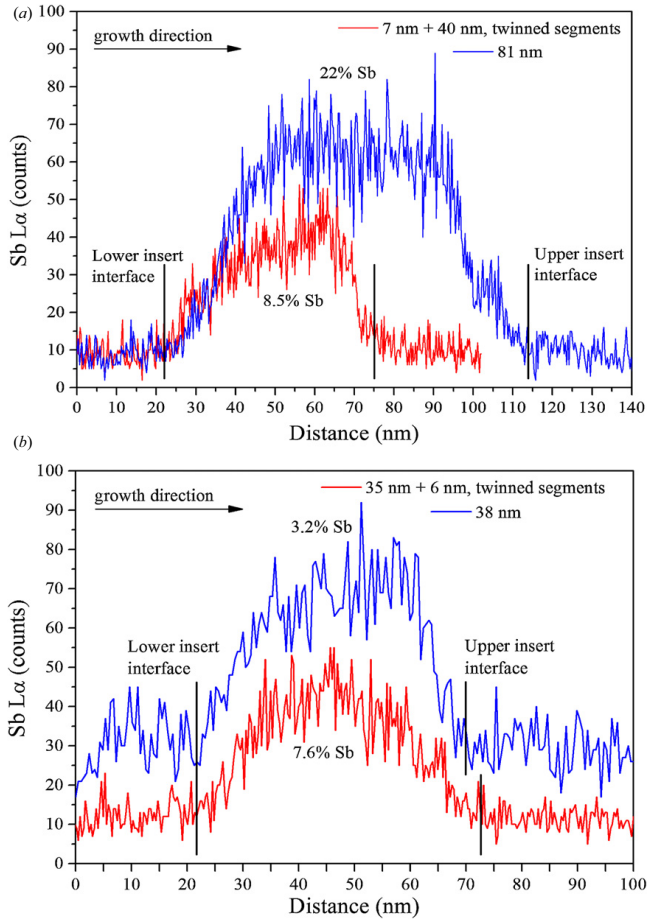

Figure 3. Sb L_α EDX line scan profiles along the ZB GaAsSb inserts for two (*a*) bare-core and (*b*) core–shell NWs. Lower and upper insert interfaces are indicated with the vertical black lines. The drift along the NW growth axis during the EDX line scan was ∼6 nm for the NW with 8.5% Sb and ∼10 nm for the other three NWs, which results in Sb-rich region appearing longer than the actual insert length. In addition, there was a small amount of drift perpendicular to the growth direction for all four NWs, but the line scans remained within the uniformly thick central region.

The Sb L_α EDX line scan profiles in figure 3 indicate that the Sb concentration increases gradually from the lower insert interface, reaches a maximum value at or just above the insert center and decreases, with a similar slope as the increase, towards the upper insert interface. Moreover, the distance over which the Sb concentration increases or decreases varies with the insert length. For shorter inserts this happens over ∼5–10 nm, whereas for longer inserts (>60 nm) the region with a graded Sb concentration spans over ∼20 nm or more. For some NWs, the Sb L_α EDX line scan profile is fairly symmetric (see for example the NWs with 22% and 7.6% Sb in figure 3), whereas for others, a slightly steeper slope occurs towards the upper insert interface (see for example the NWs with 8.5% and 3.2% Sb in figure 3). For NWs with longer inserts (especially for lengths > 60 nm), the Sb concentration reaches a maximum value and remains approximately constant over the central region of the insert (up to 20 nm). This was the case for the bare-core NW with 22% Sb in figure 3(*a*). Indeed, the value of 20–22% was confirmed with the EDX point analysis at several points near the insert center for this NW. For NWs with short inserts (<40 nm), a plateau with a constant Sb concentration was never observed. The results presented in figures 2 and 3 are discussed further below in terms of growth kinetics.

Before the Sb flux is switched on for the ZB GaAsSb insert growth, the Au, Ga and As content in the catalyst droplet have reached a stable state, for the Ga and As fluxes used for WZ GaAs growth. After the Sb flux is switched on, GaAsSb growth starts and the crystal phase switches to ZB [11, 12]. The Sb concentration in the Au droplet and the insert

starts to build up from 0%, creating the graded region with increasing Sb concentration in the lower part of the insert. The Sb concentration in the Au droplet and the GaAsSb insert increases with the insert growth time, until an equilibrium between Au, Ga, As and a few per cent of Sb in the Au droplet is established, or the flux interruption is introduced. The Sb plateau in the central region of the insert, as seen by the NW with 22% Sb in figure 3(*a*), indicates that the equilibrium in the Au droplet is achieved for the NWs with long inserts during the 30 s of the nominal insert growth. After the 30 s of insert growth, the flux interruption is introduced in order to reduce the Sb content in the Au droplet [28] and on the NW side walls [29], before the WZ GaAs core growth is continued. During the first stage of the 1 min flux interruption, we expect that the ZB GaAsSb insert continues to grow fueled by remaining 'surplus' of Ga, As and Sb in the Au droplet and adatoms diffusing up the NW sidewalls, until a new 'no growth' equilibrium situation is established. However, this would result in only a few additional nms of the ZB GaAsSb insert, and thus cannot explain the extended graded region with decreasing Sb concentration observed in the upper part of the inserts. We believe that at this point, the growth has reached the end of the central region of the insert with a maximum Sb concentration, i.e., the Sb mole fraction does not change significantly during the GaAsSb growth that occurs during the initial stage of the 1 min flux interruption. When Ga and As fluxes are switched on again for the WZ GaAs core growth, at first the ZB GaAsSb insert will continue to grow, with decreasing Sb mole fraction, until the Au droplet is sufficiently emptied of Sb under the new equilibrium conditions. The observed almost equal lengths of the graded regions in the lower and upper part of the inserts also suggest that the flux interruption itself has a minor effect on the total Sb profile. Thus, the graded region with decreasing Sb concentration towards the upper insert interface occurs due to a decreasing Sb content in the Au droplet during the initial stage of nominal GaAs growth after the flux interruption. The total ZB GaAsSb insert length (as measured by TEM) is hence longer than the length grown during the 30 s when the Sb flux was on.

Since the GaAsSb inserts were grown for approximately the same time in total for both batches, the large range of insert lengths (altogether ∼20–80 nm, see figure 2) indicates that the insert growth rate varied from NW to NW. On average longer inserts for the bare-core NWs imply higher growth rates than for the core–shell NWs. The growth rate for Au-assisted NWs depends on the NW diameter [30, 31] in such a way that the NWs with smaller diameters grow faster than those with larger diameters. The increase of insert length with decrease of NW diameter was indeed observed for the bare-core NWs (not shown). For the core–shell NWs no direct relation between the NW core diameter and the growth rate can be drawn, since the core diameter could not be measured directly. However, the narrower range of insert lengths and shorter inserts for the core–shell NWs indicate indirectly that this batch has on average larger NW core diameters and less variation in the Au droplet size than in the bare-core batch. It should be noted that for this batch, the Au was deposited *in situ* in an MBE growth chamber on a heated substrate, which normally (depending on temperature and Au flux) gives less variation in the Au droplet sizes as compared to when depositing Au on the substrate *ex situ* by electron-beam evaporation.

During the GaAsSb insert growth, there is a competition between Sb and As for incorporation into the insert [29, 32]. In the case of two-dimensional growth, Sb is incorporated more efficiently into GaAsSb at higher growth rates than at lower growth rates [32]. If the same trend applies for NW growth, it could partly explain the increase of the Sb concentration with increase of the insert length observed in figure 2. However, more investigation is needed in order to clarify why the higher growth rate of thin NWs causes inserts with higher Sb concentrations than in thicker NWs with lower growth rate. More homogeneous Au droplet size and distribution should be targeted to achieve a uniform growth rate and thereby reduce the distribution in the insert length and composition.

So far, the EDX results have been used to qualitatively correlate the Sb concentrations and the GaAsSb insert lengths, and a clear trend was observed for the bare-core NWs in figure 2. If we assume that the same trend should be expected for the core–shell NWs, the scattered distribution of the Sb concentrations would indicate that the EDX quantification was less accurate than for the bare-core NWs. It is known that EDX in TEM has inherent drawbacks [25] such as a low count rate, poor detection efficiency (detection limit of a few atomic percent depending on the element), limited spatial resolution (probed volume wider than the probe size), beam-broadening within the specimen, variation due to channeling effects and specimen drift. Therefore, the EDX quantification of the Sb concentration in the ZB GaAsSb inserts has to be treated with caution, especially for the core–shell NWs or at lower concentrations. Furthermore, the here applied quantification of the EDX data by the INCA software does not consider relative orientation between the electron beam and the crystal lattice, the effects of crystal phase and NW morphology (hexagonal cross-section). The INCA software uses calculated k-factors which are based on a flat geometry with a uniform composition. A manual Cliff–Lorimer determination of the ZB GaAs k-factor for quantifying the Sb concentration more correctly in the ZB GaAsSb insert could not be used here as no reference ZB GaAs region was available in the same NWs.

3.3. The Sb concentration analysis by quantitative HAADF-STEM

To verify the Sb concentration values and the qualitative profiles obtained by the EDX analysis, some bare-core NWs (indicated with red squares in figure 2) were additionally analyzed by quantitative HAADF STEM. Results from two bare-core NWs, with a short and a long insert, are presented in figures 4 and 5, respectively. The experimental HAADF STEM intensity profiles across the insert were taken from a 3 nm wide region near the insert center, indicated with the red boxes in figures 4(*b*) and 5(*b*). The simulated intensity profile across the insert was generated using the known thickness profile and assuming a radially uniform distribution of Sb and a Sb concentration based on the experimental intensity

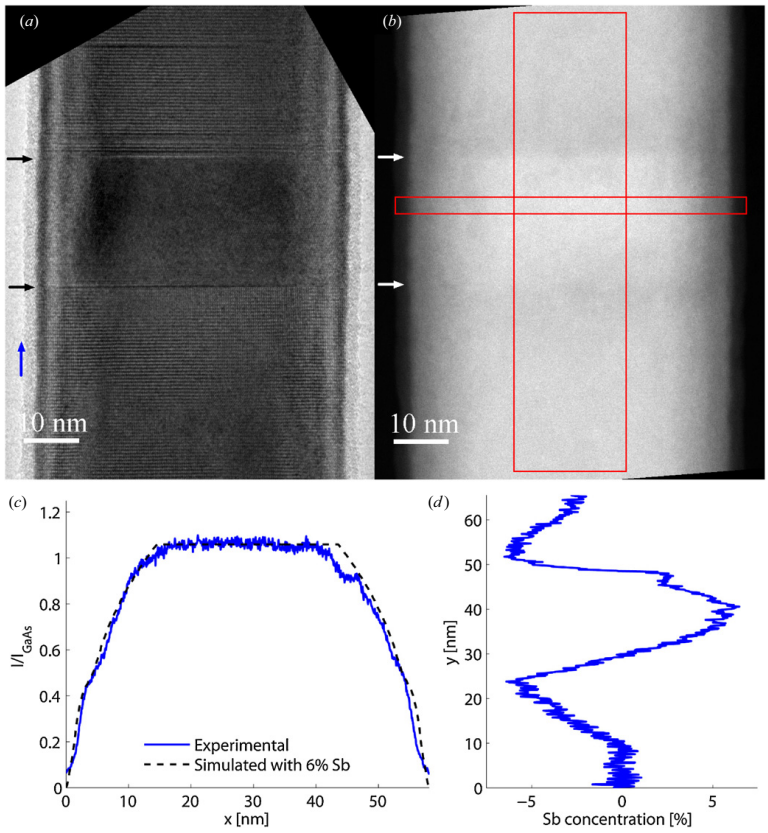

Figure 4. A bare-core NW with a 23 nm long ZB GaAsSb insert. (*a*) HRTEM image. The blue (vertical) arrow shows the growth direction. (*b*) HAADF STEM image. The black and white arrows in (*a*) and (*b*), respectively, mark the insert interfaces. (*c*) Relative HAADF STEM intensity profiles across the insert (*x*-direction, horizontal in (*a*, *b*)): the experimental profile (solid blue line) averaged over the 3 nm wide red box in (*b*), and the simulated profile (dashed black line) assuming a radially uniform Sb distribution with 6% Sb. (*d*) The Sb concentration profile along the insert (*y*-direction, vertical in (*a*, *b*)), obtained from HAADF STEM intensity profile averaged over the 20 nm wide red box in (*b*). Note that the negative values at the interfaces are not related to composition variations, but are due to dechanneling related to surface strain relaxation and/or the SFs [19, 33].

level at the central part of the cross-sectional profile. The Sb concentration profiles along the inserts, shown in figures 4(*d*) and 5(*d*), were obtained by quantifying the HAADF STEM intensities averaged along the uniformly thick central part of the NWs, indicated by the ∼20 nm wide red boxes in figures 4(*b*) and 5(*b*).

The NW presented in figure 4 has a 23 nm long ZB GaAsSb insert and some SFs above the insert, as seen in the HRTEM image (figure 4(*a*)). The maximum Sb concentration along the insert obtained by quantitative HAADF STEM ($6 \pm 1\%$) is higher than the EDX point analysis result (2% at the insert center). The simulated HAADF STEM intensity profile across the insert, assuming a radially uniform Sb concentration of 6% (figure 4(*c*), dashed black line), matches well the experimental HAADF STEM intensity profile (figure 4(*c*), solid blue line). The Sb concentration profile along the insert (figure 4(*d*)), taken from the 20 nm wide red box in figure 4(*b*), is slightly asymmetric and steeper towards the upper insert interface. The increase of the Sb concentration extends from the lower insert interface for ∼15 nm. The maximum Sb concentration (6%) is reached for this insert exactly at the position of the 3 nm wide red box in figure 4(*b*), which is located slightly above the insert center. The profile displays no plateau of a constant Sb concentration, and the concentration starts to decrease towards the upper insert interface immediately above the narrow region with the maximum Sb concentration. This is in accordance with observations from the EDX line scans for shorter inserts. The negative Sb concentrations which occur around the insert interfaces (figure 4(*d*)), corresponding to a lower intensity in the HAADF STEM image (figure 4(*b*)), are not a real compositional effect but caused by dechanneling related

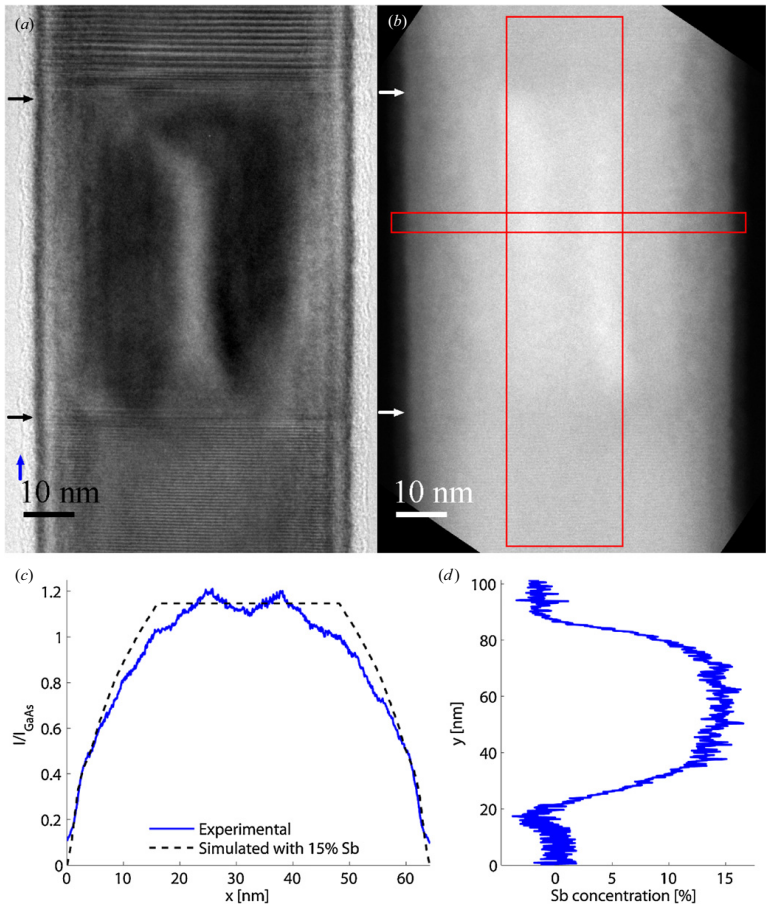

Figure 5. A bare-core NW with a 64 nm long ZB GaAsSb insert: (*a*) HRTEM image. (*b*) HAADF STEM image. The arrows in (*a*) and (*b*) mark the growth direction and the insert interfaces as in figure 4. (*c*) Relative HAADF STEM intensity profiles across the insert (*x*-direction, horizontal in (*a*, *b*)): the experimental profile (solid blue line) averaged over the 3 nm wide red box in (*b*), and the simulated profile (dashed black line) assuming a radially uniform Sb distribution with 15% Sb. (*d*) The Sb concentration profile along the insert (*y*-direction, vertical in (*a*, *b*)), obtained from HAADF STEM intensity profile averaged over the 22.5 nm wide red box in (*b*).

to surface strain relaxation at the insert interfaces and/or the SFs [33].

The NW shown in figure 5 has a 64 nm long insert, which corresponds to the average insert length for the bare-core NWs. This NW has also a 20 nm long 4H GaAs polytype segment directly above the ZB GaAsSb insert. Regions with varying intensity can be observed within the insert in both the HRTEM (figure 5(*a*)) and the HAADF STEM images (figure 5(*b*)). This indicates the presence of strain and/or an inhomogeneous Sb distribution within the insert. Similar strain-related intensity variations were observed within the inserts in BF/DF TEM images for nearly all NWs analyzed in this work (see for example the three inserts in figure 1), especially for those with longer inserts and higher Sb concentrations. This was not observed for very short inserts in bare-core NWs, such as the NW in figure 4.

The maximum Sb concentration along the insert is found to be 15 ± 4% for this NW. To obtain this value, the HAADF intensity was averaged over 0.5–0.6 of the central evenly thick region as the intensity profile fluctuates due to strain and/or an inhomogeneous Sb distribution within the insert. The high uncertainty in the maximum Sb concentration reflects these fluctuations. This value corresponds to the concentration found by EDX point analysis at the insert center (14%). For the third NW analyzed by quantitative HAADF STEM (not shown here), there was also a similar agreement: quantitative HAADF STEM resulted in 13 ± 4% Sb concentration whereas the EDX point analysis gave 12% Sb concentration. The Sb concentration profile along the insert (figure 5(*d*)) appears to be

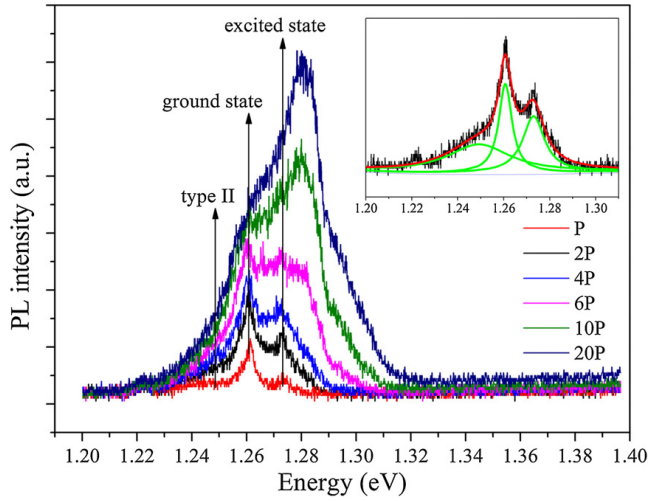

Figure 6. Low temperature (20 K) power-dependent PL spectra of the NW shown in figure 1(*c*). Inset: Lorentzian line shape fit of the PL spectrum at a power density of 2P, where $P = 283$ W cm^{-2}.

slightly asymmetric. The increase of the Sb concentration from the lower insert interface occurs over ∼20 nm, and a decrease towards the upper insert interface occurs over ∼15 nm. The Sb concentration reaches a plateau of an almost constant value in the central region of the insert. This Sb concentration profile is qualitatively in agreement with the EDX line scan results for long inserts.

For the NW in figure 5, the experimental HAADF STEM intensity profile (figure 5(*c*), solid blue line) does not fit well to the simulated HAADF STEM intensity profile across the insert, assuming a radially uniform Sb concentration of 15% (figure 5(*c*), dashed black line). This was not the case for the NW in figure 4. At the NW wedges, the experimental intensity is clearly lower than the simulated intensity. A similar discrepancy of the experimental and simulated HAADF STEM intensity profile across the insert was observed for the third NW (13 ± 4% Sb), suggesting that there is a radial Sb concentration gradient in case of a higher maximum Sb content. This mismatch indicates that the Sb concentration is decreasing from the insert center towards the outer surfaces of the NW. It has been observed for ZB GaAsSb inserts in Ga-assisted NWs as well [19]. The radial Sb concentration gradient is probably due to diffusion of Sb towards the outer surfaces and exchange with As at the outer surfaces [29] during the growth of the WZ GaAs core above the insert, or radial GaAs overgrowth. The presence of an outer layer with a reduced Sb content might indicate that the maximum concentration as determined by HAADF STEM is underestimated.

To summarize the structural and compositional analysis based on electron microscopy techniques: both EDX and quantitative HAADF STEM indicate that the here studied ZB GaAsSb inserts have a decreasing Sb concentration towards the interfaces with the upper and lower GaAs segments. The insert length and composition vary from NW to NW. Longer inserts have a higher maximum Sb concentration and a plateau. In addition, radial decrease in the Sb concentration towards the outer surfaces was observed in NWs with higher Sb concentrations. The Sb richest region is hence located axially near the center of the insert and radially around the NW axis. The length of the Sb richest region varies with the maximum Sb concentration and the insert length. The Sb concentrations as determined by HAADF STEM are approximately equal to the Sb concentrations obtained by the EDX quantification for inserts with an average length and an average Sb concentration. For lower concentrations, quantitative HAADF STEM seems to give a higher Sb concentration value than EDX. Therefore an independent approach is needed to verify the concentration analysis based on TEM techniques, specifically for NWs with a low Sb content, or core–shell NWs which could not be studied by quantitative HAADF STEM. Furthermore, it is important to relate the observed compositional variations to the optical properties of these heterostructured NWs.

3.4. Correlated μ-PL-TEM study of the ZB GaAsSb inserts

The same single bare-core and core–shell NWs were studied by μ-PL and TEM-EDX to directly correlate the GaAsSb insert composition to its optical properties. A representative bare-core NW regarding both the structural and optical characteristics (the NW shown in figure 1(*c*)) will be discussed in more detail here. The GaAsSb insert is 59 nm long and the EDX point analysis resulted in 13.7% Sb. Strain contrast is visible within the insert in the DF TEM image in figure 1(*c*). DF TEM further shows that there is a twinned single SF (∼1 nm) at both insert interfaces, and some SFs below and above the insert.

Figure 6 shows the low temperature power-dependent PL spectra of the ZB GaAsSb insert emission for this particular

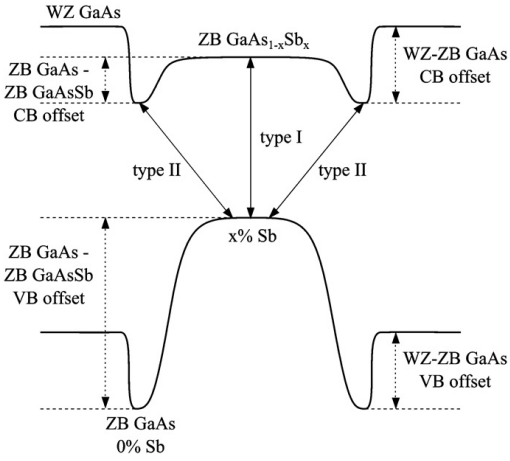

Figure 7. Proposed schematic energy band diagram for a ZB GaAsSb insert with a Sb concentration profile decreasing symmetrically towards the interfaces, within WZ GaAs barriers. ZB GaAs (i.e. 0% Sb) is assumed at the insert interfaces with WZ GaAs. The dashed lines qualitatively indicate the conduction (CB) and valence band (VB) offsets at the insert interfaces and within the insert. The full line arrows indicate two possible optical transition routes within the insert, type I and type II.

NW. A Lorentzian line shape fit at a low excitation power (∼566 W cm^{-2}, inset in figure 6) indicates that there are three distinct PL peaks at 1.249, 1.261, and 1.273 eV. In addition, a very weak PL peak is observed at 1.222 eV (not fitted), which was present in most of the PL spectra and is a spectral artefact. The weak and broad PL peak at 1.249 eV is observed only at low excitation powers. This peak is blueshifted by ∼5 meV at 566 W cm^{-2} compared to the lowest excitation power (283 W cm^{-2}). The PL emission at 1.261 eV, which is the dominant PL peak at the lowest excitation power, is not blueshifted when the excitation power is increased. The PL peak at 1.273 eV saturates at higher power at the same time as another higher energy PL peak (at ∼1.28 eV) appears and the peak becomes dominant at higher excitation powers.

To explain the origin of the insert-related PL peaks, a qualitative energy band diagram for a typical ZB GaAsSb insert in a WZ GaAs NW with a graded Sb concentration towards the insert interfaces, is given in figure 7. This energy band diagram is proposed based on the compositional results presented above (sections 3.1–3.3) and band alignments as suggested in literature [5, 6, 21, 34], as explained in the following. The common understanding is that the WZ GaAs/ZB GaAs heterojunction has a type II band alignment [21, 34] with electrons confined in ZB GaAs and holes confined in WZ GaAs. The band alignment for the ZB GaAs/ZB GaAsSb heterojunction is also considered to be type II, for Sb concentrations below 40%, with electrons weakly confined in ZB GaAs and holes strongly confined in ZB GaAsSb, according to the references [5, 6]. For clarity, we assume a symmetric Sb concentration profile along the insert in figure 7 and defects at the interfaces are not included in this schematic band diagram. Note that the Sb concentration profile is often slightly asymmetric along the insert (see sections 3.2 and 3.3) but this would not affect the following discussion regarding the qualitative energy band diagram. Due to the increasing Sb concentration from the insert interfaces towards the central region of the insert, there are no sharp WZ GaAs/ZB GaAsSb heterojunctions. Instead, the change in the energy band diagram at the interfaces will be as if there is a sharp WZ GaAs/ZB GaAs heterojunction at both the insert interfaces, followed by a graded region with increasing Sb concentration towards the center of the ZB GaAsSb insert. The twinned SFs at the insert interfaces can be considered as ZB GaAs, and in the energy band diagram they can be included into the ZB GaAs region (∼0% Sb) at the beginning and/or at the end of the insert.

The PL peak at 1.249 eV is attributed to the optical transitions between holes confined in ZB GaAsSb in the central region of the insert, and electrons confined in ZB GaAs near the insert interfaces (type II transitions in figure 7). The presence of blueshift for this peak at low excitation powers indicates type II behavior. Note that the radial gradient of the Sb concentration may contribute to this type II transition as well.

The PL peaks at 1.261 and 1.273 eV are attributed to the ground and first excited state of the ZB GaAsSb insert, respectively. The absence of a blueshift for these two PL peaks, as the excitation power increases (see figure 6), is characteristic for type I transitions as reported previously [17, 24]. The ZB GaAsSb insert PL peaks at 1.261 and 1.273 eV are thus assigned to transitions between electrons weakly confined, and holes more strongly confined in the insert (type I transition in figure 7), occurring in the central region of the insert. Thus, the central Sb-richest region of the ZB GaAsSb insert has a type I band alignment with respect to the WZ GaAs barriers.

Further evidence for the type I band alignment is the relatively high PL emission intensity generally obtained from the bare-core NWs, despite the absence of surface passivation by the AlGaAs shell, as shown in figure 6. The radial gradient of the Sb concentration in the GaAsSb insert may act as self-passivation for the bare-core NWs. However, it should be noted that the insert PL emission intensity is in general much higher for the core–shell NWs at similar excitation powers.

Comparison of all bare-core and core–shell NWs with different structural defects in the insert region, as shown in figure 1, resulted in the conclusion that isolated structural defects (single SFs, 4H segment) in the WZ GaAs core, at or near-by the insert interfaces, have no major contribution to the GaAsSb insert PL emission. A small number of twin planes (1–4) within the ZB GaAsSb inserts appear to have no effect on the insert PL emission either. In fact, the most dominant effects are imposed by the graded Sb concentration. The graded concentration profile reduces the effects of planar defects at the interfaces on the GaAsSb PL emission. In previous reports on the same type of heterostructured NWs [12, 14, 24], the influence of ZB GaAs twins and 4H polytype segments on the ZB GaAsSb PL emission was discussed as well, but assuming a constant and uniform Sb concentration within the insert. For instance, it was claimed that a ZB GaAs twin at the upper insert interface induces a type II PL emission [12, 14, 24]. This claim

is in line with the model proposed here as the twin at either insert interface actually falls into the region with a graded Sb concentration, and can even be pure ZB GaAs (close to an interface with WZ GaAs), which results in type II transitions as sketched in figure 7. No obvious PL features indicating the presence of the 4H GaAs segment at the upper insert interface were observed in this work. This is in agreement with the theoretical predictions [35] and our previous observations [24].

The ground state PL emission energies (type I transitions, see figures 6 and 7), obtained by fitting with Lorentzian or Lorentzian–Gaussian line shape functions, were further used to determine the Sb concentrations in the inserts for all the studied bare-core and core–shell NWs. An empirical model for the low temperature bandgap of unstrained bulk $GaAs_{1-x}Sb_x$, according to Teissier *et al* [6], was used to determine the Sb concentration x, from the GaAsSb insert ground state PL emission energy. These results are presented in figure 8(*a*) together with the corresponding values of the Sb concentration obtained with the EDX point analysis. Figure 8(*b*) presents the Sb concentration determined from the PL emission energy as a function of the insert length (analogous to figure 2) and, for comparison, it includes the three NWs studied by quantitative HAADF STEM (section 3.1.3).

For average composition (12–16%), the Sb concentrations determined with EDX point analysis, quantitative HAADF STEM and calculated from the PL emission energies are fairly in agreement, although there is a relatively large variation in the EDX data. There is however a distinct difference in the slopes of Sb concentration versus emission energy based on EDX and PL, which could arise due to two reasons. At a low Sb content (<10%), here especially pronounced for core–shell NWs, the EDX underestimates the Sb content due to the poor sensitivity. In addition, beam-broadening is expected to affect the concentration values for the core–shell NWs more severely, since the probe spreads first in the AlGaAs/GaAs shell-cap and then reaches the GaAsSb insert. At high Sb content (>16%), the unstrained PL model might no longer be valid due to strain.

The graph in figure 8(*b*) shows a trend similar to the one in figure 2: the calculated Sb concentration increases with increasing insert length, which is reflected in a decreasing ZB GaAsSb PL emission energy (figure 8(*a*)). As observed in figure 2, the inserts are generally shorter and the Sb concentrations lower in the core–shell NWs compared to the bare-core NWs. Here, however, the same trend between the Sb concentrations and the insert lengths is present for the core–shell NWs as well, which could not be concluded based on the EDX point analysis only. Since both bare-core and core–shell NWs with a wide range of Sb concentrations (∼6–16%) display the same trend (figure 8(*b*)) and strain is present in the inserts, we conclude that the additional strain induced by the AlGaAs shell has no major effect on the ZB GaAsSb insert PL emission energy for the Sb concentrations studied in this work. In addition, this trend indicates that the AlGaAs shell growth in the core–shell NWs induces no observable decrease of the Sb concentration in the GaAsSb inserts. Furthermore, if we assume that the insert length is an indication of the Sb concentration, there is a good agreement of the Sb concentrations calculated from the PL energy with the ones determined with the quantitative HAADF-STEM over the Sb concentration range presented in this study (figure 8(*b*)).

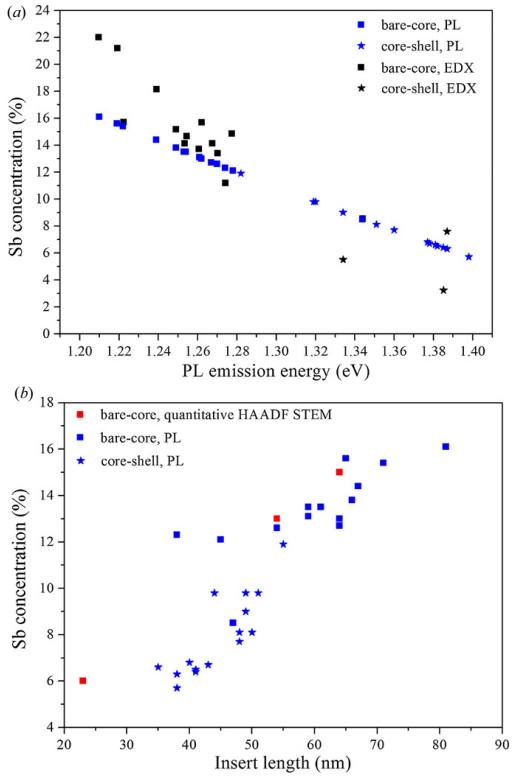

Figure 8. (*a*) The Sb concentration determined from the PL emission energy (all 29 PL-TEM NWs represented, blue symbols) and by point EDX (17 of 29 PL-TEM NWs, as given in figure 2, black symbols), as a function of the GaAsSb insert PL emission energy for the bare-core (squares) and core–shell (stars) NWs. (*b*) The Sb concentration determined from the GaAsSb insert PL emission energy (blue symbols) for the 29 PL-TEM NWs presented in (*a*) as a function of the insert length as determined by TEM. The bare-core NWs studied by quantitative HAADF STEM (red squares) are included for comparison.

It should be emphasized that the correlated μ-PL-TEM approach can be used to estimate the Sb concentrations for both bare-core and core–shell NWs. In contrast, the Sb concentrations determined by EDX can be inaccurate for the core–shell NWs with lower Sb concentration (<10%). Presently, the quantitative HAADF STEM approach used here for the bare-core NWs cannot be applied to the core–shell NWs as we had no suitable model to account for the high-angle electron scattering from the AlGaAs shell. The HAADF STEM approach could neither be applied on NWs on 50 nm thick SiN supports used for correlated μ-PL-TEM, as the relatively thick support affects the overall image intensity and hence the quantification.

Based on the presented structural, compositional and optical characterization, we believe that the graded Sb sections need to be considered as one of the main NW parameters for optoelectronic performance optimization. At the lower interface the graded section will depend on the applied Sb flux and the growth rate. However, an abrupt profile is difficult to realize due to the required build-up of Sb in Au droplet. For the upper interface the Sb profile might become more abrupt, and the defect density might be reduced further, by a longer flux interruption. For pure type I optical properties the graded sections at both interfaces should have abrupt Sb profiles. An advantage of the graded interfaces is that varying defect distribution at the interfaces has less influence on the optical properties of these heterostructured NWs.

4. Conclusions

In this work, the Sb concentration distribution within and variation among the ZB GaAsSb inserts in WZ GaAs bare-core and WZ GaAs/AlGaAs core–shell NWs grown by Au-assisted MBE was investigated comparing three different characterization methods: EDX analysis, quantitative HAADF STEM and correlated μ-PL-TEM. A variation in the insert lengths and Sb concentrations was observed especially for the bare-core NWs. A trend of increasing Sb concentration with increasing insert length was evident from the EDX results for bare-core NWs, and from the correlated PL-TEM results for all the NWs. This trend is due to a distribution of sizes of the Au droplets, resulting in a variation in the NW (core) diameters and consequently the growth rates. Furthermore, EDX and quantitative HAADF STEM analyses confirmed that there is a region with a graded Sb concentration within the insert near both insert interfaces. Quantitative HAADF STEM analysis additionally indicated that there is a radial Sb concentration gradient, with a lower Sb concentration towards the outer surfaces, which is more pronounced for inserts with a higher maximum Sb concentration. All these findings imply that the Sb richest region is located axially near the center of the insert and radially around the NW axis.

For bare-core NWs the quantitative HAADF STEM analysis resulted in approximately equal Sb concentrations as the quantification by EDX point analysis for an average insert length and composition (12–16%). The Sb concentrations obtained from EDX and PL, based on an unstrained model, were also in agreement for inserts with the average Sb concentrations. However, for Sb concentrations $x < 10\%$ and for the core–shell NWs, EDX underestimates the Sb content. For higher Sb concentrations ($x > 16\%$) quantification by unstrained PL model might be inaccurate due to strain.

The observed Sb concentration profile along the insert induces both type I and type II transitions within the ZB GaAsSb insert. The type I transitions occur within the central Sb-richest region of the insert and dominate in the insert-related PL emission. The observed weak type II transitions originate from recombination of holes in the valence band of the central region of the insert and electrons in the conduction band of the regions near the insert interfaces, due to the decreasing Sb concentration towards the interfaces with the WZ GaAs core. No pronounced influence of the structural defects (SFs, 4H segment) in the adjacent WZ GaAs core on the GaAsSb insert PL emission was found.

Acknowledgments

This work was supported by the 'RENERGI' (grant no 190871) and 'NANOMAT' programs (grant no 182091) of the Research Council of Norway, and by the Norwegian University of Science and Technology (NTNU).

References

[1] Björk M T, Thelander C, Hansen A E, Jensen L E, Larsson M W, Wallenberg L R and Samuelson L 2004 *Nano Lett.* **4** 1621–5
[2] van Kouwen M P, van Weert M H M, Reimer M E, Akopian N, Perinetti U, Algra R E, Bakkers E P A M, Kouwenhoven L P and Zwiller V 2010 *Appl. Phys. Lett.* **97** 113108
[3] Claudon J, Bleuse J, Malik N S, Bazin M, Jaffrennou P, Gregersen N, Sauvan C, Lalanne P and Gérard J-M 2010 *Nature Photon.* **4** 174–7
[4] Prins A, Dunstan D, Lambkin J, O'Reilly E, Adams A, Pritchard R, Truscott W and Singer K 1993 *Phys. Rev.* B **47** 2191–6
[5] Liu G, Chuang S-L and Park S-H 2000 *J. Appl. Phys.* **88** 5554–61
[6] Teissier R, Sicault D, Harmand J C, Ungaro G, Le Roux G and Largeau L 2001 *J. Appl. Phys.* **89** 5473–7
[7] Vurgaftman I, Meyer J R and Ram-Mohan L R 2001 *J. Appl. Phys.* **89** 5815–75
[8] Wang J B, Johnson S, Chaparro S, Ding D, Cao Y, Sadofyev Y, Zhang Y H, Gupta J and Guo C 2004 *Phys. Rev.* B **70** 195339
[9] Sadofyev Y G and Samal N 2010 *Materials* **3** 1497–508
[10] Baranowski M, Syperek M, Kudrawiec R, Misiewicz J, Gupta J A, Wu X and Wang R 2011 *Appl. Phys. Lett.* **98** 061910
[11] Dheeraj D L, Patriarche G, Largeau L, Zhou H L, van Helvoort A T J, Glas F, Harmand J C, Fimland B O and Weman H 2008 *Nanotechnology* **19** 275605
[12] Dheeraj D L, Patriarche G, Zhou H, Hoang T B, Moses A F, Grønsberg S, van Helvoort A T J, Fimland B-O and Weman H 2008 *Nano Lett.* **8** 4459–63
[13] Dheeraj D L, Patriarche G, Zhou H, Harmand J C, Weman H and Fimland B O 2009 *J. Cryst. Growth* **311** 1847–50
[14] Hoang T B, Moses A F, Ahtapodov L, Zhou H, Dheeraj D L, van Helvoort A T J, Fimland B O and Weman H 2010 *Nano Lett.* **10** 2927–33
[15] Plissard S, Dick K A, Wallart X and Caroff P 2010 *Appl. Phys. Lett.* **96** 121901
[16] van Helvoort A T J, Dheeraj D L, Zhou H, Grønsberg S, Patriarche G, Fimland B and Weman H 2010 *J. Phys.: Conf. Ser.* **241** 012084
[17] Todorovic J, Moses A F, Dheeraj D L, Olk P, Fimland B O, Weman H and van Helvoort A T J 2011 *J. Phys.: Conf. Ser.* **326** 012043
[18] Rosenauer A, Gries K, Müller K, Pretorius A, Schowalter M, Avramescu A, Engl K and Lutgen S 2009 *Ultramicroscopy* **109** 1171–82
[19] Kauko H, Grieb T, Bjørge R, Schowalter M, Munshi A M, Weman H, Rosenauer A and van Helvoort A T J 2013 *Micron* **44** 254–60
[20] Bao J, Bell D C, Capasso F, Wagner J B, Mårtensson T, Trägårdh J and Samuelson L 2008 *Nano Lett.* **8** 836–41
[21] Heiss M *et al* 2011 *Phys. Rev.* B **83** 045303

[22] Jahn U, Lähnemann J, Pfüller C, Brandt O, Breuer S, Jenichen B, Ramsteiner M, Geelhaar L and Riechert H 2012 *Phys. Rev.* B **85** 045323
[23] Zhou H L, Hoang T B, Dheeraj D L, van Helvoort A T J, Liu L, Harmand J C, Fimland B O and Weman H 2009 *Nanotechnology* **20** 415701
[24] Todorovic J, Moses A F, Karlberg T, Olk P, Dheeraj D L, Fimland B O, Weman H and van Helvoort A T J 2011 *Nanotechnology* **22** 325707
[25] Williams D B and Carter C B 2009 *Transmission Electron Microscopy: A Textbook for Materials Science. Part 4: Spectrometry* 2nd edn (Berlin: Springer)
[26] Rosenauer A and Schowalter M 2008 STEMSIM—a new software tool for simulation of STEM HAADF Z-contrast imaging *Microscopy of Semiconducting Materials 2007* ed A G Cullis and P A Midgley (Springer) pp 170–2
[27] Grillo V, Carlino E and Glas F 2008 *Phys. Rev.* B **77** 054103
[28] Dick K A, Bolinsson J, Borg B M and Johansson J 2012 *Nano Lett.* **12** 3200–6
[29] Yano M, Ashida M, Kawaguchi A, Iwai Y and Inoue M 1989 *J. Vac. Sci. Technol.* B **7** 199–203
[30] Plante M C and LaPierre R R 2006 *J. Cryst. Growth* **286** 394–9
[31] Dubrovskii V G and Sibirev N V 2007 *J. Cryst. Growth* **304** 504–13
[32] Selvig E, Fimland B O, Skauli T and Haakenaasen R 2001 *J. Cryst. Growth* **227–228** 562–5
[33] Grillo V 2009 *Ultramicroscopy* **109** 1453–64
[34] De A and Pryor C E 2010 *Phys. Rev.* B **81** 155210
[35] Belabbes A, Panse C, Furthmüller J and Bechstedt F 2012 *Phys. Rev.* B **86** 075208

Paper III

Antimony surface depletion during the growth of GaAsSb and GaAs/GaAsSb nanowires

H. Kauko, B. O. Fimland, T. Grieb, A. M. Munshi, A. Rosenauer and A. T. J. van Helvoort

In preparation.

Antimony surface depletion during the growth of GaAsSb and GaAs/GaAsSb nanowires

H. Kauko,[1] B. O. Fimland,[2] T. Grieb,[3] A. M. Munshi,[2] A. Rosenauer,[3] and A. T. J. van Helvoort[1, a)]

[1)] *Department of Physics, Norwegian University of Science and Technology (NTNU), Trondheim, Norway*

[2)] *Department of Electronics and Telecommunications, NTNU, Trondheim, Norway*

[3)] *Institut für Festkörperphysik, Universität Bremen, Bremen, Germany*

(Dated: November 21, 2013)

Surface depletion of Sb during the growth of GaAsSb nanowires (NWs) and GaAs NWs with GaAsSb inserts has been studied using quantitative high angular dark field scanning transmission electron microscopy, employing a model for diffusion of Sb in the hexagonal NWs. GaAsSb NWs grown with Ga-assisted molecular beam epitaxy (MBE), and GaAs/GaAsSb NWs grown with Ga- and Au-assisted MBE were investigated. At the high temperatures employed in the NW growth, As-Sb exchange and diffusion of Sb towards the the outer surface takes place, resulting in surface depletion of Sb in the GaAsSb NWs and the GaAsSb inserts. In GaAsSb NWs, increasing surface depletion of Sb was observed towards the bottom of the NW due to longer exposure to As containing process gas. In GaAsSb inserts, increasing surface depletion of Sb was observed with increasing post-insert axial GaAs growth time, resulting from a combined effect of radial GaAs overgrowth and diffusion of Sb. The effect of growth temperature on the diffusion of Sb in the GaAsSb inserts was identified.

I. INTRODUCTION

Planar lattice-mismatched III-V semiconductor heterostructures are widely studied and applied for lasing, photodetector and energy applications[1]. Strain can however affect the growth control and functional properties of such heterostructures. Lately, III-V semiconductor nanowires (NWs) have gained a lot of attention as an alternative to planar semiconductors for similar applications[2]. NWs can overcome the challenges and limitations caused by the lattice mismatch due to strain relaxation at the free surfaces[3]. Furthermore, the demand for active material is reduced to less than one fifth of the material compared to a planar device with the same surface area[4].

One of the interesting III-V systems is zinc blende (ZB) $GaAs_{1-y}Sb_y$ due to its widely tunable bandgap (1.0 - 1.4 eV[5]) and the possibility for both type I and type II band alignment with GaAs[6]. Vapor-liquid-solid (VLS) growth of GaAsSb NWs and GaAs/GaAsSb heterostructured NWs by molecular beam epitaxy (MBE) using both Au-[7,8] and Ga-assisted[9,10] techniques have been demonstrated earlier. To obtain the desired band gap structure, the heterostructure should have an even, controllable composition and abrupt interfaces. In previous studies on axial $GaAs_{1-y}Sb_y$ inserts in GaAs NWs grown by MBE, concentration gradients axially towards the interfaces with GaAs as well as radially across the NW were observed[11,12]. The axial concentration gradients are related to a reservoir effect in the VLS growth process[13]. The radial concentration gradient was assumed to be caused by exchange between As and Sb at the NW surface during the axial growth after the insert, however this was not addressed in further detail. Early studies on MBE growth of planar GaAsSb demonstrate

a)Electronic mail: a.helvoort@ntnu.no

that GaAsSb surfaces easily become depleted from Sb under an As flux, especially at temperatures above 500°C[14–16]. As NWs have a high surface-to-volume ratio and the NW surface is exposed to As flux at high temperatures, this effect is expected to be very pronounced during the growth of GaAsSb NWs and heterostructured GaAs/GaAsSb NWs. A lower Sb content at the surface and an uneven radial Sb composition could affect the optical and electrical properties of the NWs.

The As-Sb exchange process at the NW surface will lead to diffusion and eventually surface depletion of Sb. Isothermal diffusion in semiconductors is primarily driven by a concentration gradient. Here diffusion of Sb out of a NW is considered. How the process is described depends on the extent of the crystal from which the diffusion takes place, and the extent of the reservoir into which Sb diffuses. Assuming a very large reservoir, i.e., an infinite sink for the out-diffusing Sb, a semi-infinite crystal and one-dimensional situation, the Sb concentration at a distance z from an Sb source with concentration C_0 is given by[17]

$$C(z,t) = C_0 erf\left(\frac{z}{2\sqrt{Dt}}\right), \qquad (1)$$

where t is the duration of the diffusion process. D is a temperature and material dependent diffusion coefficient, defined as[17]

$$D = D_0 \exp\left(-Q/k_B T\right), \qquad (2)$$

where D_0 is a temperature independent factor, Q is the activation energy for atomic jump mechanism, k_B is the Boltzmann constant and T is the temperature.

Here we have studied diffusion of Sb in Ga-assisted $GaAs_{1-y}Sb_y$ NWs and in axial $GaAs_{1-y}Sb_y$ inserts in both Ga- and Au-assisted GaAs NWs using quantitative high-angle annular dark field scanning transmission electron microscopy (HAADF STEM). HAADF STEM image intensity is dependent on the atomic number and specimen thickness, and quantitative HAADF STEM refers to quantification of zone-axis image intensities by comparison with simulated intensities[18,19]. The method has been successfully applied to compositional analysis of different planar heterostructured semiconductor systems[20–22]. Previously the method has also been applied to compositional characterisation of heterostructured NWs[11], and variations in HAADF STEM intensity profiles across the $GaAs_{1-y}Sb_y$ inserts were observed in this study. In the present work, a concentration profile across the $GaAs_{1-y}Sb_y$ NW segment was modelled from the basis of growth conditions and basic diffusion processes, taking into account the hexagonal NW shape. Using simulated HAADF STEM image intensities for different thicknesses and Sb concentrations, this concentration profile was applied to interpret the observed variations in experimental HAADF STEM intensity profiles across $GaAs_{1-y}Sb_y$ NWs and $GaAs_{1-y}Sb_y$ inserts.

II. MATERIALS AND METHODS

A. Nanowire growth

The NWs were grown with the vapor-liquid-solid (VLS) technique in a Varial Gen II Modular molecular beam epitaxy (MBE) system. Altogether five different NW samples were studied: one GaAsSb NW sample (batch A), three samples of Ga-assisted GaAs/GaAsSb NWs with a varying post-insert pure GaAs growth time (batches B-D), and one Au-assisted GaAs/GaAsSb NW sample (batch E). The samples and their growth details are described in Table I and illustrated schematically in Fig. 1(a). HAADF STEM image of a representative NW from each batch is shown in Fig. 1(b). The Ga-assisted NWs (batches A-D) were grown on Si(111) substrates and the Au-assisted NWs (batch E) on GaAs(111)B substrates. For batches B-D, the pure GaAs part below the insert has always ZB phase and above the insert wurtzite (WZ) phase. For batch E, the pure GaAs parts below and above the insert have both WZ phase. The growth direction was [111] for ZB GaAs(Sb) and [0001] for WZ GaAs. The Ga flux was the same for each batch and set to yield a growth rate of 0.7 monolay-

Table I. Growth details of the studied NW samples. For the widths (W) and insert lengths (L), the range observed among the studied NWs is presented.

Batch	T [°C]	Growth procedure	As flux [Torr]	Sb flux [Torr]	W insert/GaAs [nm]	L insert [nm]
A	640	40min GaAsSb	4.3×10^{-6}	1.2×10^{-6}	172-193	–
B	620	20min GaAs/1min GaAsSb	4.2×10^{-6}	1.1×10^{-6}	88-91/70-74	109-118
C	620	20min GaAs/1min GaAsSb/5min GaAs	4.2×10^{-6}	1.1×10^{-6}	92-111/91-108	126-147
D	620	20min GaAs/1min GaAsSb/15min GaAs	4.2×10^{-6}	1.1×10^{-6}	86-134/85-131	135-156
E	540	17min GaAs/30s GaAsSb/17min GaAs	6.0×10^{-6}	0.6×10^{-6}	58-65/58-65	23-64

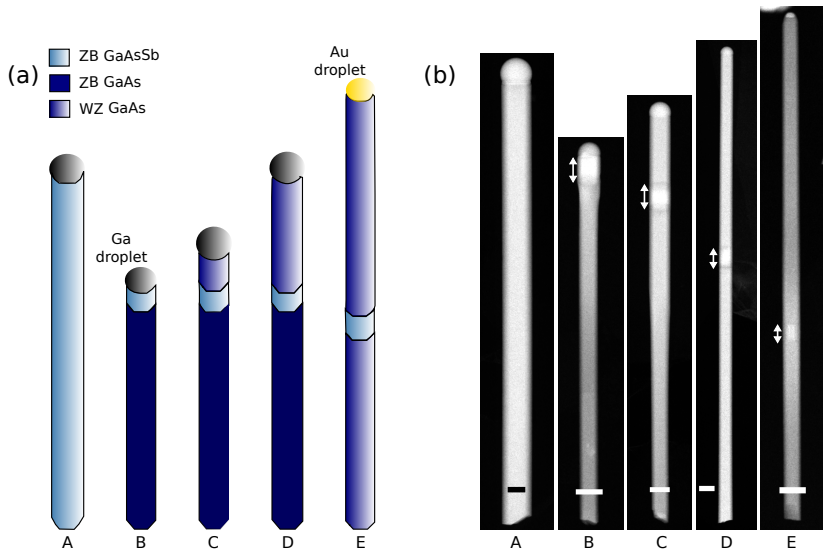

Figure 1. (a) Schematic NWs for the five different batches studied and (b) HAADF images of a representative NW from each batch. The scale bar is 100 nm in each image, and the double-headed arrows mark the inserts.

ers per second. From each batch at least three representative NWs were analysed with quantitative HAADF STEM and energy dispersive spectroscopy (EDX). For more detailed descriptions of the NW growth, see[10] (batches B-D) and[7] (batch E).

B. Microscopy

For the TEM studies, the NWs were scraped off the substrate with a diamond scraper, dispersed in isopropanol and transferred to a graphene-coated Cu-grid (Graphene Laboratories Inc.). The microscopy was performed on a JEOL 2010F operated at 200 kV ($C_s = 1$ mm). Images along the [110] axis for ZB GaAs(Sb)

([11$\bar{2}$0] for WZ GaAs) were recorded using a probe-forming aperture semi-angle of 8.4 mrad, a probe size of approximately 0.2 nm and a dwell time of 38.8 µs. The ADF detector covered an angular range from 29 to 114 mrad. Reference high-resolution (HR) TEM images were taken on a 2K Gatan UltraScan CCD camera. EDX point scans were performed off the [110] zone with a probe size of 1 nm for a live time of 120 to 180 s, using a Si drift detector (Oxford Instruments, solid angle 0.23 sr). The EDX data on the ZB GaAsSb inserts was quantified manually using the Cliff-Lorimer[23] method when a ZB GaAs reference area was available (batches B-D). Otherwise quantification by the EDX software (Oxford Instruments INCA) was used.

C. Image simulations and intensity normalization

HAADF STEM image simulations for WZ GaAs in the [0001] orientation and ZB $GaAs_{1-y}Sb_y$ in the [110] orientation for different Sb concentrations y were performed with the STEMsim software[24], based on the frozen-lattice multislice method. Static atomic displacements (SAD)[25] as well as the increase in the unit cell size and the Debye-Waller factor of Ga due to the change in composition were taken into account in the simulations. Using simulated intensities for different thicknesses and Sb concentrations y, a matrix for intensity as a function of concentration and thickness (CT-matrix) was constructed with cubic interpolation. In order to compare experimental and simulated image intensities, the experimental images were normalized to the incident beam intensity using a detector scan image according to Rosenauer et al.[19]. For more details on the simulations and intensity normalization, see[11].

The quantification can additionally be made more robust by comparing the experimental and simulated intensities relative to pure GaAs intensity (I/I_{GaAs}) instead of the absolute values[19,21,25]. This mitigates errors associated with for instance the measurement of thickness. In the present study this was possible for NWs with GaAsSb inserts (batches B-E), where a pure GaAs area was available in the same image. The reference GaAs intensity was taken from the central part of the NW, where thickness is constant. If there was a thickness difference between the insert and the pure GaAs segment, I_{GaAs} was extrapolated to a value corresponding to the thickness of the insert. The NW thickness was determined from the projected width in TEM images. For the simulated intensities, simulated I_{GaAs} at the respective thickness was used for calculating I/I_{GaAs}. Fig. 2 shows the simulated intensity as a function of Sb concentration and thickness relative to I_{GaAs}.

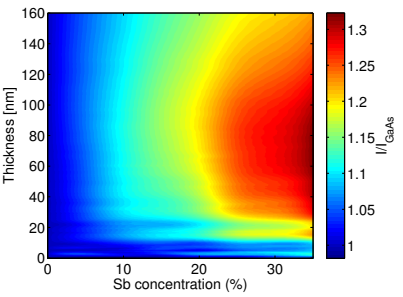

Figure 2. Simulated HAADF STEM intensity as a function of Sb concentration and thickness (CT-matrix) relative to the pure GaAs intensity (I_{GaAs}).

D. Modelled HAADF STEM intensity profiles considering diffusion

To study the radial Sb distribution, experimental HAADF intensity profiles taken across the NWs were compared with simulated profiles. For the pure WZ and ZB GaAs parts, the experimental intensity profile is nearly always in a good agreement with the simulated profile (see[11]), confirming that the thickness profile for the hexagonal NWs is modelled correctly and that the normalized experimental intensities correspond to the simulated intensities. In

the present study the cross-sectional intensity profile for pure GaAs was always verified for batches B-E.

For the GaAsSb segments, the experimental cross-sectional intensity profile often deviates from a simulated profile assuming a radially uniform Sb distribution[11,12]. Here the observed intensity profiles were modelled employing concentration profiles considering diffusion in the hexagonal NWs. First, based on the NW dimensions (Fig. 3(a)) and growth parameters, a profile for average concentration $\bar{C}(x,t)$ was obtained by integrating $C(z,t)$ (Eq. (1)) over the NW thickness for each position x across the NW. In figure 3(b), $C(z,t)$ is plotted for position $x = 0$, for different values of diffusion time, t. Diffusion takes place perpendicularly to the NW surface, however at the sides the surface is not perpendicular but at an angle of 30° with respect to the incident beam direction. Hence in these regions, the electron beam sees a slightly elongated diffusion profile. To take this into account, a geometrical correction factor of $\sin 30° = 1/2$ was included in Eq. (1) when integrating over these regions. Hence the average concentration $\bar{C}(x,t)$ for point x across the NW becomes

$$\begin{aligned}\bar{C}(x,t) =& \frac{1}{L\cos 30}\int_0^L C(z,t)dz \\ =& \frac{C_0}{L\cos 30}\left[\int_0^{z^*} erf\left(\frac{z}{2\sqrt{Dt}}\right)dz \right. \\ &\left. + \int_{z^*}^{L} erf\left(\frac{z}{4\sqrt{Dt}}\right)dz\right],\end{aligned} \quad (3)$$

where L is half of the NW width as indicated in Fig. 3(a). Since the NW is cylindrically symmetric, the average concentration calculated for the upper-right quarter represents the average intensity over the NW thickness at the right side, and the profile can be mirror-inverted to obtain the profile at the left side. From the basis of the resulting concentration profile $\bar{C}(x,t)$ and the known thickness profile of the NW, a modelled HAADF STEM intensity profile was constructed using the CT-matrix (Fig. 2). The maximum concentration C_0 was found by fitting the modelled intensity profile with the experimental profile at evenly thick the central part of the NW. Simulated intensity profiles assuming a homogeneous Sb distribution across the NW and an Sb concentration based on the experimental intensity at the central part of the NW not taking diffusion into account, are included in the plots for the cross-sectional intensity profiles for comparison.

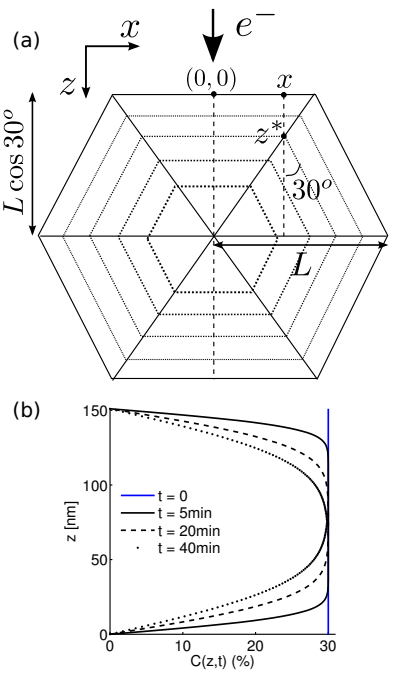

Figure 3. (a) Schematic of a hexagonal NW cross-section with the dimensions indicated (the dotted lines are contours of constant concentration) and (b) a plot for $C(z,t)$ (Eq. (1)), assuming $C_0 = 30\%$ and $T = 640°$C (corresponding to batch A), for different values of t.

Here, diffusion of Sb in GaAsSb is studied, assuming equal amount of outward diffusion of Sb and inward diffusion of As. Hence for the diffusion parameter D, an average value of the

self-diffusion parameters of As in GaAs and Sb in GaSb was used. Values of D_0 and Q employed for calculating D (Eq. (2)) for self-diffusion of Sb in GaSb are $D_0 = 3.4 \cdot 10^{18}$ $\mathrm{nm}^2/\mathrm{s}^{-1}$ and $Q = 3.45$ eV[26]. The respective values for As in GaAs are $D_0 = 7 \cdot 10^{13}$ $\mathrm{nm}^2/\mathrm{s}^{-1}$ and $Q = 3.2$ eV[26].

III. RESULTS AND DISCUSSION

A. GaAsSb nanowires

In GaAsSb NWs, an increasing Sb concentration towards the tip of the NW was observed by both quantitative HAADF STEM and EDX point analysis. The increase in concentration was strongest in the first two thirds of the NW, and flattened out in the upper part based on EDX point scans along the different NWs. As the growth conditions were not changed, it was suggested that this concentration gradient occurs due to out-diffusion of Sb during the NW growth.

Cross-sectional intensity profiles from the three areas indicated in Fig. 4(a) are presented in Figs. 4(b), (d) and (f). A trend for increasing deviation of the experimental profile (solid blue line) from the simulated profile assuming homogeneous Sb distribution (black dashed line) is observed when moving from the tip to the bottom of the NW: the region with even intensity at the central part of the experimental intensity profile becomes narrower towards the bottom of the NW. To each experimental intensity profile, a modelled intensity profile considering diffusion as explained in section II D is fitted (red dashed line). The corresponding profiles for average Sb concentration across the NW based on Eq. (3), employed in generating the modelled intensity profiles, are shown in Figs. 4(c), (e) and (g). Diffusion times t of 4, 20 and 40 min were assumed for the tip, middle and bottom part, respectively. These values were estimated considering the position along the NW and the total growth time, assuming an even growth rate. The modelled intensity profiles considering diffusion are in good agreement with the experimental profiles for the middle and the bottom parts. For the tip, the modelled intensity profile overestimates the experimental profile at the sides. A good agreement was obtained assuming $t = 10$ min, which suggests that further diffusion takes place after the NW growth. Right below the the droplet an experimental intensity profile agreeing with the simulated profile assuming homogeneous Sb distribution was obtained. The overall intensity was however lower in that region, indicating that this segment had grown after switching off the gas fluxes, fuelled by the droplet constituents.

Based on the HAADF STEM intensity at the central part, assuming a homogeneous Sb distribution throughout the NW, Sb concentrations of 23%, 21% and 19% were determined for tip, middle and bottom, respectively, as is indicated in Figs. 4(b), (d) and (f). By EDX, concentrations of 28%, 26% and 20% were measured, respectively. According to the diffusion model (Eq. (3)), however, a maximum concentration C_0 of 26% for the central part of the NW was estimated at each point – tip, middle and bottom – for the NW presented in Fig. 4, as is indicated in the plots. This was observed with other NWs from this batch as well. This suggests that Sb is only depleted from the surface, and the concentration in the NW centre remains unchanged. The Sb concentration values obtained with the different approaches including all the studied NWs are summarized in Table II.

The results indicate that diffusion of Sb towards the NW surface takes place during the growth, when the surface is exposed to the processing gases. Diffusion results in a varying cross-sectional Sb concentration profile, and consequently in a varying cross-sectional HAADF STEM intensity profile along the NW. The observed diffusion effect is probably the reason for the variation in Sb concentration along these NWs. The concentration variation could also be due to variation in growth rate or temperature during the growth, although we do not expect that these factors would induce such distinct variation as is observed here. The good agreement obtained between the modelled and experimental HAADF STEM intensity pro-

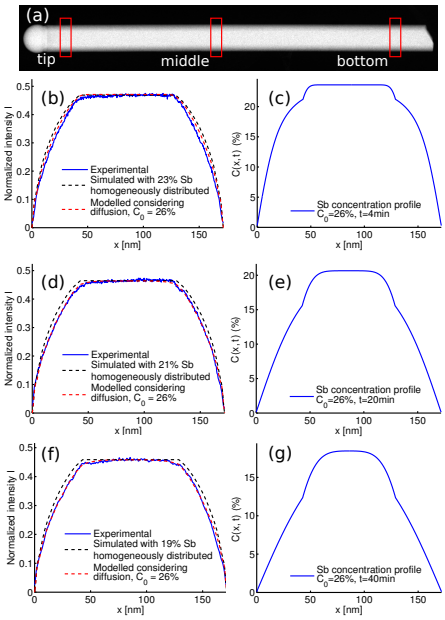

Figure 4. (a) HAADF STEM image of a GaAsSb NW (batch A) and experimental, simulated and modelled HAADF STEM intensity profiles across the NW at the different areas indicated in (a): (b) tip, (d) middle and (f) bottom. (c), (e) and (g) present the corresponding profiles for average Sb concentration, $\bar{C}(x,t)$, according to Eq. (3), employed in constructing the modelled intensity profiles (red dashed lines in (b), (d) and (f), respectively).

files in Fig. 4 supports the hypothesis that the concentration variation results from diffusion.

GaAsSb is intrinsically p-type due to Sb vacancies. If Sb diffuses out of the NW surface during the growth as the above results suggest, this might yield an increase in Sb vacancies, i.e., an increased hole density, and hence higher conductivity towards the bottom of the NW. The diffusion coefficient for Sb in GaSb is significantly higher than for As in GaAs (0.31 $\mathrm{nm}^2/\mathrm{s}^{-1}$ as opposed to $1.5 \cdot 10^{-4}$ $\mathrm{nm}^2/\mathrm{s}^{-1}$ at $T = 640°\mathrm{C}$); hence the outward diffusion of Sb is probably stronger than inward diffusion of As and not all the Sb vacancies are replaced by As. One way to reduce radial diffusion of Sb during the NW growth could be to use a lower growth temperature, as is used for instance in the growth of Au-assisted GaAsSb NWs[8].

B. Ga-assisted nanowires with inserts

When GaAs NWs with GaAsSb inserts are grown, the insert is exposed to As gas during the growth of the upper GaAs segment. Figs. 5(a), (b) and (d) present experimental, simulated and modelled cross-sectional intensity profiles for GaAsSb inserts in Ga-assisted GaAs NWs from batches B, C and D, respectively. The experimental intensity profiles were taken over ~ 5 nm wide regions approximately in the middle of the insert, where the Sb concentration was the highest. For batch B, with no GaAs segment grown after the insert, only a simulated intensity profile assuming a homogeneous Sb distribution is included (Fig. 5(a)). This profile fits the experimental intensity profile well, indicating that a homogeneous Sb distribution is present directly after the insert growth.

For batches C and D, the simulated intensity profiles assuming a homogeneous Sb distribution overestimate the experimental intensity profiles especially at the sides, where thickness is changing (Figs. 5(b) and (d)). This is particularly pronounced in the case of batch D, with the longer post-insert pure GaAs growth time. In this case it was however observed that diffusion according to Eq. (1) could not explain the observed cross-sectional HAADF STEM profiles at the inserts, but an overgrown GaAs layer is present as well. In this case, the primary sink for the out-diffusing Sb is the formed GaAs shell, which is finite. To be able to model the diffusion for this case, following assumptions were made: (i) GaAs shell is formed instantaneously on the insert after the insert growth, and (ii) at the formed core-shell interface, inward diffusion of As and outward diffusion of Sb are equal, such that the Sb concentration

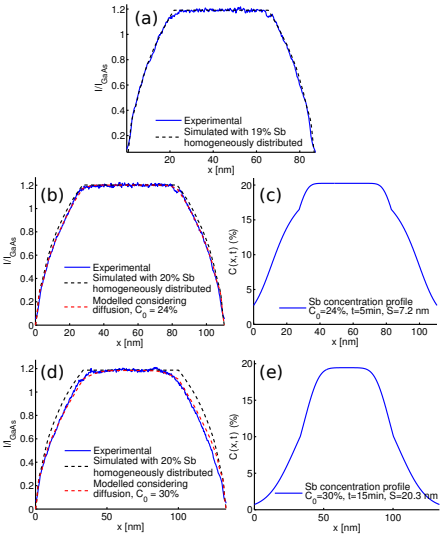

Figure 5. Experimental, simulated and modelled cross-sectional HAADF STEM intensity profiles at the insert for NWs from batch (a) B, (b) C and (d) D. Figures (c) and (e) present the corresponding profiles for average Sb concentration, $\bar{C}_{shell}(x,t)$, according to Eq. (5), employed in constructing the modelled intensity profiles (red dashed line) in figures (b) and (d), respectively.

at the interface is $1/2C_0$. Under these assumptions, the concentration at a distance z from an Sb source with concentration C_0 is

$$C_{shell}(z,t) = \frac{1}{2} C_0 erfc\left(-\frac{z}{2\sqrt{Dt}}\right). \quad (4)$$

In Fig. 6(b), $C_{shell}(z,t)$ is plotted for position $x = 0$, for different t and T corresponding to the values used in batches C-E. The average concentration for point x across the NW, $\bar{C}_{shell}(x,t)$, integrated over the NW thickness (see Fig. 6(a)), then becomes

$$\begin{aligned}\bar{C}_{shell}(x,t) =& \frac{1}{L\cos 30}\int_{-S}^{L-S} C_{shell}(z,t)dz \\ =& \frac{C_0}{2L\cos 30}\left[\int_{-S}^{z^*} erfc\left(-\frac{z}{2\sqrt{Dt}}\right)dz \right. \\ &\left. + \int_{z^*}^{L-S} erfc\left(-\frac{z}{4\sqrt{Dt}}\right)dz\right], \end{aligned} \quad (5)$$

where S is the thickness of the GaAs overgrowth as indicated in Fig. 6(a). In this case, both C_0 and S were varied to obtain a fit with the experimental HAADF STEM intensity profiles.

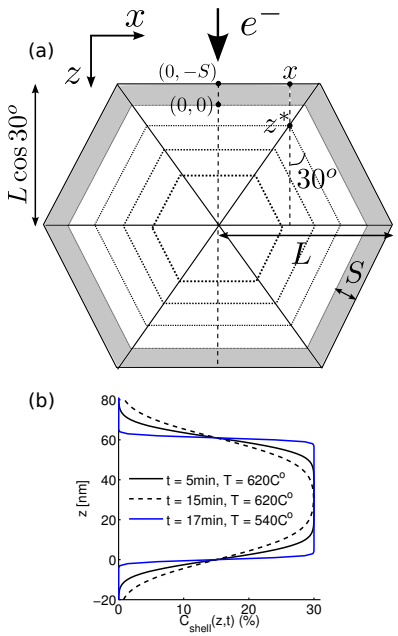

Figure 6. (a) Schematic of a hexagonal NW cross-section with GaAs overgrowth of thickness S, and (b) $C_{shell}(z,t)$ according to Eq. (4) assuming $C_0 = 30\%$ and $S = 20$ nm, for different t and T corresponding to the values used in batches C-E.

With intensity profiles modelled using concentration profiles based on Eq. (5) (red dashed line in Figs. 5(b) and (d)), good agreement with the experimental profiles is obtained. The corresponding profiles for average Sb concentration are presented in Figs. 5(c) and (e). In the case of the NW from batch D, a relatively thick shell ($S = 20.3$ nm) had to be included to model the experimental intensity profile, however this NW was a particularly thick one from this batch. From Figs. 5(c) and (e) it can further be seen, that because of redistribution of Sb by diffusion, there is no distinct GaAs shell, and the concentration profile is fairly smooth (see also Fig. 6(b)). Moreover, according to this model, Sb concentration is not 0 at the surfaces.

The Sb concentration based on quantitative HAADF STEM, assuming a homogeneous Sb distribution, was 19%, 20% and 20% for the NWs included in Fig. 5 from batch B, C, and D, respectively. With EDX, Sb concentrations of 24%, 36% and 35% were measured at the inserts for these three NWs, respectively. With the diffusion model, maximum concentrations C_0 of 24% and 30% were estimated for the NWs from batch C and D, respectively. The concentrations obtained with the different approaches considering all the studied NWs are summarized in table II. Since the inserts in batches B-D were grown under similar conditions, one would assume that the initial maximum Sb concentration, C_0, would be similar for these batches. The increase in Sb concentration from batch B to C can be explained with that when continuing the GaAs growth after insert, surplus Sb available in the Ga droplet gets incorporated to the insert[12]. From batch C to D however, there is no more Sb available to be incorporated to the insert. It might hence be that the diffusion model overestimates C_0 in the case of a high S. Furthermore, in batch D there was generally more variation in the NW dimensions and in the determined Sb concentrations than in batches C and B (see Tables I and II). This is probably related to the longer growth time employed in batch D.

We have additionally observed that annealing NWs with inserts under As-flux (4.2×10^{-6} Torr) leads to reduction of the NW diameter at the insert. This etching effect could happen parallel to the radial GaAs overgrowth in the present case. Once there is a GaAs barrier formed, the etching process stops and diffusion results in a redistribution of Sb to the overgrown GaAs layer. The GaAs overgrowth is formed at the beginning of the upper GaAs segment growth: the rate of radial overgrowth on the insert reduces once even thickness along the NW is established. Indeed, strong anti-tapering can be seen in the NW from batch B (Fig. 1(b)), and still some towards the bottom of the NW from batch C, whereas the NW from batch D has an even thickness along the whole NW.

Table II. Sb concentrations determined with the different approaches along the NW for batch A and at the middle of the insert for batches B-E (the number of NWs considered is given in parentheses).

Batch		Q. STEM, average	Q. STEM, C_0	EDX
A(3)	tip	23-31%	26-37%	20-28%
	middle	21-30%	26-37%	17-26%
	bottom	19-28%	26-37%	12-20%
B(3)		19-20%	–	24-37%
C(3)		20-22%	24-25%	28-36%
D(4)		20-22%	27-38%	18-35%
E(3)		6-14%	10-28%	2-14%

The observed variation in the radial concentration profile with post-insert GaAs growth implies for instance that it will be challenging to grow multiple GaAsSb inserts in GaAs NWs[10] with the same radial Sb concentration profiles and hence optoelectronic properties. Other, improved growth strategies for heterostructured GaAs/GaAsSb NWs are required if decrease in concentration towards the outer surfaces is to be avoided.

C. Au-assisted nanowires with inserts

Intensity profiles at the insert for three NWs from batch E are presented in Figs. 7(a), (c) and (e). The corresponding profiles for average Sb concentration based on Eq. (5) are

shown in Figs. 7(b), (d) and (f).[27] These NWs have average Sb concentrations of 6%, 14% and 13% based on quantitative STEM, assuming a homogeneous Sb distribution, and 2%, 12% and 14%, respectively, based on EDX. With the diffusion model, maximum Sb concentrations C_0 of 9%, 23% and 28% at the insert centre were estimated for the three NWs, respectively. The variation in Sb concentration among these NWs, despite the similar post-insert GaAs growth time, is related to variation in the Au seed particle size, resulting in a variation in growth rates and consequently in insert lengths[12] (see Table I). Furthermore, the experimental intensity profiles of these three NWs are very different. The experimental intensity profile in Fig. 7(a), for the NW with the lowest Sb concentration, is fairly similar to the simulated profile assuming a homogeneous Sb distribution. This is not the case for the experimental intensity profiles in Figs. 7(c) and (e), which display prominent variations.

As the growth temperature was substantially lower, with these NWs diffusion is less pronounced and a distinct GaAs shell is present in the average concentration profiles in Figs. 7(b), (d) and (f) (see also Fig. 6(b)). This is reflected in the intensity variations present in the experimental intensity profiles at the sides. The modelled intensity profiles reflect these variations and are in a surprisingly good agreement with the experimental profiles, especially for the NW in Fig. 7(e). This batch is hence a further proof for the presence of GaAs overgrowth, and a verification for that Eq. (4) describes the redistribution of Sb in these cases well. The thickness of the overgrowth, S, is fairly similar for the three NWs presented in Fig. 7, as is the width of these NWs. The slightly higher S employed for the NW in Fig. 7(e) might have resulted in an overestimation of C_0 in that particular case. On the other hand, thicker GaAs overgrowth could explain why the experimental intensity profile in Fig. 7(e) is so different from the profile in Fig. 7(c).

If the GaAsSb insert is constrained by a GaAs shell, this will induce strain to the insert. This is probably the reason to the strong intensity variations present at the evenly thick central region in the intensity profiles of Au-assisted NWs, in particular in the NWs presented in Figs. 7(c) and (e), with higher Sb concentrations. In addition, in Au-assisted growth the size of the Au particle is fixed and might hinder the expansion of the insert during its growth. In Ga-assisted growth, the Ga-particle can reshape[10] and the insert is able to expand to compensate for the increase in the lattice parameter with the increased Sb content. Furthermore, in Ga-assisted NWs the insert does not exhibit a clear core-shell structure due to the redistribution of Sb by diffusion as was discussed in the previous section. This can explain the absence of strain contrast, and accordingly the relatively smooth HAADF STEM intensity profiles in Figs. 5(a),

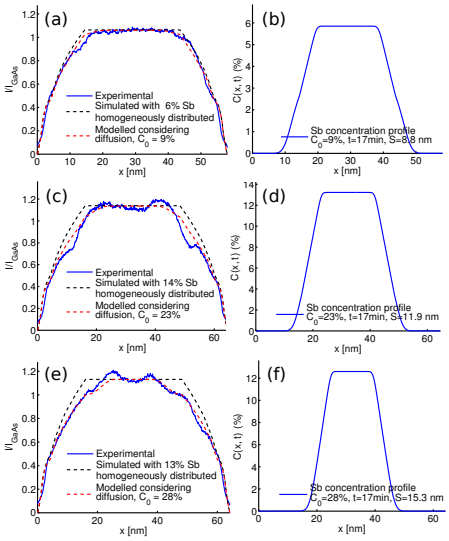

Figure 7. (a), (c) and (e): Experimental, simulated and modelled cross-sectional HAADF STEM intensity profiles at the insert for three NWs from batch E. (b), (d) and (f): The corresponding profiles for average Sb concentration, $\bar{C}_{shell}(x,t)$, according to Eq. (5), employed in constructing the modelled intensity profiles (red dashed line) in (a), (c) and (e), respectively.

(b) and (d), despite the higher apparent Sb concentration in the inserts of Ga-assisted NWs. Please note that strain could be an additional driving force for outward diffusion of Sb. This has not been taken into account in the present study.

If the NW insert has a surface layer depleted of Sb due to radial GaAs overgrowth and/or out-diffusion of Sb as the above analysis suggests, this will affect the optical properties of the NWs. With Au-assisted insert NWs in particular, a relatively high photoluminescence (PL) signal is generally obtained at the insert despite the absence of a passivating AlGaAs shell[7,12]. This could be explained with the presence of the relatively thick overgrown GaAs layer, which would similarly to AlGaAs passivate GaAsSb surface states due to the higher band gap of GaAs. This effect is probably smaller in Ga-assisted NWs as upon further post-insert GaAs growth the GaAs layer and its passivating effects are reduced due to diffusion of Sb into the overgrown GaAs layer. On the other hand thick GaAs overgrowth as observed with the Au-assisted insert NWs will make electrical contacting of the GaAsSb insert more challenging.

D. The effect of the Sb depleted layer on the concentration determination

In the present study, an average Sb concentration in $GaAs_{1-y}Sb_y$ NWs and $GaAs_{1-y}Sb_y$ inserts was determined from the basis of HAADF STEM intensities, assuming a homogeneous Sb distribution throughout the NW. The maximum concentration C_0 in the NW centre was estimated assuming a concentration profile across the NW based on Eqs. (3) (GaAsSb NWs) and (5) (inserts). It is however not clear how well the estimated C_0 corresponds to the actual Sb concentration in the NW centre, and how does the variation in concentration in the electron beam direction affect the HAADF STEM intensity quantification, and accordingly the determination of the average Sb concentration.

To study these concerns, initial simulations were carried out, employing a concentration profile considering diffusion in the incident beam direction with values for C_0 of 28% and 30% in the centre. The simulated HAADF STEM intensities as a function of thickness were relatively similar with the intensities for a homogeneous Sb concentration of 21% across the thickness. According to these results the average Sb concentration based on quantitative HAADF STEM, assuming a homogeneous Sb distribution, is 0.25-0.30 times lower than the maximum value in the centre. In this initial simulation however, no overgrown shell was considered. Furthermore, the standard deviation for the average simulated intensities was high, despite the high number of iterations (over 30 for each compositional configuration). Hence the results should be treated with caution, and a more detailed study is needed considering the different cases predicted by the diffusion models presented here. Experimentally, for batch B-D it was observed that the average Sb concentration based on quantitative HAADF STEM was similar for all the studied NWs, independent of the presence of depletion of Sb at the surface. On the other hand the value for the estimated C_0 varied a lot, especially for batches D and E.

As a reference, EDX point spectra were acquired for all the studied NWs. For Ga-assisted NWs with inserts (batches B-D), the values based on EDX generally exceeded the average Sb concentration values based on quantitative HAADF STEM (assuming a homogeneous Sb distribution), which are as above stated likely underestimated. This deviation was present also for NWs from batch B, which should not have a surface layer depleted of Sb. For the Au-assisted NWs presented here with the higher Sb concentration (Figs. 7(c) and (e)), the average Sb concentration values based on quantitative HAADF STEM and EDX were similar, despite the thick overgrown GaAs shell. In a previous study on the same system[12], concentrations determined by quantitative HAADF STEM, EDX and photoluminescence (PL) were in agreement for Sb concentrations in the same range (10-16%). However, for higher average Sb concentrations (>16% as determined by EDX), similar

deviation was observed as in the present study with Ga-assisted GaAs/GaAsSb NWs.

For some individual NWs, such as the batch D NW presented in section III B, the concentration determined by EDX was relatively well in agreement with the C_0 based on the diffusion model. The variation in the concentration values obtained with EDX was however very large (see Table II). Measuring the same GaAsSb insert of a NW from batch C gave values for the Sb concentration varying from 13 up to 28% when orientation relative to the electron beam or to the EDX detector was altered. EDX quantification is based on the assumption of a homogeneous composition within the excited area and a planar geometry, and NWs are hence not an ideal system to be studied by EDX. Furthermore, for a compound system as GaAs, orientation dependent absorption will also affect the EDX result, especially at orientations close to [110] zone axis[29].

In addition to the large variations in the measured Sb concentration, with EDX it is not possible to detect small changes in radial Sb distribution as was done here with quantitative HAADF STEM. Especially at the sides of the NWs, the variation in thickness dominates the EDX signal, and variations in composition cannot be detected. We therefore conclude that quantitative HAADF STEM is superior to EDX, when high sensitivity and high spatial resolution are required. Refinements in the HAADF STEM image simulations are however needed to better understand the effect of a varying Sb concentration profile in the beam direction into the concentration determination.

IV. CONCLUSIONS

Using a detailed quantitative analysis of HAADF STEM image intensities considering diffusion mechanisms, this study has shown that an uneven radial Sb distribution develops during the growth of GaAsSb NWs and GaAsSb inserts within GaAs NWs. The NW surface becomes depleted of Sb due to As-Sb exchange at and Sb diffusion towards the NW surface. In Ga-assisted GaAsSb NWs, increasing surface depletion of Sb was observed towards the bottom of the NW due to longer exposure to As containing process gas. In Ga-assisted NWs with GaAsSb inserts, increasing surface depletion was observed with increased post-insert pure GaAs growth time.

At the GaAsSb inserts, radial overgrowth of GaAs was identified in addition to diffusion of Sb. In Ga-assisted NWs, diffusion resulted in redistribution of Sb to the GaAs overgrowth and a smooth concentration profile across the insert. In Au-assisted NWs, grown at a lower temperature, the contribution of diffusion was small and the concentration profile across the insert displayed an abrupt transition from the GaAsSb core-region to the GaAs overgrowth.

The radial Sb concentration variations cause a radial variation in the band gap, thereby affecting the optoelectronic properties of these NWs. These variations should hence be considered in further growth optimisation of GaAsSb NWs and GaAs NWs with GaAsSb inserts.

ACKNOWLEDGEMENTS

This work was supported by the Faculty of Natural Sciences and Technology at NTNU and the "RENERGI" program of the Research Council of Norway under grant no. 190871.

REFERENCES

[1] Z. Alferov, Semiconductors **32**, 1 (1998).
[2] P. Yang, R. Yan, and M. Fardy, Nano Lett. **10**, 1529 (2010).
[3] K. L. Kavanagh, Semiconductor Sci. Tech. **25**, 024006 (2010).
[4] P. Hiralal, H. E. Unalan, and G. A. J. Amaratunga, Nanotechnology **23**, 194002 (2012).
[5] I. Vurgaftman, J. R. Meyer, and L. R. Ram-Mohan, J. Appl. Phys. **89**, 5815 (2001).
[6] J.-B. Wang, S. R. Johnson, S. A. Chaparro, D. Ding, Y. Cao, Y. G. Sadofyev, Y.-H. Zhang, J. A. Gupta, and C. Z. Guo, Phys. Rev. B **70**, 195339 (2004).
[7] D. L. Dheeraj, G. Patriarche, H. Zhou, T. B. Hoang, A. F. Moses, S. Grønsberg, A. T. J. van Helvoort, B.-O. Fimland, and H. Weman, Nano Lett. **8**, 4459 (2008).

[8]D. L. Dheeraj, G. Patriarche, L. Largeau, H. L. Zhou, A. T. J. van Helvoort, F. Glas, J. C. Harmand, B. O. Fimland, and H. Weman, Nanotechnology **19**, 275605 (2008).
[9]S. Plissard, K. A. Dick, X. Wallart, and P. Caroff, Appl. Phys. Lett. **96**, 121901 (2010).
[10]A. M. Munshi, D. L. Dheeraj, J. Todorovic, A. T. J. van Helvoort, H. Weman, and B. O. Fimland, J. Cryst. Growth **372**, 163 (2013).
[11]H. Kauko, T. Grieb, R. Bjørge, M. Schowalter, A. M. Munshi, H. Weman, A. Rosenauer, and A. T. J. van Helvoort, Micron **44**, 254 (2013).
[12]J. Todorovic, H. Kauko, L. Ahtapodov, A. F. Moses, P. Olk, D. L. Dheeraj, B. O. Fimland, H. Weman, and A. T. J. van Helvoort, Semiconductor Sci. Tech.(2013), accepted.
[13]K. A. Dick, J. Bolinsson, B. M. Borg, and J. Johansson, Nano Lett. **12**, 3200 (2012).
[14]M. Yano, M. Ashida, A. Kawaguchi, Y. Iwai, and M. Inoue, J. Vac. Sci. and Tech. B **7**, 199 (1989).
[15]M. Yano, H. Yokose, Y. Iwai, and M. Inoue, J. Cryst. Growth **111**, 609 (1991).
[16]R. Kaspi and K. R. Evans, J. Cryst. Growth **175-176**, 838 (1997).
[17]D. Shaw, "Atomic Diffusion in Semconductors," (Plenum Press, 1973) Chap. General Features of Diffusion in Semiconductors.
[18]J. M. LeBeau and S. Stemmer, Ultramicroscopy **108**, 1653 (2008).
[19]A. Rosenauer, K. Gries, K. Müller, A. Pretorius, M. Schowalter, A. Avramescu, K. Engl, and S. Lutgen, Ultramicroscopy **109**, 1171 (2009).
[20]A. Rosenauer, T. Mehrtens, K. Müller, K. Gries, M. Schowalter, P. V. Satyam, S. Bley, C. Tessarek, D. Hommel, K. Sebald, M. Seyfried, J. Gutowski, A. Avramescu, K. Engl, and S. Lutgen, Ultramicroscopy **111**, 1316 (2011).
[21]M. Herrera, Q. M. Ramasse, D. G. Morgan, D. Gonzalez, J. Pizarro, A. Yáñez, P. Galindo, R. Garcia, M.-H. Du, S. B. Zhang, M. Hopkinson, and N. D. Browning, Phys. Rev. B **80**, 125211 (2009).
[22]E. Carlino and V. Grillo, Phys. Rev. B **71** (2005).
[23]G. Cliff and G. W. Lorimer, J. Microsc. **103**, 203 (1975).
[24]A. Rosenauer and M. Schowalter, "STEMSIM – A New Software Tool for Simulation of STEM HAADF Z-Contrast Imaging," in *Microscopy of Semiconducting Materials 2007* (2008).
[25]V. Grillo, E. Carlino, and F. Glas, Phys. Rev. B **77**, 054103 (2008).
[26]J. H C. Casey, "Atomic Diffusion in Semconductors," (Plenum Press, 1973) Chap. Diffusion in the III-V Compound Semiconductors.
[27]The graphs in Figs. 7(a) and (e) were presented also in[12], but without the simulated profiles considering diffusion.
[28]L. Ahtapodov, J. Todorovic, P. Olk, T. Mjåland, P. Slåttnes, D. L. Dheeraj, A. T. J. van Helvoort, B. O. Fimland, and H. Weman, Nano Lett. **12**, 6090 (2012).
[29]M. DeGraef, *Introduction to Conventional Transmission Electron Microscopy* (Cambridge University Press, 2003).

Paper IV

Compositional analysis of GaAs/AlGaAs heterostructures using quantitative scanning transmission electron microscopy

H. Kauko, C. L. Zheng, Y. Zhu, S. Glanvill, C. Dwyer, A. M. Munshi, B. O. Fimland, A. T. J. van Helvoort and J. Etheridge

Accepted for publication in *Applied Physics Letters*.

Compositional analysis of GaAs/AlGaAs heterostructures using quantitative scanning transmission electron microscopy

H. Kauko,[1] C. L. Zheng,[2] Y. Zhu,[2,3] S. Glanvill,[2] C. Dwyer,[2,4] A. M. Munshi,[5] B. O. Fimland,[5] A. T. J. van Helvoort,[1] and J. Etheridge[2,3,a)]

[1)] *Department of Physics, Norwegian University of Science and Technology (NTNU), Trondheim, Norway*

[2)] *Monash Centre for Electron Microscopy, Monash University, VIC 3800, Australia*

[3)] *Department of Materials Engineering, Monash University, VIC 3800, Australia*

[4)] *Ernst Ruska-Centre for Microscopy and Spectroscopy with Electrons, and Peter Grünberg Institute, Forschungszentrum Jülich, D-52425 Jülich, Germany*

[5)] *Department of Electronics and Telecommunications, Norwegian University of Science and Technology (NTNU), Trondheim, Norway*

(Dated: November 19, 2013)

We demonstrate a method for compositional mapping of $Al_xGa_{1-x}As$ heterostructures with high accuracy and unit cell spatial resolution using quantitative high angle annular dark field scanning transmission electron microscopy (HAADF STEM). The method is low dose relative to spectroscopic methods, and insensitive to the effective source size and higher order lens aberrations. We apply the method to study the spatial variation in Al concentration in cross-sectioned GaAs/AlGaAs core-shell nanowires and quantify the concentration in the Al-rich radial band and the AlGaAs shell segments.

GaAs/AlGaAs heterostructures in quantum wells and more recently in nanowires (NWs) are technologically important for optoelectronic applications, such as high-frequency lasers[1] and efficient light emitting diodes[2]. Compositional variations in the AlGaAs barrier or at the interfaces within the heterostructures will modify the band gap and carrier concentration and thereby affect the optical properties of these heterostructures[3–6]. Hence accurate methods for characterizing the composition with high spatial resolution are needed. Aberration corrected high-angle annular dark field scanning transmission electron microscopy (HAADF STEM) can image nanostructures down to the atomic scale with the image intensity sensitive to the atomic number and specimen thickness[7,8]. With appropriate characterization of the incident electron wave field and the ADF detector response and angular range, the measured HAADF STEM image intensities can be compared quantitatively, on an absolute scale, with simulated intensities[9–12]. If all relevant experimental parameters are measured and included in the simulations, quantitative information such as the sample thickness[9,12] and chemical composition[10,13,14] can be extracted in simple circumstances. This provides an alternative approach to energy dispersive X-ray (EDX) or electron energy loss spectroscopy (EELS) mapping for compositional analysis. The approach offers a high spatial resolution with a lower radiation dose and potentially higher sensitivity and accuracy. For a given spatial resolution, the dwell time and hence radiation dose, is at least two orders of magnitude less than for an EELS or EDX chemical map. Furthermore, in EELS low energy edges, such as Al $L_{2,3}$, are dominated by background signal and hence difficult to detect and quantify. In EDX, the effective resolution can be limited by the large sampled volume.

Here we demonstrate a method for compositional analysis of $Al_xGa_{1-x}As$ by quantitative HAADF STEM and apply it to complex core-shell NW heterostructures. The negligible strain, which might otherwise affect the HAADF STEM intensity[15,16], and the relatively large difference in the atomic number between Ga and Al, render GaAs/AlGaAs particularly amenable to compositional analysis by quantitative HAADF STEM. Nevertheless, a compositional analysis of the AlGaAs system from ADF STEM images has only been attempted once[13]. Since this pioneering study, there have been significant advances in STEM electron-optics[17,18], as well as in the methods for quantitative analysis of STEM images[9–12,19–21]. GaAs/AlGaAs core-shell structured NWs and the peculiar compositional variations in the AlGaAs shell have received wide attention lately[5,22–24]. In those studies, the compositional characterisation was based on qualitative interpretation of HAADF STEM images and EDX. The present study demonstrates that quantitative HAADF STEM can give higher resolution compositional information in AlGaAs than obtained previously.

The GaAs NWs were grown with the vapour-liquid-solid (VLS) growth mechanism on a Si(111) substrate using Ga-assisted molecular beam epitaxy (MBE). The growth direction for zinc blende (ZB) GaAs was ⟨111⟩, the growth time 35 min and the growth temperature 620°C[25]. Core growth was terminated by stopping the Ga flux and consuming the Ga droplet by As flux. Subsequently, the AlGaAs shell was grown by vapour-solid (VS) mechanism on the {110} core facets for 30 min at a temperature of 460°C. The nominal Al content was 50% based on planar growth calibration. Lastly, a GaAs cap was grown on the shell facets by VS growth for 20 min to prevent oxidation of the AlGaAs shell. The cross-

a)Electronic mail: joanne.etheridge@monash.edu

sectional TEM specimens were prepared by embedding NWs on the substrate into epoxy resin and microtoming thin slices perpendicular to the NW growth direction[26] (Fig. 1(a)). TEM characterization of entire NWs showed that these NWs have a high density of stacking faults and twin planes in the upper third of the NWs, and few crystal defects in the bottom two thirds of the NW. We assume that the cross-section studied here (Fig. 1(b)) is from the bottom two thirds. For high-resolution HAADF STEM characterization, the specimens were investigated with a FEI Titan^3 80-300 Schottky field emission gun transmission electron microscope fitted with both probe and image aberration correctors (CEOS GmbH) and operated at 300 kV. The probe convergence semi-angle was set to 16.2 mrad (100 µm condenser lens aperture) with spot size number 9. A Fischione Instruments 3000 ADF detector spanning an angular range from 46 mrad to approximately 200 mrad was used. For low magnification TEM characterisation and EDX, the sample was studied with a JEOL 2010F operated at 200 kV (C_s = 1 mm, probe size ~1 nm), equipped with a Si drift detector for EDX (Oxford Instruments, solid angle 0.23 srad).

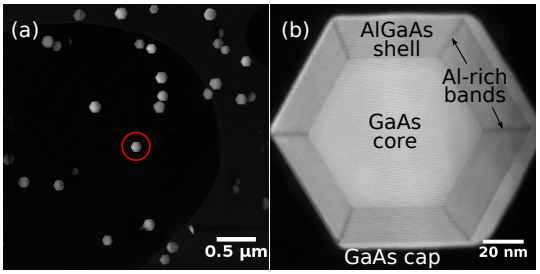

Figure 1. (a) Low-magnification HAADF STEM image of several NW cross-sections and (b) a close-up image of the cross-section encircled in (a) perpendicular to the ⟨111⟩ growth direction, showing the light GaAs core and cap, the AlGaAs shells (darker) plus the radial Al-rich bands (dark) parallel to the ⟨112⟩ directions. (The drop in intensity in the right hand region is due to change in local crystal tilt.)

In order to extract quantitative chemical information, the recorded experimental HAADF STEM images were compared with the simulated images using a GPU-enhanced frozen-phonon multislice code which includes multiple elastic scattering and multiple thermal diffuse scattering assuming the Einstein model[27]. The experimental images are put on an absolute scale by normalizing the image intensity against the total incident beam intensity according to $I_{norm} = (I_{raw} - I_{dark})/(I_{det} - I_{dark})$, where I_{norm} is the normalized image intensity, I_{raw} the raw image intensity, I_{dark} the dark current of the detector, and I_{det} is the average detector response towards the total incident beam intensity[28]. I_{det} is determined by scanning the incident beam over the whole detector in real space in the absence of a specimen[12,28,29]. In order to avoid saturating and potential damage to the detector during the scan, a smaller condenser lens aperture (30 µm) was used to form a relatively low intensity beam, but keeping the gain and offset settings the same. The intensity difference between the two probes applied for imaging and detector scan, formed with different condenser lens aperture sizes, was calibrated with a CCD camera, and taken into account in the image normalization. Care was taken to distinguish the active area of the detector from the physical size of the annulus and to calibrate each accordingly.

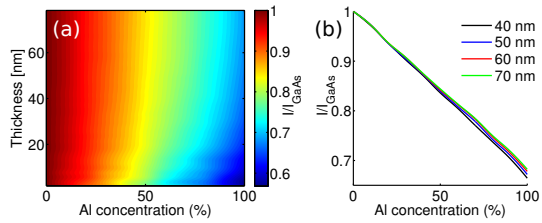

Figure 2. (a) Simulated HAADF STEM intensity normalized to the GaAs intensity (I/I_{GaAs}) as a function of thickness and Al concentration and (b) I/I_{GaAs} as a function of Al concentration for different thicknesses.

The image simulations for ZB $Al_xGa_{1-x}As$ in [111] orientation were performed with a supercell of 27.7×32.0 Å (2×4 unit cells) sampled in an array of 1024×1024 pixels. This gave a maximum scattering angle of 210 mrad for 300 keV electrons considering symmetrical bandwidth limiting. Image intensities were calculated for Al concentrations x from 0 to 100 % with a step of 10 %, up to a thickness of 80 nm with a step of 2 nm. The slight change in the unit cell size and the Debye-Waller factor of As due to the change in composition were taken into account using linear interpolation. Using simulated intensities averaged over the supercell for different thicknesses and Al concentrations, a matrix for intensity as a function of thickness and Al concentration (CT matrix, Fig. 2(a)) was constructed with cubic interpolation. The simulated and normalized experimental intensities were compared using the intensity ratio I/I_{GaAs}, where I is the intensity of AlGaAs and I_{GaAs} is the intensity of pure GaAs at the same thickness. This mitigates errors associated with the measurement of thickness and not taking into account the angular dependence of the detector response[30]. For the normalized experimental images, I_{GaAs} was taken from the nearby GaAs core region. The specimen thickness (75 nm) was also determined from the experimental I_{GaAs} by comparison with simulated intensities. From the simulated data in Fig. 2(a) it can be seen that I/I_{GaAs} is almost constant as a function of thickness for a given Al concentration for thicknesses above 30 nm. In Fig. 2(b) the simulated I/I_{GaAs} is plotted as a function of Al concentration for different thicknesses, demonstrating that I/I_{GaAs} decreases linearly as a function of Al concentration in the relevant thickness range. The simulations hence confirm that the GaAs/AlGaAs system is

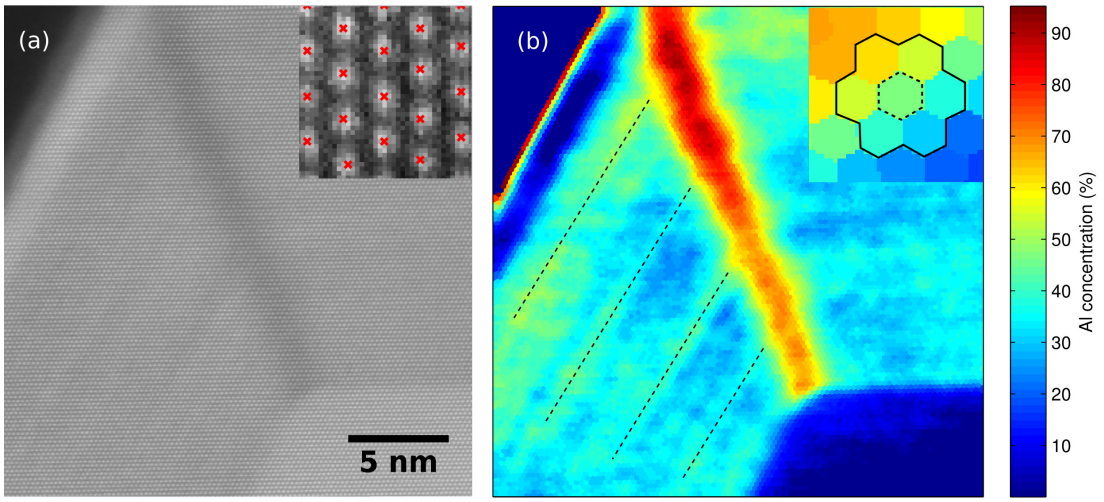

Figure 3. (a) High-resolution HAADF STEM image of the upper left corner of the cross-section in Fig. 1(b). The inset shows a small magnified region, with the atomic column positions located. (b) The corresponding Al composition map. The black dashed lines in the AlGaAs shell mark the Al-rich lines parallel to the {110} planes. In the inset, taken from the start of the Al-rich band near the core, the unit cell region employed for averaging the intensity is depicted.

well-suited for quantitative HAADF STEM analysis.

For the present case, the relevant variations in Al concentration are on the nanometer scale rather than atomic scale, thus we choose to do the compositional analysis at unit cell resolution. At unit cell resolution, the effective source size and higher order lens aberrations do not have to be considered[31]. This decreases the number of parameters to be measured and incorporated in the simulations and thereby avoids the errors associated with the measurement of these parameters. Furthermore, for the range of specimen thicknesses considered here, the intensity at an atomic column position will have contributions from the neighbouring atomic columns as well due to dynamical scattering of the electron probe[32–34]. This means that, for specimens such as these which are compositionally inhomogeneous, atomic resolution images or spectroscopic maps cannot necessarily provide compositional information with atomic spatial resolution. The experimental images were analysed as follows. First, the atomic column positions were located with normalized cross-correlation, using a Gaussian kernel with a standard deviation of 0.2 Å. With cross-correlation the position of the peak of the Gaussian is located rather than the pixel with local maximum intensity, giving a more accurate estimation of the actual atomic column position (see the inset in Fig. 3(a)). The positions of the six nearest neighbours were additionally located for each position. Subsequently, each pixel in the image was allocated to its nearest atomic column position[10]. This yields an image divided into hexagonal-like regions, so-called Voronoi polygons, centered at the atomic column positions. The intensity for each Voronoi polygon was calculated as the average over the central polygon and its six neighbouring polygons, as is depicted in the inset in Fig. 3(b). This effectively performs mean filtering for the image, but on an extended unit cell basis instead of using a square kernel. At each step it was ensured that the image processing did not alter the average image intensity. Finally, an Al concentration was determined for each polygon by comparing its intensity with the simulated intensities in the normalized CT matrix (Fig. 2(a)).

Fig. 3(a) presents a high-resolution HAADF STEM image from the upper left corner of the cross-section presented in Fig. 1(b). This region was chosen for its even thickness and orientation across the field of view. The image shows a dark band parallel to the ⟨112⟩ direction in the AlGaAs shell. Based on the lower HAADF STEM intensity, it can be deduced that this band is rich in Al, as was confirmed by EDX here and in earlier studies[5,22–24]. Fig. 3(b) presents a compositional map obtained from Fig. 3(a) using the quantitative intensity analysis described above. This map shows compositional information that cannot be determined from the original HAADF STEM image without such analysis. Firstly, the Al concentration in the Al-rich band increases from $66 \pm 3\%$ to $89 \pm 3\%$ towards the outer surface (the errors are standard deviations for the Al concentration at $\sim 1 \times 1$ nm regions). The width of the band (defined as the region where the Al concentration exceeds 60%) increases from ~ 1.3 nm near the core to ~ 2.5 nm near the GaAs cap. Secondly, in the AlGaAs shell segments the Al concentration increases also away from the core, from $36 \pm 3\%$ to $46 \pm 3\%$. In addition, on both sides of the Al-rich band, regions with lower Al concentration ($28 \pm 2\%$) are

present. This is reasonable as Al is accumulated in the Al-rich bands[5,24]. EDX measurements with lower spatial resolution on several similar cross-sections indicated an average Al concentration of $64 \pm 8\%$ in the Al-rich bands and $42 \pm 5\%$ in the shell segments. The value for the Al-rich band is similar to the values reported by others[5,22], however lower than the value obtained with quantitative HAADF STEM. We attribute this deviation to imprecise probe positioning and poorer spatial resolution of EDX, causing sampling of the nearby AlGaAs shell with a lower Al content. Finally, in the AlGaAs shell segments, variations in the Al concentration of lamellae parallel to the {110} planes are present. This kind of quasi-periodic concentration fluctuations in the AlGaAs shell were present in almost all the cross-sections studied, and were also observed by Rudolph et al[22]. Similar fluctuations have been reported previously in planar MBE growth of (110) AlGaAs[35]. The periodicity of the main Al-rich lines (black dashed lines in Fig. 3(b)) is ~ 3 nm as measured from the compositional map. Similar periodicities were measured in other NW cross-sections. These lines are less clear on the right side of the Al-rich band, which might be related to the fact that here the lines are parallel to the scanning direction of the electron beam.

To summarize, we have demonstrated a method for high-resolution compositional analysis of GaAs/AlGaAs heterostructures by quantitative HAADF STEM, and applied the method to analyze a cross-sectioned GaAs/AlGaAs core-shell NW specimen. The method mapped in detail compositional variations in Al across the NW cross-section at a unit cell resolution. The local composition of the narrow Al-rich radial bands was revealed and it was shown that the Al concentration increases along the band as well as in the AlGaAs shell in a direction away from the core. Al-rich lamellae occurring at ~ 3 nm intervals parallel to the {110} planes were also detected. Identifying Al-variations in detail is important for optimizing the optical properties of GaAs/AlGaAs core-shell NWs. This study shows that quantitative HAADF STEM is an effective method for high-resolution compositional analysis of GaAs/AlGaAs heterostructures, providing an alternative to spectroscopic methods in TEM.

Support is acknowledged from the Norwegian PhD Network on Nanotechnology for Microsystems (HK), the Australian Research Council grants DP110104734 (CD and JE) and LE0454166 (JE) and the "RENERGI" program of the Research Council of Norway grant 190871 (AMM and BOF).

REFERENCES

[1] R. Kohler, A. Tredicucci, F. Beltram, H. E. Beere, E. H. Linfield, A. G. Davies, D. A. Ritchie, R. C. Iotti, and F. Rossi, Nature **417**, 156 (2002).
[2] K. Tomioka, J. Motohisa, S. Hara, K. Hiruma, and T. Fukui, Nano Lett. **10**, 1639 (2010).
[3] M. Ramsteiner, R. Hey, R. Klann, U. Jahn, I. Gorbunova, and K. H. Ploog, Phys. Rev. B **55**, 5239 (1997).
[4] J. Noborisaka, J. Motohisa, S. Hara, and T. Fukui, Appl. Phys. Lett. **87**, 093109 (2005).
[5] M. Heiss, Y. Fontana, A. Gustafsson, G. Wüst, C. Magen, D. D. O'Regan, J. W. Luo, B. Ketterer, S. Conesa-Boj, A. V. Kuhlmann et al., Nat. Mater. **12**, 1476 (2013).
[6] M. Hocevar, T. Giang, L. Thuy, R. Songmuang, M. den Hertog, L. Besombes, J. Bleuse, Y.-M. Niquet, and N. T. Pelekanos, Appl. Phys. Lett. **102**, 191103 (2013).
[7] S. J. Pennycook and D. E. Jesson, Ultramic. **37**, 14 (1991).
[8] P. D. Nellist and S. J. Pennycook, Ultramic. **78**, 111 (1999).
[9] J. M. LeBeau, S. D. Findlay, L. J. Allen, and S. Stemmer, Nano Lett. **10**, 4405 (2010).
[10] A. Rosenauer, T. Mehrtens, K. Müller, K. Gries, M. Schowalter, P. V. Satyam, S. Bley, C. Tessarek, D. Hommel, K. Sebald et al., Ultramic. **111**, 1316 (2011).
[11] C. Dwyer, C. Maunders, C. L. Zheng, M. Weyland, P. C. Tiemeijer, and J. Etheridge, Appl. Phys. Lett. **100**, 191915 (2012).
[12] H. Katz-Boon, C. J. Rossouw, C. Dwyer, and J. Etheridge, Ultramic. **124**, 61 (2013).
[13] S. Anderson, C. Birkeland, G. Anstis, and D. Cockayne, Ultramic. **69**, 83 (1997).
[14] R. Bjørge, C. Dwyer, M. Weyland, P. Nakashima, C. Marioara, S. Andersen, J. Etheridge, and R. Holmestad, Acta Mater. **60**, 3239 (2012).
[15] Z. H. Yu, D. A. Muller, and J. Silcox, J. Appl. Phys. **95**, 3362 (2004).
[16] T. Grieb, K. Müller, R. Fritz, M. Schowalter, N. Neugebohrn, N. Knaub, K. Volz, and A. Rosenauer, Ultramic. **117**, 15 (2012).
[17] M. Haider, P. Hartel, H. Müller, S. Uhlemann, and J. Zach, Microsc. Microanal. **16**, 393 (2010).
[18] O. L. Krivanek, M. F. Chisholm, V. Nicolosi, T. J. Pennycook, G. J. Corbin, N. Dellby, M. F. Murfitt, C. S. Own, Z. S. Szilagyi, M. P. Oxley et al., Nature **464**, 571 (2010).
[19] J. M. LeBeau, S. D. Findlay, L. J. Allen, and S. Stemmer, Phys. Rev. Lett. **100** (2008).
[20] C. Dwyer, R. Erni, and J. Etheridge, Ultramic. **110**, 952 (2010).
[21] S. van Aert, K. J. Batenburg, M. D. Rossell, R. Erni, and G. van Tendeloo, Nature **470**, 374 (2011).
[22] D. Rudolph, S. Funk, M. Döblinger, S. Morkötter, S. Hertenberger, L. Schweickert, J. Becker, S. Matich, M. Bichler, D. Spirkoska et al., Nano Lett. **13**, 1522 (2013).
[23] M. Fickenscher, T. Shi, H. E. Jackson, L. M. Smith, J. M. Yarrison-Rice, C. Zheng, P. Miller, J. Etheridge, B. M. Wong, Q. Gao et al., Nano Lett. **13**, 1016 (2013).
[24] C. Zheng, J. Wong-Leung, Q. Gao, H. H. Tan, C. Jagadish, and J. Etheridge, Nano Lett. **13**, 3742 (2013).
[25] A. M. Munshi, D. L. Dheeraj, J. Todorovic, A. T. J. van Helvoort, H. Weman, and B. O. Fimland, J. Cryst. Growth **372**, 163 (2013).
[26] S. R. Glanvill, Microsc. Res. Techniq. **31**, 275 (1995).
[27] C. Dwyer, Ultramic. **110**, 195 (2010).
[28] A. Rosenauer, K. Gries, K. Müller, A. Pretorius, M. Schowalter, A. Avramescu, K. Engl, and S. Lutgen, Ultramic. **109**, 1171 (2009).
[29] J. M. LeBeau and S. Stemmer, Ultramic. **108**, 1653 (2008).
[30] S. Findlay and J. LeBeau, Ultramic. **124**, 52 (2013).
[31] C. Rossouw, C. Dwyer, H. Katz-Boon, and J. Etheridge(2013), Accepted in Ultramic.
[32] C. Dwyer and J. Etheridge, Ultramic. **96**, 343 (2003).
[33] P. Voyles, J. Grazul, and D. Muller, Ultramic. **96**, 251 (2003).
[34] C. J. Rossouw, L. J. Allen, S. D. Findlay, and M. P. Oxley, Ultramic. **96**, 299 (2003).
[35] P. M. Petroff, A. Y. Cho, F. K. Reinhart, A. C. Gossard, and W. Wiegmann, Phys. Rev. Lett. **48**, 170 (1982).

Part III

Conclusions

Chapter 4

Conclusions, summary and future work

In this work, quantitative HAADF STEM was applied to study heterostructured GaAs-based NWs. Three types of NWs grown with Au- and Ga-assisted MBE were investigated: GaAs NWs with axial GaAsSb inserts, GaAsSb NWs, and GaAs/AlGaAs core-shell NWs. In this concluding chapter the main findings from the method and material perspective are summarized, and suggestions for future studies are given.

4.1 Conclusions

4.1.1 Quantitative HAADF STEM

Scanning the ADF detector on JEOL 2010F

A prerequisite for quantitative HAADF STEM work is that the experimental images are normalized to the incident beam intensity. The normalization can be accomplished by using a detector scan image, as was explained in section 2.5.1. Hence a crucial achievement for the present study was being able to perform the detector scan on the JEOL 2010F, on which most of the experiments were performed. Once the correct procedure was found (given in section 2.5.1), it was applied repeatedly in each HAADF STEM session on the JEOL 2010F aiming for quantitative image analysis.

Quantifying Sb concentration in GaAsSb

To our knowledge, Sb concentration in $GaAs_{1-y}Sb_y$ has not been previously studied by quantitative HAADF STEM. Being a heavy element in a

lighter matrix, it was assumed that this would be a relatively straightforward task, however many challenges were met along the way. The GaAs lattice is strongly affected by the introduced Sb due to the larger covalent radius of Sb with respect to As, inducing SAD to the lattice, and due to the large lattice mismatch between GaAs and GaSb (see sections 2.4.3 and 2.5.2). In an initial quantitative HAADF STEM study on GaAs/GaAsSb NWs [138], these factors were not considered in the image simulations, resulting in an overestimation of the Sb concentration in the insert. In Paper I, written in cooperation with T. Grieb, M. Schowalter and A. Rosenauer from the University of Bremen, the SAD, and the changes in the lattice parameter and the Debye-Waller factor of Ga due to the change in composition were included in the simulations. This was an important improvement towards a more accurate analysis of Sb concentration in $GaAs_{1-y}Sb_y$ by quantitative HAADF STEM. Other non-compositional factors affecting the HAADF STEM intensity, namely the intensity dips at the insert interfaces resulting from surface strain relaxation [92], were also identified owing to the collaboration with the group of A. Rosenauer.

The compositional analysis of GaAsSb inserts within GaAs NWs and GaAsSb NWs was performed on NWs lying in plane. In this case, the cross-sectional thickness profile of the NW could be determined from the projected width in the TEM image, assuming a hexagonal shape. In Paper I, fitting the normalized experimental intensity profile across a ZB GaAs segment to the corresponding simulated profile, based on the modelled thickness profile, served as a valuable verification for the quantification approach. At the GaAsSb inserts, in Papers I and II a mismatch in the cross-sectional experimental intensity profile and a simulated profile assuming a uniform distribution of Sb was observed, indicating a decrease in Sb concentration towards the NW surface.

In Paper III, a step further was taken by applying a concentration profile based on a physical model for diffusion in the hexagonal NW in order to explain the observed HAADF STEM intensity profiles. By studying different batches of GaAs/GaAsSb and GaAsSb NWs, the effects of growth time and temperature on the observed HAADF STEM intensity profiles were identified and correlated with the changes in the cross-sectional Sb concentration profiles. It was additionally observed that diffusion alone could not explain the observed intensity profiles at the GaAsSb inserts, but radial GaAs overgrowth takes place during the post-insert GaAs growth as well. The work provided valuable information on the redistribution of Sb taking place during the growth of GaAs/GaAsSb and GaAsSb NWs, which will have to be considered in the growth optimization of these NWs in the future.

Quantifying Al concentration in AlGaAs

As opposed to GaAsSb, AlGaAs is virtually free of SAD, and the change in lattice parameter between GaAs and AlAs is negligible (see sections 2.4.3 and 2.5.2). HAADF STEM image simulations of $Al_xGa_{1-x}As$ were hence relatively straightforward to realize. Nevertheless, apart from an early, pioneering quantitative HAADF STEM study [5], there have been no attempts to quantify Al concentration in $Al_xGa_{1-x}As$, and the work presented in Paper IV is hence unique. Most importantly, in this paper a method for processing the atomic resolution HAADF STEM images, yielding unit cell resolution compositional analysis, was developed. The method allowed detailed analysis of Al concentration variations in the $Al_xGa_{1-x}As$ shell in cross-sectioned GaAs/AlGaAs NWs.

4.1.2 Heterostructured GaAs nanowires

GaAs/GaAsSb and GaAsSb nanowires

In the work on GaAs NWs with GaAsSb inserts, the most important discovery was the presence of axial and radial concentration gradients in the GaAsSb inserts. Before the findings in Paper I, it was assumed that the Sb concentration profile along the insert is rectangular, as usually is the case for group V elements in planar MBE grown heterostructures, and the possibility for radial concentration gradients was also not considered. In Paper II, the effects of the axial concentration gradients on the NWs optical properties were studied in detail using correlated PL-TEM. In Paper III, the causes for the radial concentration gradients were investigated further using a physical model, comparing different growth batches, and their effects on the NW properties were discussed. Additional findings in Paper III were the radial overgrowth of GaAs on the GaAsSb inserts during the post-insert axial GaAs growth, as well as a variation in the radial Sb concentration profile along the length of GaAsSb NWs. The last-mentioned induced a variation in Sb concentration along the GaAsSb NW, and its effects on the NWs electrical properties will be a topic of a future study [139].

GaAs/AlGaAs core-shell nanowires

Core-shell structured GaAs/AlGaAs NWs are currently a very active area of research, and several studies on the compositional variations and optical properties on similar NWs as studied in Paper IV became published during spring 2013 [123, 124, 140]. These earlier reports however base their compositional analysis on a qualitative interpretation of HAADF STEM images

and EDX. The quantitative HAADF STEM analysis presented in Paper IV shows the concentration variations on a higher spatial resolution and higher accuracy than what has been reported, and compositional features that had not been detected earlier were identified. These include depletion of Al in the immediate surroundings of the Al-rich bands, as well as an increase in Al concentration in the Al-rich band and in the AlGaAs shell segment in a direction outward from the core. These findings could give more insight to why the peculiar concentration variations in the AlGaAs shell arise.

4.2 Summary

The main findings and achievements regarding the quantitative HAADF STEM method and the NW material:

- Establishing a procedure for performing the detector scan on the JEOL 2010F.
- Quantifying Sb concentration in $GaAs_{1-y}Sb_y$, with SAD included in the HAADF STEM image simulations.
- Identifying axial concentration gradients in GaAsSb inserts in GaAs NWs, and studying their effects on the NWs optical properties.
- Identifying radial concentration gradients in GaAsSb inserts within GaAs NWs and in GaAsSb NWs, and explaining their causes through quantitative analysis of HAADF STEM intensity profiles across the GaAsSb segments, applying a physical model considering diffusion and radial GaAs overgrowth.
- Developing a method for quantifying Al concentration in $Al_xGa_{1-x}As$ at unit cell spatial resolution using aberration corrected STEM.

4.3 Future work

4.3.1 Quantitative HAADF STEM

Once the methodology for quantifying alloy concentration in the hexagonal NWs has been established, it would be interesting to apply this technique to different types of NWs: to different alloys of GaAs, or completely different III-V NWs, such as the InP system studied for instance by the NW group at Lund University [95].

Alloying is important for adjusting the NWs optoelectronic properties, however to create a p-n junction and finally a NW solar cell, doping is required. One common dopant for GaAs is Be, and Be-doped GaAs NWs are already grown by the NW group at IET, NTNU. The dopant concentrations are much lower than the concentrations of alloying elements. It would be interesting to see if HAADF STEM has the sensitivity to detect variations in Be-concentration along the Be-doped GaAs NWs.

The observed surface depletion of Sb in GaAsSb inserts and GaAsSb NWs complicated accurate concentration determination in these structures. In Paper III, an average Sb concentration for the GaAsSb segments was determined from the basis of HAADF STEM intensities, assuming a homogeneous Sb distribution throughout the NW. The maximum Sb concentration in the NW centre was additionally estimated using the developed diffusion model. It is however not clear how well the estimated maximum concentration corresponds to the actual Sb concentration in the NW centre, and how does the variation in concentration in the electron beam direction affect the HAADF STEM intensity quantification, and hence the determination of the average Sb concentration. Initial simulations were carried out in the context of Paper III to study these concerns, however more work is needed to answer these remaining questions.

In section 3.3.4, a procedure for correlated PL-(S)TEM was introduced, and initial results from a Ga-assisted insert NW were presented. Similarly to Paper II, where Au-assisted insert NWs were studied by correlated PL-TEM, correlated PL-(S)TEM could contribute in finding out the actual Sb concentration in the inserts of Ga-assisted NWs. More NWs should therefore be studied with this method.

Finally, here a procedure for acquiring a detector scan image at the JEOL 2010F, which is soon replaced by new instruments at NTNU, was established. To perform truly quantitative HAADF STEM imaging also in the future, the same should be achieved on the new instruments. This is a challenge for the future PhD students and post docs at the TEM Gemini centre. Hopefully the description about the procedure on JEOL 2010F given in section 2.5.1 will be of help in accomplishing this task.

4.3.2 Heterostructured GaAs nanowires

During the visit to MCEM, not only Ga-assisted but also Au-assisted GaAs/AlGaAs core-shell NWs, which have the WZ phase, were microtomed and studied with the the FEI Titan^3 80-300 and later with the JEOL 2010F at NTNU. Among these cross-sections, taken at different heights along the NWs, large variations in the core-shell morphology were observed

(figure 3.4): in some cases, the core had a round shape and the core and the shell exhibited very similar HAADF STEM intensities; in other cases the core had a distinct hexagonal shape, and the shell had a clearly lower HAADF STEM intensity with respect to the core. It was assumed that the first-mentioned cross-sections were from the axial AlGaAs segment which forms during the shell growth (see section 3.1). To confirm this, new cross-sections were prepared by focused ion beam, in which case the original position of the cross-section along the NW is known. In these attempts, however, NWs with an axial AlGaAs segment were not identified, and the prepared cross-sections had a distinct core-shell structure and a hexagonal core. There are no studies on cross-sectioned WZ GaAs/AlGaAs core-shell NWs, hence this would be an interesting piece of work to accomplish. Moreover, WZ GaAs/AlGaAs core-shell NWs show unique optical properties [112], and it would be interesting to study how the optical properties are affected by the variations in the cross-sectional morphology along the NWs.

Once the skill for preparing good cross-sectional specimens by microtomy had been learned during the visit to MCEM, it would be important to pass on this skill, although this would require some new investments to the TEM specimen preparation laboratory at TEM Gemini Centre. Nevertheless, once learned, microtomy is a relatively easy and fast method to produce high-quality specimens – a well-suited task for a project or master student! As mentioned in section 3.4, the NW group at IET, NTNU, has an ongoing project for developing GaAs/AlGaAs core-shell NW solar cells. To characterize the core and shell dimensions as well as the doping densities in the core and the shell, which according to the simulations are crucial for the device performance [137], cross-sectioned TEM specimens are needed.

The new aberration corrected instrument at NTNU opens new possibilities also regarding studies on heterostructured GaAs NWs. Apart from an early qualitative HAADF STEM experiment at the Aalto University, Finland, GaAs/GaAsSb NWs have only been characterised at a relatively low magnification. Now that an aberration corrected instrument is available at NTNU, it would be interesting to study the GaAsSb inserts at atomic resolution – to study the Sb concentration in detail near the insert interfaces, and to reveal possible clustering of Sb in the inserts.

To conclude, this study has shown that quantitative HAADF STEM is well-suited for studying heterostructured GaAs-based NWs. Many unexpected features, that affect the NWs optical properties and should hence be considered in the growth optimization, were identified and studied in detail. It is hence strongly recommended that quantitative HAADF STEM will be applied for studying heterostructured NWs also in the future.

References

[1] S. J. Pennycook and D. E. Jesson, "High-resolution Z-contrast imaging of crystals," *Ultramicroscopy*, vol. 37, no. 1-4, pp. 14–38, 1991.

[2] P. D. Nellist and S. J. Pennycook, "Incoherent imaging using dynamically scattered coherent electrons," *Ultramicroscopy*, vol. 78, no. 1-4, pp. 111–124, 1999.

[3] J. M. LeBeau and S. Stemmer, "Experimental quantification of annular dark-field images in scanning transmission electron microscopy," *Ultramicroscopy*, vol. 108, no. 12, pp. 1653–1658, 2008.

[4] A. Rosenauer, K. Gries, K. Müller, A. Pretorius, M. Schowalter, A. Avramescu, K. Engl, and S. Lutgen, "Measurement of specimen thickness and composition in $Al_xGa_{1-x}N$/GaN using high-angle annular dark field images," *Ultramicroscopy*, vol. 109, no. 9, pp. 1171–1182, 2009.

[5] S. Anderson, C. Birkeland, G. Anstis, and D. Cockayne, "An approach to quantitative compositional profiling at near-atomic resolution using high-angle annular dark field imaging," *Ultramicroscopy*, vol. 69, no. 2, pp. 83 – 103, 1997.

[6] S. V. Aert, J. Verbeeck, R. Erni, S. Bals, M. Luysberg, D. V. Dyck, and G. V. Tendeloo, "Quantitative atomic resolution mapping using high-angle annular dark field scanning transmission electron microscopy," *Ultramicroscopy*, vol. 109, no. 10, pp. 1236 – 1244, 2009.

[7] A. Rosenauer, T. Mehrtens, K. Müller, K. Gries, M. Schowalter, P. V. Satyam, S. Bley, C. Tessarek, D. Hommel, K. Sebald, M. Seyfried, J. Gutowski, A. Avramescu, K. Engl, and S. Lutgen, "Composition mapping in InGaN by scanning transmission electron microscopy," *Ultramicroscopy*, vol. 111, no. 8, pp. 1316–1327, 2011.

[8] J. M. LeBeau, S. D. Findlay, L. J. Allen, and S. Stemmer, "Standardless atom counting in scanning transmission electron microscopy," *Nano Lett.*, vol. 10, no. 11, pp. 4405–4408, 2010.

[9] H. Katz-Boon, C. J. Rossouw, C. Dwyer, and J. Etheridge, "Rapid Measurement of Nanoparticle Thickness Profiles," *Ultramicroscopy*, vol. 124, pp. 61 – 70, 2013.

[10] K. L. Kavanagh, "Misfit dislocations in nanowire heterostructures," *Semicond. Sci. Tech.*, vol. 25, no. 2, p. 024006, 2010.

[11] T. Mårtensson, C. P. T. Svensson, B. A. Wacaser, M. W. Larsson, W. Seifert, K. Deppert, A. Gustafsson, L. R. Wallenberg, and L. Samuelson, "Epitaxial IIIV nanowires on silicon," *Nano Lett.*, vol. 4, no. 10, pp. 1987–1990, 2004.

[12] D. L. Dheeraj, G. Patriarche, H. Zhou, T. B. Hoang, A. F. Moses, S. Grønsberg, A. T. J. van Helvoort, B.-O. Fimland, and H. Weman, "Growth and characterization of wurtzite GaAs nanowires with defect-free zinc blende GaAsSb inserts," *Nano Lett.*, vol. 8, no. 12, pp. 4459–4463, 2008.

[13] S. Plissard, K. A. Dick, X. Wallart, and P. Caroff, "Gold-free GaAs/GaAsSb heterostructure nanowires grown on silicon," *Appl. Phys. Lett.*, vol. 96, no. 12, p. 121901, 2010.

[14] L. J. Lauhon, M. S. Gudiksen, D. Wang, and C. M. Lieber, "Epitaxial core–shell and core–multishell nanowire heterostructures," *Nature*, vol. 420, no. 6911, pp. 57–61, 2002.

[15] H. L. Zhou, T. B. Hoang, D. L. Dheeraj, A. T. J. van Helvoort, L. Liu, J. C. Harmand, B. O. Fimland, and H. Weman, "Wurtzite GaAs/AlGaAs core-shell nanowires grown by molecular beam epitaxy," *Nanotechnology*, vol. 20, no. 41, p. 415701, 2009.

[16] L. Tsakalakos, J. Balch, J. Fronheiser, B. A. Korevaar, O. Sulima, and J. Rand, "Silicon nanowire solar cells," *Appl. Phys. Lett.*, vol. 91, no. 23, p. 233117, 2007.

[17] J. A. Czaban, D. A. Thompson, and R. R. LaPierre, "GaAs core-shell nanowires for photovoltaic applications," *Nano Lett.*, vol. 9, no. 1, pp. 148–154, 2009.

[18] E. C. Garnett, M. L. Brongersma, Y. Cui, and M. D. McGehee, "Nanowire solar cells," *Ann. Rev. Mat. Res.*, vol. 41, no. 1, pp. 269–295, 2011.

[19] X. Jiang, Q. Xiong, S. Nam, F. Qian, Y. Li, and C. M. Lieber, "InAs/InP radial nanowire heterostructures as high electron mobility devices," *Nano Lett.*, vol. 7, no. 10, pp. 3214–3218, 2007.

[20] Y. Li, J. Xiang, F. Qian, S. Gradecak, Y. Wu, H. Yan, D. A. Blom, and C. M. Lieber, "Dopant-free GaN/AlN/AlGaN radial nanowire heterostructures as high electron mobility transistors," *Nano Lett.*, vol. 6, no. 7, pp. 1468–1473, 2006.

[21] K. Tomioka, J. Motohisa, S. Hara, K. Hiruma, and T. Fukui, "GaAs/AlGaAs core multishell nanowire-based light-emitting diodes on Si," *Nano Lett.*, vol. 10, no. 5, pp. 1639–1644, 2010.

[22] F. Qian, S. Gradecak, Y. Li, C.-Y. Wen, and C. M. Lieber, "Core/multishell nanowire heterostructures as multicolor, high-efficiency light-emitting diodes," *Nano Lett.*, vol. 5, no. 11, pp. 2287–2291, 2005.

[23] L. Hu and G. Chen, "Analysis of optical absorption in silicon nanowire arrays for photovoltaic applications," *Nano Lett.*, vol. 7, no. 11, pp. 3249–3252, 2007.

[24] E. Garnett and P. Yang, "Light trapping in silicon nanowire solar cells," *Nano Lett.*, vol. 10, no. 3, pp. 1082–1087, 2010.

[25] M. Knoll and E. Ruska, "Das elektronenmikroskop," *Zeitschrift für Physik*, vol. 78, no. 5-6, pp. 318–339, 1932.

[26] E. Ruska, "The development of the electron microscope and of electron microscopy," *Bioscience Rep.*, vol. 7, no. 8, pp. 607–629, 1987.

[27] L. de Broglie, "Recherches sur la theorie des quanta," *Annales de Physique*, vol. 3, pp. 22–128, 1925.

[28] A. V. Crewe, J. Wall, and J. Langmore, "Visibility of single atoms," *Science*, vol. 168, no. 3937, pp. 1338–1340, 1970.

[29] A. V. Crewe, J. Wall, and L. Welter, "A high-resolution scanning transmission electron microscope," *J. Appl. Phys.*, vol. 39, no. 13, pp. 5861–5868, 1968.

[30] P. Nellist and S. Pennycook, "The principles and interpretation of annular dark-field Z-contrast imaging," in *Adv. Imag. Elect. Phys.*, vol. 113, pp. 147–203, 2000.

[31] D. B. Williams and C. B. Carter, *Transmission Electron Microscopy: A Textbook for Materials Science.* Springer, 2nd ed., 2009.

[32] R. Bjørge, C. Dwyer, M. Weyland, P. Nakashima, C. Marioara, S. Andersen, J. Etheridge, and R. Holmestad, "Aberration-corrected scanning transmission electron microscopy study of -like precipitates in an AlMgGe alloy," *Acta Mater.*, vol. 60, no. 67, pp. 3239 – 3246, 2012.

[33] R. Sæterli, E. Flage-Larsen, J. Friis, O. Løvvik, J. Pacaud, K. Marthinsen, and R. Holmestad, "Experimental and theoretical study of electron density and structure factors in CoSb3," *Ultramicroscopy*, vol. 111, no. 7, pp. 847 – 853, 2011.

[34] J. C. H. Spence and J. M. Cowley, "Lattice imaging in STEM," *Optik*, vol. 50, no. 2, pp. 129–142, 1978.

[35] J. M. Cowley, "Image contrast in a transmission scanning electron microscope," *Appl. Phys. Lett.*, vol. 15, no. 2, pp. 58–59, 1969.

[36] S. D. Findlay, N. Shibata, H. Sawada, E. Okunishi, Y. Kondo, T. Yamamoto, and Y. Ikuhara, "Robust atomic resolution imaging of light elements using scanning transmission electron microscopy," *Appl. Phys. Lett.*, vol. 95, no. 19, 2009.

[37] R. Erni, *Aberration-Corrected Imaging in Transmission Electron Microscopy: an Introduction.* World Scientific, 2010.

[38] E. J. Kirkland, *Advanced computing in electron microscopy.* Springer, 2nd ed., 2010.

[39] P. W. Hawkes, "Aberration correction past and present," *Philos. T. R. Soc. A*, vol. 367, no. 1903, pp. 3637–3664, 2009.

[40] P. D. Nellist and S. J. Pennycook, "Subangstrom resolution by underfocused incoherent transmission electron microscopy," *Phys. Rev. Lett.*, vol. 81, no. 19, pp. 4156–4159, 1998.

[41] O. L. Krivanek, N. Dellby, A. J. Spence, R. A. Camps, and L. M. Brown, "Aberration correction in the STEM," in *Inst. Phys. Conf. Ser.*, pp. 35–40, 1997.

[42] M. Haider, H. Rose, S. Uhlemann, E. Schwan, B. Kabius, and K. Urban, "A spherical-aberration-corrected 200 kV transmission electron microscope," *Ultramicroscopy*, vol. 75, no. 1, pp. 53–60, 1998.

[43] P. E. Batson, N. Dellby, and O. L. Krivanek, "Sub-ångstrom resolution using aberration corrected electron optics," *Nature*, vol. 418, no. 6898, pp. 617–620, 2002.

[44] Y. Zhu, H. Inada, K. Nakamura, and J. Wall, "Imaging single atoms using secondary electrons with an aberration-corrected electron microscope," *Nat. Mater.*, vol. 8, no. 10, pp. 808–812, 2009.

[45] P. Voyles, D. Muller, and E. Kirkland, "Depth-dependent imaging of individual dopant atoms in silicon," *Microsc. Microanal.*, vol. 10, no. 2, pp. 291–300, 2004.

[46] C. Dwyer and J. Etheridge, "Scattering of ångstrom-scale electron probes in silicon," *Ultramicroscopy*, vol. 96, no. 3-4, pp. 343–360, 2003.

[47] A. Howie, "Aberration correction: zooming out to overview," *Philos. T. Roy. Soc. A*, vol. 367, no. 1903, pp. 3859–3870, 2009.

[48] S. J. Pennycook, "Structure determination through Z-contrast microscopy," *Adv. Imag. Elect. Phys.*, vol. 123, pp. 173–206, 2002.

[49] P. D. Nellist, *Scanning Transmission Electron Microscopy: Imaging and Analysis*, ch. The Principles of STEM imaging. Springer, 2011.

[50] S. J. Pennycook, B. Rafferty, and P. D. Nellist, "Z-contrast imaging in an aberration-corrected scanning transmission electron microscope," *Microsc. Microanal.*, vol. 6, no. 04, pp. 343–352, 2000.

[51] C. Dwyer, R. Erni, and J. Etheridge, "Measurement of effective source distribution and its importance for quantitative interpretation of STEM images," *Ultramicroscopy*, vol. 110, no. 8, pp. 952 – 957, 2010.

[52] B. Rafferty, P. D. Nellist, and S. J. Pennycook, "On the origin of transverse incoherence in Z-contrast STEM," *J. Electron Microsc.*, vol. 50, no. 3, pp. 227–233, 2001.

[53] K. Watanabe, T. Yamazaki, I. Hashimoto, and M. Shiojiri, "Atomic-resolution annular dark-field STEM image calculations," *Phys. Rev. B*, vol. 64, no. 11, 2001.

[54] S. D. Findlay, L. J. Allen, M. P. Oxley, and C. J. Rossouw, "Lattice-resolution contrast from a focused coherent electron probe. Part II," *Ultramicroscopy*, vol. 96, no. 1, pp. 65–81, 2003.

[55] M. Herrera, Q. M. Ramasse, D. G. Morgan, D. Gonzalez, J. Pizarro, A. Yáñez, P. Galindo, R. Garcia, M.-H. Du, S. B. Zhang, M. Hopkinson, and N. D. Browning, "Atomic scale high-angle annular dark field STEM analysis of the N configuration in dilute nitrides of GaAs," *Phys. Rev. B*, vol. 80, no. 12, p. 125211, 2009.

[56] C. Dwyer, "Simulation of scanning transmission electron microscope images on desktop computers," *Ultramicroscopy*, vol. 110, no. 3, pp. 195–198, 2010.

[57] A. Rosenauer and M. Schowalter, "STEMSIM – A new software tool for simulation of STEM HAADF Z-contrast imaging," vol. 120 of *Springer Proceedings in Physics*, pp. 170–172, 2008.

[58] C. Koch, *Determination of core structure periodicity and point defect denisty along dislocations*. PhD thesis, Arizona State University, 2002.

[59] R. F. Loane, P. Xu, and J. Silcox, "Thermal vibrations in convergent-beam electron diffraction," *Acta Cryst. A*, vol. 47, no. 3, pp. 267–278, 1991.

[60] D. A. Muller, B. Edwards, E. J. Kirkland, and J. Silcox, "Simulation of thermal diffuse scattering including a detailed phonon dispersion curve," *Ultramicroscopy*, vol. 86, no. 34, pp. 371 – 380, 2001.

[61] K. Ishizuka, "A practical approach for STEM image simulation based on the FFT multislice method," *Ultramicroscopy*, vol. 90, pp. 71–83, Feb 2002.

[62] L. J. Allen, S. D. Findlay, M. P. Oxley, and C. J. Rossouw, "Lattice-resolution contrast from a focused coherent electron probe. Part I," *Ultramicroscopy*, vol. 96, no. 1, pp. 47–63, 2003.

[63] J. Pizarro, P. L. Galindo, E. Guerrero, A. Yanez, M. P. Guerrero, A. Rosenauer, D. L. Sales, and S. I. Molina, "Simulation of high angle annular dark field scanning transmission electron microscopy images of large nanostructures," *Appl. Phys. Lett.*, vol. 93, no. 15, 2008.

[64] J. M. LeBeau, S. D. Findlay, L. J. Allen, and S. Stemmer, "Quantitative atomic resolution scanning transmission electron microscopy," *Phys. Rev. Lett.*, vol. 100, no. 20, 2008.

[65] F. Glas, "Correlated static atomic displacements and transmission-electron-microscopy contrast in compositionally homogeneous disordered alloys," *Phys. Rev. B*, vol. 51, no. 2, pp. 825–839, 1995.

[66] D. D. Perovic, C. Rossouw, and A. Howie, "Imaging elastic strains in high-angle annular dark field scanning transmission electron microscopy," *Ultramicroscopy*, vol. 52, no. 3-4, pp. 353–359, 1993.

[67] V. Grillo, E. Carlino, and F. Glas, "Influence of the static atomic displacement on atomic resolution Z-contrast imaging," *Phys. Rev. B*, vol. 77, no. 5, p. 054103, 2008.

[68] X. Wu and J.-M. Baribeau, "Composition and strain contrast of $Si_{1-x}Ge_x$ (x = 0.20) and $Si_{1-y}C_y$ (y $\leq$ 0.015) epitaxial strained films on (100) Si in annular dark field images," *J. Appl. Phys.*, vol. 105, no. 4, p. 043517, 2009.

[69] F. Glas, "The effect of the static atomic displacements on the structure factors of weak reflections in cubic semiconductor alloys," *Philos. Mag.*, vol. 84, pp. 2055–2074, July 2004.

[70] B. Cordero, V. Gomez, A. E. Platero-Prats, M. Reves, J. Echeverria, E. Cremades, F. Barragan, and S. Alvarez, "Covalent radii revisited," *Dalton Trans.*, pp. 2832–2838, 2008.

[71] M. Schowalter, K. Müller, and A. Rosenauer, "Scattering amplitudes and static atomic correction factors for the composition-sensitive 002 reflection in sphalerite ternary III-V and II-VI semiconductors," *Acta Crystallogr., Sect. A: Found. Crystallogr.*, vol. 68, no. 1, pp. 68–76, 2012.

[72] S. Findlay and J. LeBeau, "Detector non-uniformity in scanning transmission electron microscopy," *Ultramicroscopy*, vol. 124, no. 0, pp. 52 – 60, 2013.

[73] P. Hartel, H. Rose, and C. Dinges, "Conditions and reasons for incoherent imaging in STEM," *Ultramicroscopy*, vol. 63, no. 2, pp. 93–114, 1996.

[74] E. Carlino and V. Grillo, "Atomic-resolution quantitative composition analysis using scanning transmission electron microscopy Z-contrast experiments," *Phys. Rev. B*, vol. 71, no. 23, 2005.

[75] S. I. Molina, D. L. Sales, P. L. Galindo, D. Fuster, Y. Gonzalez, B. Alen, L. Gonzalez, M. Varela, and S. J. Pennycook, "Column-by-column compositional mapping by Z-contrast imaging," *Ultramicroscopy*, vol. 109, no. 10, p. 1315, 2009.

[76] P. Robb and A. Craven, "Column ratio mapping: A processing technique for atomic resolution high-angle annular dark-field (HAADF) images," *Ultramicroscopy*, vol. 109, no. 1, pp. 61–69, 2008.

[77] H. Inada, L. Wu, J. Wall, D. Su, and Y. Zhu, "Performance and image analysis of the aberration-corrected Hitachi HD-2700C STEM," *J. Electron Microsc.*, vol. 58, no. 3, pp. 111–122, 2009.

[78] V. Grillo and F. Rossi, "STEM_CELL: A software tool for electron microscopy. Part 2 analysis of crystalline materials," *Ultramicroscopy*, vol. 125, pp. 112 – 129, 2013.

[79] S. Adachi, "GaAs, AlAs, and $Al_xGa_{1-x}As$: Material parameters for use in research and device applications," *J. Appl. Phys.*, vol. 58, no. 3, pp. R1–R29, 1985.

[80] I. Vurgaftman, J. R. Meyer, and L. R. Ram-Mohan, "Band parameters for III-V compound semiconductors and their alloys," *J. Appl. Phys.*, vol. 89, no. 11, pp. 5815–5875, 2001.

[81] T. Mehrtens, K. Müller, M. Schowalter, D. Hu, D. M. Schaadt, and A. Rosenauer, "Measurement of indium concentration profiles and segregation efficiencies from high-angle annular dark field-scanning transmission electron microscopy images," *Ultramicroscopy*, vol. 131, pp. 1–9, 2013.

[82] P. Voyles, J. Grazul, and D. Muller, "Imaging individual atoms inside crystals with ADF-STEM," *Ultramicroscopy*, vol. 96, no. 3-4, pp. 251–273, 2003.

[83] C. J. Rossouw, L. J. Allen, S. D. Findlay, and M. P. Oxley, "Channelling effects in atomic resolution STEM," *Ultramicroscopy*, vol. 96, no. 34, pp. 299 – 312, 2003.

[84] D. O. Klenov and S. Stemmer, "Contributions to the contrast in experimental high-angle annular dark-field images," *Ultramicroscopy*, vol. 106, no. 10, pp. 889–901, 2006.

[85] S. D. Findlay, D. O. Klenov, S. Stemmer, and L. J. Allen, "Atomic number contrast in high angle annular dark field imaging of crystals," *Mater. Sci. Tech. Ser.*, vol. 24, no. 6, pp. 660–666, 2008.

[86] C. Maunders, C. Dwyer, P. Tiemeijer, and J. Etheridge, "Practical methods for the measurement of spatial coherence – A comparative study," *Ultramicroscopy*, vol. 111, no. 8, pp. 1437 – 1446, 2011.

[87] S. I. Molina, M. P. Guerrero, P. L. Galindo, D. L. Sales, M. Varela, and S. J. Pennycook, "Calculation of integrated intensities in aberration-corrected Z-contrast images," *J. Electron Microsc.*, vol. 60, no. 1, pp. 29–33, 2011.

[88] C. Rossouw, C. Dwyer, H. Katz-Boon, and J. Etheridge, "Channelling contrast analysis of lattice images: Conditions for probe-insensitive stem," 2013. Accepted in Ultramicroscopy.

[89] J. E. Allen, E. R. Hemesath, D. E. Perea, J. L. Lensch-Falk, Z. Li, F. Yin, M. H. Gass, P. Wang, A. L. Bleloch, R. E. Palmer, *et al.*, "High-resolution detection of Au catalyst atoms in Si nanowires," *Nature Nanotech.*, vol. 3, no. 3, pp. 168–173, 2008.

[90] P. Voyles, D. Muller, J. Grazul, P. Citrin, and H. Gossmann, "Atomic-scale imaging of individual dopant atoms and clusters in highly n-type bulk Si," *Nature*, vol. 416, no. 6883, pp. 826–829, 2002.

[91] T. Grieb, K. Müller, R. Fritz, M. Schowalter, N. Neugebohrn, N. Knaub, K. Volz, and A. Rosenauer, "Determination of the chemical composition of GaNAs using STEM HAADF imaging and STEM strain state analysis," *Ultramicroscopy*, vol. 117, pp. 15 – 23, 2012.

[92] V. Grillo, "The effect of surface strain relaxation on HAADF imaging," *Ultramicroscopy*, vol. 109, no. 12, pp. 1453–1464, 2009.

[93] T. Grieb, K. Müller, R. Fritz, V. Grillo, M. Schowalter, K. Volz, and A. Rosenauer, "Quantitative chemical evaluation of dilute GaNAs using ADF STEM: Avoiding surface strain induced artifacts," *Ultramicroscopy*, vol. 129, pp. 1 – 9, 2013.

[94] HREM Research Inc., *qHAADF for DigitalMicrograph*, 2012. User Manual.

[95] J. Wallentin, N. Anttu, D. Asoli, M. Huffman, I. Åberg, M. H. Magnusson, G. Siefer, P. Fuss-Kailuweit, F. Dimroth, B. Witzigmann, H. Q.

Xu, L. Samuelson, K. Deppert, and M. T. Borgström, "InP nanowire array solar cells achieving 13.8% efficiency by exceeding the ray optics limit," *Science*, vol. 339, no. 6123, pp. 1057–1060, 2013.

[96] E. Lai, W. Kim, and P. Yang, "Vertical nanowire array-based light emitting diodes," *Nano Res.*, vol. 1, no. 2, pp. 123–128, 2008.

[97] G. Zheng, F. Patolsky, Y. Cui, W. U. Wang, and C. M. Lieber, "Multiplexed electrical detection of cancer markers with nanowire sensor arrays," *Nat. Biotechnol.*, vol. 23, no. 10, pp. 1294–1301, 2005.

[98] Y. Cui, Q. Wei, H. Park, and C. M. Lieber, "Nanowire nanosensors for highly sensitive and selective detection of biological and chemical species," *Science*, vol. 293, no. 5533, pp. 1289–1292, 2001.

[99] P. Yang, R. Yan, and M. Fardy, "Semiconductor nanowire: What's next?," *Nano Lett.*, vol. 10, no. 5, pp. 1529–1536, 2010.

[100] P. Hiralal, H. E. Unalan, and G. A. J. Amaratunga, "Nanowires for energy generation," *Nanotechnology*, vol. 23, no. 19, p. 194002, 2012.

[101] M. J. Bierman and S. Jin, "Potential applications of hierarchical branching nanowires in solar energy conversion," *Energ. Environ. Sc.*, vol. 2, no. 10, pp. 1050–1059, 2009.

[102] P. Krogstrup, H. I. Jørgensen, M. Heiss, O. Demichel, J. V. Holm, M. Aagesen, J. Nygård, and A. F. i Morral, "Single-nanowire solar cells beyond the Shockley-Queisser limit," *Nat. Photonics*, vol. 7, no. 4, pp. 306–310, 2013.

[103] H. Goto, K. Nosaki, K. Tomioka, S. Hara, K. Hiruma, J. Motohisa, and T. Fukui, "Growth of core-shell InP nanowires for photovoltaic application by selective-area metal organic vapor phase epitaxy," *Appl. Phys. Expr.*, vol. 2, no. 3, p. 035004, 2009.

[104] J. V. Holm, H. I. Jørgensen, P. Krogstrup, J. Nygård, H. Liu, and M. Aagesen, "Surface-passivated GaAsP single-nanowire solar cells exceeding 10% efficiency grown on silicon," *Nature Communications*, vol. 4, no. 1498, 2013.

[105] T. Fukui, M. Yoshimura, E. Nakai, and K. Tomioka, "Position-controlled III-V compound semiconductor nanowire solar cells by selective-area metalorganic vapor phase epitaxy," *AMBIO*, vol. 41, no. 2, pp. 119–124, 2012.

[106] S. F. Karg, "Nanowire multijunction solar cell," July 2010. Patent number US 20100175748.

[107] S. Wenham, M. A. Green, M. E. Watt, and R. Corkish, *Applied Photovoltaics*. Earthscan, 2nd ed., 2007.

[108] D. L. Dheeraj, A. M. Munshi, M. Scheffler, A. T. J. van Helvoort, H. Weman, and B. O. Fimland, "Controlling crystal phases in GaAs nanowires grown by Au-assisted molecular beam epitaxy," *Nanotechnology*, vol. 24, no. 1, p. 015601, 2013.

[109] E. Alarcón-Lladó, S. Conesa-Boj, X. Wallart, P. Caroff, and A. F. i Morral, "Raman spectroscopy of self-catalyzed $GaAs_{1-x}Sb_x$ nanowires grown on silicon," *Nanotechnology*, vol. 24, no. 40, p. 405707, 2013.

[110] M. Hjort, J. Wallentin, R. Timm, A. A. Zakharov, U. Håkanson, J. N. Andersen, E. Lundgren, L. Samuelson, M. T. Borgström, and A. Mikkelsen, "Surface chemistry, structure, and electronic properties from microns to the atomic scale of axially doped semiconductor nanowires," *ACS nano*, vol. 6, no. 11, pp. 9679–9689, 2012.

[111] G. Bussone, R. Schott, A. Biermanns, A. Davydok, D. Reuter, G. Carbone, T. Schulli, A. Wieck, and U. Pietsch, "Grazing-incidence X-ray diffraction of single GaAs nanowires at locations defined by focused ion beams," *J. Appl. Crystallogr.*, vol. 46, no. 4, 2013.

[112] L. Ahtapodov, J. Todorovic, P. Olk, T. Mjåland, P. Slåttnes, D. L. Dheeraj, A. T. J. van Helvoort, B. O. Fimland, and H. Weman, "A story told by a single nanowire: Optical properties of wurtzite GaAs," *Nano Lett.*, vol. 12, no. 12, pp. 6090–6095, 2012.

[113] R. S. Wagner and W. C. Ellis, "Vapor-liquid-solid mechanism of single crystal growth," *Appl. Phys. Lett.*, vol. 4, no. 5, pp. 89–90, 1964.

[114] D. L. Dheeraj, G. Patriarche, L. Largeau, H. L. Zhou, A. T. J. van Helvoort, F. Glas, J. C. Harmand, B. O. Fimland, and H. Weman, "Zinc blende GaAsSb nanowires grown by molecular beam epitaxy," *Nanotechnology*, vol. 19, no. 27, p. 275605, 2008.

[115] A. M. Munshi, D. L. Dheeraj, J. Todorovic, A. T. J. van Helvoort, H. Weman, and B. O. Fimland, "Crystal phase engineering in self-catalyzed GaAs and GaAs/GaAsSb nanowires grown on Si(111)," *J. Cryst. Growth*, vol. 372, pp. 163 – 169, 2013.

[116] A. M. Munshi, D. L. Dheeraj, V. T. Fauske, D.-C. Kim, A. T. J. van Helvoort, B. O. Fimland, and H. Weman, "Vertically aligned GaAs nanowires on graphite and few-layer graphene: generic model and epitaxial growth," *Nano Lett.*, vol. 12, no. 9, pp. 4570–4576, 2012.

[117] V. Dhaka, T. Haggren, H. Jussila, H. Jiang, E. Kauppinen, T. Huhtio, M. Sopanen, and H. Lipsanen, "High quality GaAs nanowires grown on glass substrates," *Nano Lett.*, vol. 12, no. 4, pp. 1912–1918, 2012.

[118] F. Glas, J.-C. Harmand, and G. Patriarche, "Why does wurtzite form in nanowires of III-V zinc blende semiconductors?," *Phys. Rev. Lett.*, vol. 99, no. 14, p. 146101, 2007.

[119] M. I. McMahon and R. J. Nelmes, "Observation of a wurtzite form of gallium arsenide," *Phys. Rev. Lett.*, vol. 95, no. 21, p. 215505, 2005.

[120] A. Kelly and K. M. Knowles, *Crystallography and Crystal Defects.* Wiley, 2nd ed., 2012.

[121] C. Thelander, P. Caroff, S. Plissard, A. W. Dey, and K. A. Dick, "Effects of crystal phase mixing on the electrical properties of InAs nanowires," *Nano Lett.*, vol. 11, no. 6, pp. 2424–2429, 2011.

[122] S. R. Glanvill, "Ultramicrotomy of semiconductors and related materials," *Microsc. Res. Techniq.*, vol. 31, no. 4, pp. 275–284, 1995.

[123] M. Heiss, Y. Fontana, A. Gustafsson, G. Wüst, C. Magen, D. D. O'Regan, J. W. Luo, B. Ketterer, S. Conesa-Boj, A. V. Kuhlmann, J. Houel, E. Russo-Averchi, J. R. Morante, M. Cantoni, N. Marzari, J. Arbiol, A. Zunger, R. J. Warburton, and A. Fontcuberta i Morral, "Self-assembled quantum dots in a nanowire system for quantum photonics," *Nat. Mater.*, vol. 12, pp. 1476–4660, 2013.

[124] D. Rudolph, S. Funk, M. Döblinger, S. Morkötter, S. Hertenberger, L. Schweickert, J. Becker, S. Matich, M. Bichler, D. Spirkoska, I. Zardo, J. J. Finley, G. Abstreiter, and G. Koblmüller, "Spontaneous alloy composition ordering in GaAs-AlGaAs core-shell nanowires," *Nano Lett.*, vol. 13, no. 4, pp. 1522–1527, 2013.

[125] C. Zheng, J. Wong-Leung, Q. Gao, H. H. Tan, C. Jagadish, and J. Etheridge, "Polarity-driven 3-fold symmetry of GaAs/AlGaAs core multishell nanowires," *Nano Lett.*, vol. 13, no. 8, pp. 3742–3748, 2013.

[126] T. Walther, "An improved approach to quantitative X-ray microanalysis in (S)TEM: Thickness dependent k -factors," *J. Phys. Conf. Ser.*, vol. 241, no. 1, p. 012016, 2010.

[127] G. Cliff and G. W. Lorimer, "The quantitative analysis of thin specimens," *J. Microsc.*, vol. 103, no. 2, pp. 203–207, 1975.

[128] M. DeGraef, *Introduction to Conventional Transmission Electron Microscopy*. Cambridge University Press, 2003.

[129] J. Todorovic, A. F. Moses, T. Karlberg, P. Olk, D. L. Dheeraj, B. O. Fimland, H. Weman, and A. T. J. van Helvoort, "Correlated microphotoluminescence and electron microscopy studies of the same individual heterostructured semiconductor nanowires," *Nanotechnology*, vol. 22, no. 32, p. 325707, 2011.

[130] G. Gilliland, "Photoluminescence spectroscopy of crystalline semiconductors," *Mat. Sci. and Eng. R*, vol. 18, no. 36, pp. 99 – 399, 1997.

[131] S. Perera, M. A. Fickenscher, H. E. Jackson, L. M. Smith, J. M. Yarrison-Rice, H. J. Joyce, Q. Gao, H. H. Tan, C. Jagadish, X. Zhang, and J. Zou, "Nearly intrinsic exciton lifetimes in single twin-free GaAs/AlGaAs core-shell nanowire heterostructures," *Appl. Phys. Lett.*, vol. 93, no. 5, p. 053110, 2008.

[132] J. Noborisaka, J. Motohisa, S. Hara, and T. Fukui, "Fabrication and characterization of freestanding GaAs/AlGaAs core-shell nanowires and AlGaAs nanotubes by using selective-area metalorganic vapor phase epitaxy," *Appl. Phys. Lett.*, vol. 87, no. 9, p. 093109, 2005.

[133] C.-C. Chang, C.-Y. Chi, M. Yao, N. Huang, C.-C. Chen, J. Theiss, A. W. Bushmaker, S. LaLumondiere, T.-W. Yeh, M. L. Povinelli, C. Zhou, P. D. Dapkus, and S. B. Cronin, "Electrical and Optical Characterization of Surface Passivation in GaAs Nanowires," *Nano Lett.*, vol. 12, no. 9, pp. 4484–4489, 2012.

[134] R. Teissier, D. Sicault, J. C. Harmand, G. Ungaro, G. Le Roux, and L. Largeau, "Temperature-dependent valence band offset and bandgap energies of pseudomorphic GaAsSb on GaAs," *J. Appl. Phys.*, vol. 89, no. 10, pp. 5473–5477, 2001.

[135] M. Heurlin, M. H. Magnusson, D. Lindgren, M. Ek, L. R. Wallenberg, K. Deppert, and L. Samuelson, "Continuous gas-phase synthesis of nanowires with tunable properties," *Nature*, no. 7427, p. 9094, 2012.

[136] Sol Voltaics AB, 2013. `http://www.solvoltaics.com/` Information retrieved 8/2013.

[137] C. G. Lim and H. Weman, "Numerical analysis and device optimization of radial p-n junction $GaAs/Al_xGa_{1-x}As$ core-shell nanowire solar cells," in *Numerical Simulation of Optoelectronic Devices NUSOD '13*, 2013.

[138] H. Kauko, R. Bjørge, R. Holmestad, and A. T. J. van Helvoort, "Quantitative HAADF-STEM on heterostructured GaAs nanowires," in *J. Phys. Conf. Ser.*, vol. 371, p. 012056, 2012.

[139] J. Huh, H. Yun, D.-C. Kim, A. M. Munshi, D. L. Dheeraj, H. Kauko, A. T. J. van Helvoort, S. Lee, B. O. Fimland, and H. Weman, "Rectifying behavior in individual $GaAs_xSb_{1-x}$ nanowires with compositional gradients," 2013. In preparation.

[140] M. Fickenscher, T. Shi, H. E. Jackson, L. M. Smith, J. M. Yarrison-Rice, C. Zheng, P. Miller, J. Etheridge, B. M. Wong, Q. Gao, S. Deshpande, H. H. Tan, and C. Jagadish, "Optical, structural, and numerical investigations of GaAs/AlGaAs core-multishell nanowire quantum well tubes," *Nano Lett.*, vol. 13, no. 3, pp. 1016–1022, 2013.